UNIVERSITY OF CALIFORNIA,
IRVINE

Linking Structure to Function in Resting State Macroscale Neural Activity

DISSERTATION

submitted in partial satisfaction of the requirements
for the degree of

DOCTOR OF PHILOSOPHY

in Cognitive Sciences

by

Anirudh Wodeyar

Dissertation Committee:
Professor Ramesh Srinivasan, Chair
Professor Steven C. Cramer
Professor Jeffrey L. Krichmar

2019

DEDICATION

In memory of my grandmother (ajji) Lalitha Narayan, for always believing in me and in the power of education.

TABLE OF CONTENTS

Page

LIST OF FIGURES vi

LIST OF TABLES x

ACKNOWLEDGMENTS xi

CURRICULUM VITAE xii

ABSTRACT OF THE DISSERTATION xiii

1 Background 1
- 1.1 Non-Invasive Neuroimaging . . . 3
  - 1.1.1 EEG/MEG . . . 3
  - 1.1.2 fMRI . . . 4
- 1.2 Functional Connectivity . . . 4
  - 1.2.1 fMRI Functional Connectivity . . . 4
  - 1.2.2 Coherence . . . 5
  - 1.2.3 M/EEG Amplitude Envelope Correlation . . . 5
  - 1.2.4 Pitfalls in Functional Connectivity Inference . . . 6
- 1.3 Gaussian Graphical Models of Effective Connectivity . . . 9
  - 1.3.1 Using GGM to Examine fMRI Networks . . . 9
  - 1.3.2 Using GGM to Examine M/EEG Networks . . . 10
  - 1.3.3 Applying Graph Theory . . . 10
- 1.4 Linking Structural to Functional Connectivity . . . 11
- 1.5 Structure of the Dissertation . . . 13

2 Contribution of the Structural Connectome to different Temporal scales of MEG connectivity 14
- 2.1 Introduction . . . 14
- 2.2 Methods . . . 19
  - 2.2.1 Modeling Framework . . . 19
  - 2.2.2 Estimation of Effective Connectivity . . . 27
  - 2.2.3 Simulations . . . 34
  - 2.2.4 Application to MEG data . . . 37
- 2.3 Results . . . 40

2.3.1 Simulation . . . 40
2.3.2 MEG Data . . . 45
2.4 Discussion . . . 50
2.4.1 Partial Coherence and Partial Correlation . . . 50
2.4.2 Using Graph Theory . . . 52
2.4.3 Other Methods to Reduce Leakage Effects . . . 54
2.4.4 Limitations . . . 55
2.4.5 Conclusion . . . 56

3 Influence of damage to the Structural Connectome on Functional and Effective Connectivity in resting state fMRI 57
3.1 Introduction . . . 57
3.2 Methods . . . 61
3.2.1 Patient Details . . . 61
3.2.2 MRI . . . 61
3.2.3 fMRI . . . 62
3.2.4 Virtual Tractography . . . 62
3.2.5 Measures of fMRI Functional Connectivity . . . 64
3.2.6 Adaptive Graphical Lasso to Estimate fMRI Effective Connectivity . 64
3.2.7 Modeling Impact of SC damage . . . 71
3.2.8 fMRI streamline Functional Connectivity . . . 72
3.2.9 Communication Models of FC . . . 73
3.3 Results . . . 76
3.3.1 ROI level analysis show that SC damage modulates fMRI-EC but not fMRI-FC . . . 76
3.3.2 Voxel level analysis shows that SC damage modulates fMRI-sFC . . . 76
3.3.3 Relevance of SC edges modulating fMRI-FC . . . 77
3.4 Discussion . . . 80

4 Influence of damage to the Structural Connectome on EEG Effective Connectivity 84
4.1 Introduction . . . 84
4.2 Methods . . . 87
4.2.1 Modeling Framework . . . 87
4.2.2 Estimation of Effective Connectivity . . . 94
4.2.3 Data Analysis . . . 99
4.3 Results . . . 101
4.3.1 Edge Analysis Showed Weak Modulation from Damage . . . 101
4.3.2 Mean Degrees and Damage . . . 102
4.4 Discussion . . . 106
4.4.1 Limitations . . . 108

5 Conclusion 110
5.1 Structural Connectivity and Graphical Models for Effective Connectivity . . 111
5.2 Structural Connectivity and Function across Different Timescales . . . 112

5.3 Link between Structure and Function is Limited 113
5.4 Summary 113

Bibliography **115**

A Locations of Areas **125**
A.1 MNI coordinates of Lausanne Parcellation 125

LIST OF FIGURES

Page

1.1 Common Input Problem: The common input problem asks whether a relationship between two sources is driven by the presence of a third source. We represent these sources here by A, B and C and we see in the top figure that when there is a relationship between A with B and C, the covariance is unable to distinguish this difference from B being connected to C whereas the precision does in fact make this difference visible. In the second from top figure we see that when there is in fact a relationship between B and C this is well reflected in both covariance and precision. In the bottom set of figures we show how multiple sources of common inputs can be detected if using the precision. 8

2.1 Structural Connectome: We show the streamlines derived from [68] on the right and the structural connectome for the 114 areas of the Lausanne parcellation on the left. We show the binarized SC, with any non-zero edge being assigned a weight of 1. 20

2.2 MEG Forward Model: We show the brain, with x, y, z oriented dipoles for each brain region of interest, the CSF, skull and scalp boundaries and the location of MEG gradiometers with respect to the scalp for the $fsaverage$ head. Each of 102 red dots indicates the location of a pair of orthogonal planar gradiometers. 25

2.3 Sensitivity and False Discovery Rate in Simulation: We estimated networks using the cGGM and aGGM at different signal to noise ratios. We compared these networks to the binarized SC and examined the sensitivity (upper figure) and false discovery rate (lower figure) between them. cGGM models are more sensitive to the SC across all SNR. cGGM and aGGM have comparable false discovery rates when the SNR rises above 30 dB. 41

2.4 Weight Correlation in Simulation: We estimated networks using the cGGM and aGGM at different signal to noise ratios. We compared the partial coherence (cGGM) and partial correlation (aGGM) to the SC and examined the correlation between the set of SC edges and edges estimated. Partial coherence is more correlated to the SC than partial correlation across all SNR. Partial coherence has a correlation greater than 0.5 for almost all reconstructions at an SNR above 30 db while this is true for partial correlation only at 50 dB. 43

2.5 Graph Theory and Partial Coherence: We show how well using different graph theoretic metrics does at capturing the structural connectivity characteristics relative to using the reconstructed partial coherence weights. At each SNR, we plot the correlation between graph theory metrics calculated from reconstructed network with the original network across 500 iterations in green. In orange we show the correlation of the weights of reconstructed partial coherence with the original partial coherence. For comparison purposes we show the same set of correlations (of edge weights) alongside all graph theory metrics. We examine the two methods across different SNR and find that at SNR below 50 dB, closeness centrality, betweenness centrality and degrees provide more accurate reconstruction. 45
2.6 Graph Theory and Amplitude Partial Correlation: We show how well different graph theoretic metrics can capture the structural connectivity characteristics relative to using the reconstructed partial correlation weights. At each SNR, we plot the correlation between graph theory metrics calculated from reconstructed network with the original network across 500 iterations in green. In orange we show the correlation of the weights of reconstructed partial correlation with the original partial correlation. For comparison purposes we show the same set of correlations alongside all graph theory metrics. We examine the two methods across different SNR and find that at SNR below 30 dB, closeness centrality, betweenness centrality and degrees provide more accurate reconstruction. 46
2.7 Sensitivity and False Discovery Rate in MEG data: We estimated networks using the cGGM and aGGM at different signal to noise ratios. We compared these networks to the binarized SC and examined the sensitivity (upper figure) and false discovery rate (lower figure) between them. cGGM networks are more sensitive to the SC in the beta and gamma bands while aGGM networks are more sensitive to SC in alpha and beta bands. The cGGM network has lower false discovery rates relative to aGGM networks in beta and gamma bands. 49
2.8 Degrees Across Connectomes: We show degrees across different areas in the structural connectome. Similarly we show median degrees across subjects in the beta band when using partial correlation, and in gamma band when using partial coherence. 53

3.1 Virtual Tractography - in (a) we show the pipeline for virtual tractography. We remove from the set of streamlines that represent the undamaged structural connectome (top left) the streamlines intersecting any particular patient's lesion(s), as shown in the top middle figure. Using the reduced set of streamlines we apply the Lausanne parcellation to get the final structural connectome for that patient (shown on the right). (b)Edges Showing High Damage Across Patients - We show the number of edges where patients show high damage. We found that for over 50% of edges there are few (1 or 2) to no patients showing the presence of high damage. In our analysis we used all edges where 3 or more patients had high damage (341). 65

3.2 Using the Adaptive Graphical Lassso - This was the general processing pipeline for applying the AGL to fMRI covariance from patients. The binarized undamaged SC is used to bias the penalization used when optimizing under the AGL to estimate the precision(which after normalization gives us the partial correlation). 66
3.3 GL vs AGL - We show performance (cross-validated deviance) across penalization for the graphical lasso (on the left) and adaptive graphical lasso (right figure). The error bars represent the standard deviation of the deviance across patients. We found that for all but very high penalization the AGL outperformed the GL. Further, the AGL shows minimal cross-validated deviance for an optimal set of SC edges (at an SC penalization of0.125) while the graphical lasso shows minimum deviance only for very sparse models. 70
3.4 Streamline Functional Connectivity (sFC) - We show how sFC was calculated for two streamlines in two different patients. For each streamline the end points were identified as fMRI voxels and we estimated the correlation between them. We did the same for both connected (top) and disconnected streamlines (bottom). 73
3.5 Effective Connectivity and Structural Connectivity - On the top we show representative streamlines connectivity areas for which damage influenced effective connectivity. In the center is a matrix with edges modeled in gray and edges where EC was modulated in orange. U-Areas represents sets of areas in the undamaged hemisphere and D-Area represents groups of areas in the damaged hemisphere. 75
3.6 Streamline Functional Connectivity and Structural Connectivity - On the top we show representative streamline connectivity for areas for which damage influenced sFC. In the center is a matrix with edges modeled in gray and edges where sFC was modulated in orange. U-Areas represents sets of areas in the undamaged hemisphere and D-Area represents groups of areas in the damaged hemisphere. 78

4.1 Virtual Tractography - in (a) we show the pipeline for virtual tractography. We remove from the set of streamlines that represent the undamaged structural connectome (top left) the streamlines intersecting any particular patient's lesion(s), as shown in the top middle figure. Using the reduced set of streamlines we apply the Lausanne parcellation to get the final structural connectome for that patient (shown on the right). (b)Edges Showing High Damage Across Chronic and Subacute Groups - We show the number of edges where patients show high damage. 95
4.2 Mean Degrees in SC and Delta Band for Subacute group: In the top row we show the correlation between the degrees for each area and the mean degrees of damage across the subacute group of patients. In the bottom row we show a scatter of mean degrees over each hemisphere (ipsilesional/contralesional) and the mean degrees of damage in SC (across all areas). 103

4.3 Mean Degrees in SC and Theta Band for Chronic group: In the top row we show the correlation between the degrees for each area and the mean degrees of damage across the chronic group of patients. In the bottom row we show a scatter of mean degrees over each hemisphere (ipsilesional/contralesional) and the mean degrees of damage in SC (across all areas). 105

LIST OF TABLES

Page

2.1 Simulation Results: We show the averages across all simulation iterations for the different metrics computed on both the partial coherence and amplitude partial correlation. 42

A.1 Lausanne Parcellation of 114 areas: For each area we define the center of the area in X,Y, and Z coordinates defined for the MNI template. 129

ACKNOWLEDGMENTS

I would like to thank everyone who has helped me get on this path and complete it. I'll start with my parents, my mother Asha, and my father, Anand, their support has meant everything to me these past few years.

I'd like to thank my advisor, Ramesh Srinivasan, for his patience, kindness and support, our collaborators over the years - Ron Frostig, Ellen Wann, Jessica Cassidy, Steve Cramer for the discussions and opportunities. Thanks to my committee members, Beth Lopour, Joachim Vandekerckhove, Jeffrey Krichmar and Steve Cramer for their ideas and support. Also my labmates over the years, Josh Tromberg, Michael Nunez, Luke Baltzell, and Rakibul Hasan, are appreciated for all their help and good conversations. Finally, to all the friends I've made in my time here at UCI, who knew that strong relationships could be forged through difficult times.

The work discussed in this dissertation was supported by the School of Social Sciences, UCI and the Cognitive Sciences department, UCI.

CURRICULUM VITAE

Anirudh Wodeyar

EDUCATION

Ph.D. in Psychology with Concentration in Cognitive Neuroscience **2019**
University of California, Irvine *Irvine, California*

Master of Science in Statistics **2018**
University of California, Irvine *Irvine, California*

Bachelor of Engineering in Computer Science **2014**
BITS Pilani, K.K. Birla Goa Campus *Goa, India*

RESEARCH EXPERIENCE

Graduate Research Assistant **2014–2019**
University of California, Irvine *Irvine, California*

TEACHING EXPERIENCE

Teaching Assistant **2014-2019**
University of California Irvine *Irvine, California*

PUBLICATIONS

Wodeyar A, Srinivasan R. Network Structure During Encoding Predicts Working Memory Performance. bioRxiv. 2018 Jan 1:409615.

ABSTRACT OF THE DISSERTATION

Linking Structure to Function in Resting State Macroscale Neural Activity

By

Anirudh Wodeyar

Doctor of Philosophy in Cognitive Sciences

University of California, Irvine, 2019

Professor Ramesh Srinivasan, Chair

Macroscopic neural activity measured using fMRI, MEG and EEG shows consistent statistical dependencies between different areas of the brain which is labeled as functional connectivity. A major research direction in systems neuroscience has been the effort to trace functional connectivity back to structural connectivity, defined by the white-matter tracts of the brain. In this dissertation I examine the extent to which the structural connectivity constrains dynamic neural function. We first examined, in simulation and empirically, resting state MEG data from healthy subjects and tested whether effective connectivity estimates (models of functional connectivity) are sensitive to anatomical connectivity. Effective connectivity (EC) estimated using a graphical model assesses direct connectivity potentially providing a metric appropriate to compare against anatomical connections. In silico, we compared two different models for effective connectivity - complex valued Gaussian graphical models (cGGM) that emphasizes direct connectivity on the timescale of milliseconds and amplitude Gaussian Graphical models (aGGM) that emphasizes direct connectivity on the timescale of seconds. We found that the partial coherence, a summary statistic derived from cGGM, is more aligned to the anatomy than partial correlation (derived from aGGM). Using resting state MEG data, we found that partial coherence at higher frequencies (¿30Hz) indeed provided the greatest alignment to the structural connectivity. However, at lower frequencies (1-30 Hz), we found that the partial correlation was more tightly coupled to the

anatomy. We then examined the relationship between structure and function in a subject population with heterogeneous structural connections - subacute ($<$ 1 month post stroke) patients of stroke who have lesions in the brain. Using fMRI time series parcelled into 114 brain areas, we estimated Gaussian Graphical Models (GGM) to derive the partial correlation and used virtual tractography for the structural connectivity. We found that partial correlations (relative to traditional correlations) strongly reflected the presence of structural connectivity damage. Further, applying voxel-based analyses driven by the streamlines (representing axonal fibers) allowed us to see modulation from damage across more functional connections suggesting parceling the brain inappropriately spatial smooths diverse neural activity. Finally, we examined the impact of structural connectivity damage on function in subacute and chronic ($>$ 2 months post stroke) patients of stroke using EEG. We found increased structural damage was linked to increased overall connectivity (partial coherence) in both groups. Overall our results indicate that using simple models of effective connectivity (GGMs) allow better assessment of the relationship between macroscale structure and function but even so, structure mediates function only to a limited extent, with the relationship depending strongly on the timescale and spatial resolution of the effective connectivity.

Chapter 1

Background

Understanding the functions of the brain while simultaneously learning how the brain functions is a core goal of modern neuroscience. Historically, systems neuroscience has focused on the microscale, examining the structure and dynamics of individual neurons or neural population activity. The combined activity of thousands of neurons could be argued to be uninformative, i.e., potentially all functionally relevant activity occurs only at the lowest point of reduction along the hierarchy of neural complexity. However, research suggests that there is organized and functionally relevant activity at multiple scales. Mesoscale and macroscale oscillatory behavior, the periodic fluctuations in neural population activity influences the lower scales of activity and appears to be functionally relevant [1–3]. Alongside this, recent ideas on the philosophy behind studying macroscale neural activity suggests we could approach the macroscale with the perspective of weak emergence[4, 5]. An expectation of weak emergence suggests the combined activity of lower scale units is informative in itself and lends itself to analysis that would be considerably more difficult to perform when including all lower scale units (while we expect that analysis to still yield the same results). This multiscale organization of brain structure and dynamics inherently motivates examining the brain both at the scale of individual neurons and their circuitry and also at

the scale of populations of neurons and their connectivity through white matter bundles. The ability to examine the macroscale neural activity non-invasively was advanced greatly with the advent of electroencephalography in the early 1920s through the efforts of Hans Berger. Since then, with improved technology (magnetoencephalography - MEG, functional Magnetic Resonance Imaging - fMRI and Diffusion weighted imaging) alongside improved methodology and computing resources, systems neuroscience has been moving towards a deeper understanding of macroscale structural and dynamical organization.

The need for an effort to build a human connectome, a mapping of connections between brain areas, was first motivated in detail in 2005 [6]. Since then there have been multi-lab initiatives [7, 8] aimed at collecting the data that would permit the elucidation of the human connectome - both structural (through DWI/DTI) and functional (fMRI/MEG/EEG). The structural connectome [6], the set of axonal bundles that connect macroscale neural populations, is the pathway that organizes functional activity and leads to the presence of a functional connectome. The organization of functional activity can be expected to vary however, on different time scales, both on the rapid timescale delineated by axonal conduction velocities (1-40 milliseconds) to the slower timescale imposed by changing Na^+ and K^+ concentrations [9], neuromodulatory systems [10] and the network structure [11]. Different modalities likely capture distinct aspects of the organization of functional activity, with M/EEG being more sensitive to rapid timescale activity while fMRI is more sensitive to slower timescale activity. In our work we examine both M/EEG and fMRI functional connectivity, the relationships in neural activity between brain areas, and identify the aspects of functional connectivity that arise directly from the structural connectivity.

1.1 Non-Invasive Neuroimaging

1.1.1 EEG/MEG

Electroencephalography or EEG is the measurement of electrical potentials at the scalp generated by the synchronized post-synaptic currents through predominantly pyramidal neurons in the cortex [12]. EEG is sensitive to millisecond scale events allowing it access to rapid fluctuations in neural activity. These neurophysiological signals have intrinsic time scales of organization, often organized in terms of frequency bands that exhibit distinct behaviors in different cognitive tasks and clinical disease states. EEG has low spatial resolution given it measures current that propagates to the scalp by volume conduction through the tissues of the head. The electric properties of tissues and the details of volume conduction are only be approximately known.

Magnetoencephalography or MEG measures the magnetic fields generated by synchronous post-synaptic current sources in the brain. Measurements of MEG are usually conducted using SQUIDs(superconducting quantum interference device) to improve sensitivity to minute magnetic fields in a magnetically shielded room to reduce interference. Due to the nature of magnetic field generation from dipole sources (perpendicular to orientation of the dipole from the right hand rule) MEG sensors at the scalp are much more sensitive to neural sources in sulci. MEG is sensitive to millisecond fluctuations in neural activity and has an advantage relative to EEG since magnetic fields are less distorted by the resistive skull and scalp relative to electric fields [13]. More importantly, the physics of field spread to MEG sensors is easy to precisely model (in contrast to the EEG head models). MEG still has a low spatial resolution akin to EEG, due to the separation of the sensors from the current sources in the brain.

1.1.2 fMRI

Functional magnetic resonance imaging or fMRI is a measurement technique that has risen to prominence in cognitive neuroscience in the past three decades. While magnetic resonance imaging (MRI) has been a mainstay of the medical field for several decades, the discovery that haemodynamic changes could also be measured using MRI led to fMRI. It measures a surrogate of increased neural activity (specifically the aggregate synaptic activity rather than the spiking behavior [14]) - the blood oxygen level dependent signal or BOLD. Imaging of this signal occurs usually on three dimensional voxels of dimensions in the range of 3x3x3 mm and a seconds time scale. So while BOLD imaging is orders of magnitude slower than M/EEG, its excellent spatial resolution allows us to see detailed activity across the entire brain.

1.2 Functional Connectivity

Functional connectivity in macroscopic brain data (fMRI, EEG, MEG) refers to evidence of statistical dependence between two signals recorded from different areas of the brain [15]. This broad definition encompasses multiple techniques that emphasize different aspects of the underlying brain activity.

1.2.1 fMRI Functional Connectivity

Functional connectivity measures in fMRI data are based on the correlation between the BOLD signals averaged over voxels in predefined regions of interest, measuring coactivation (on a seconds time scale) of neural populations in different regions of the brain. These regions are specified using parcellations that carve up the brain based on anatomical or functional

characteristics [16]. By estimating correlations between all pairs of brain regions we define the functional connectome.

The functional connectome has been examined in both the resting state when a subject is simply resting in the scanner or in a task state. There are sets of brain areas (sub-networks) that are coactive consistently within and across subjects, referred to as resting state networks (RSN) [17, 18]. Examining these RSNs has shown that they are present and show differential expression during task states [18] suggesting they have functional relevance. This work also spurred the examination of slow timescale modulations of spontaneous activity in M/EEG [19, 20] to identify potentially similar sub-networks.

1.2.2 Coherence

M/EEG data is a superposition of oscillatory modes, and as such, it is usually analysed in the frequency domain rather than in the time domain. The Fourier transformed M/EEG data is separated into different frequency bands and functional connectivity is examined in specific bands. Coherence is the most widely used measure of function connectivity in M/EEG studies. It is the analogue of the squared correlation coefficient, but defined for complex-valued data - the Fourier coefficients in one frequency band measured at two sensors. Coherence measures the consistency of relative amplitude and relative phase between the two sensors [21], which an estimate of the synchronization on a millisecond time scale.

1.2.3 M/EEG Amplitude Envelope Correlation

Another estimate of functional connectivity emphasizing slow timescales in M/EEG is amplitude envelope correlation [22]. The goal of this method is to match the time scale of fMRI. Examining the slow amplitude modulations provides a window on slow activation

changes in fMRI as visible in M/EEG [23]. This estimate of FC is calculated by taking the amplitude envelope of bandpass filtered M/EEG signals, down-sampling and estimating the correlation [19, 24]. Theoretically, correlated amplitude modulations can be independent of purely phasic relationships in the brain. Amplitude envelope correlations have shown strong relationships to the BOLD correlations [25]. Several studies have shown that the amplitude correlations can be decomposed to reveal similar patterns as the RSNs from resting fMRI BOLD signals, further motivating its analysis [19, 23].

1.2.4 Pitfalls in Functional Connectivity Inference

Volume Conduction and Field Spread in M/EEG

Volume conduction [12] is the instantaneous spread of current from current sources in the brain through the tissues of the head brain, cerebrospinal fluid (CSF), skull, and scalp to the EEG sensors measuring potentials on the outer surface of the scalp. From any one source, the current spread through these tissues generates scalp potentials at many sensors, including sensors distant from the source. Simulations with approximate volume conduction models suggest this spread of current may extend as far as 10 cm (or more) in directions tangential to the scalp surface [12, 26]. An implication is that two sensors may show statistical dependence due to volume conduction because they are measuring the same active source(s). Functional connectivity due to volume conduction effects can be expected to be independent of frequency and be reduced with greater separation distance between electrodes [26, 27].

While MEG is not susceptible to volume conduction effects, it is however susceptible to field spread. Field spread arises from sensors being distant from the sources they are measuring. Magnetic field from a source is simultaneously measured at multiple sensors leading to high spurious functional connectivity [27].

One method to reduce the impact of volume conduction (field spread) on functional connectivity estimates is to apply source localization techniques. The underlying expectation is that data being measured by M/EEG arises from dipole sources in the brain. We first build a head model (discussed in more detail for MEG in Chapter 2 and EEG in Chapter 4) which informs us of how the current from dipole sources spreads to EEG sensors (or how the magnetic fields spread over MEG sensors). From the head model we get the forward model matrix- an estimate of the measured potential/field at each sensor due to a unit source at each location in the brain. Inverting this matrix to localize activity at sources in the brain is a difficult problem with a degenerate solution space. Different inverse algorithms tackle this problem using different assumptions on the statistics of source data (two common assumptions being that sources are linearly independent - yielding beamformer solutions [28], or that source power should be minimized - L2 norm inverse [29]). We favor the L2 norm inverse as the beamformer is based on the assumption that there is no correlations between sources. Unfortunately, even if these assumptions are valid, inverse solutions are not perfect reconstructions that absolutely remove volume conduction (field spread) effects [30]. In all inverse solutions, we see leakage effects. This phenomenon occurs when the activity localized to one source is correlated (due to an imperfect inverse solution) to nearby sources.

Common Inputs in M/EEG and fMRI

Another common pitfall when examining functional connectivity are false functional connections due to common inputs. Two areas that have no shared activity by communicating with the same brain region will have a non-zero functional connectivity. This connectivity does not reflect a direct connection, for instance by a corticocortical fiber system, between populations at the two areas. This implies that we cannot directly infer from high functional connectivity values a map of connections in the brain. We discuss ahead how using graphical models can help mitigate this pitfall as well.

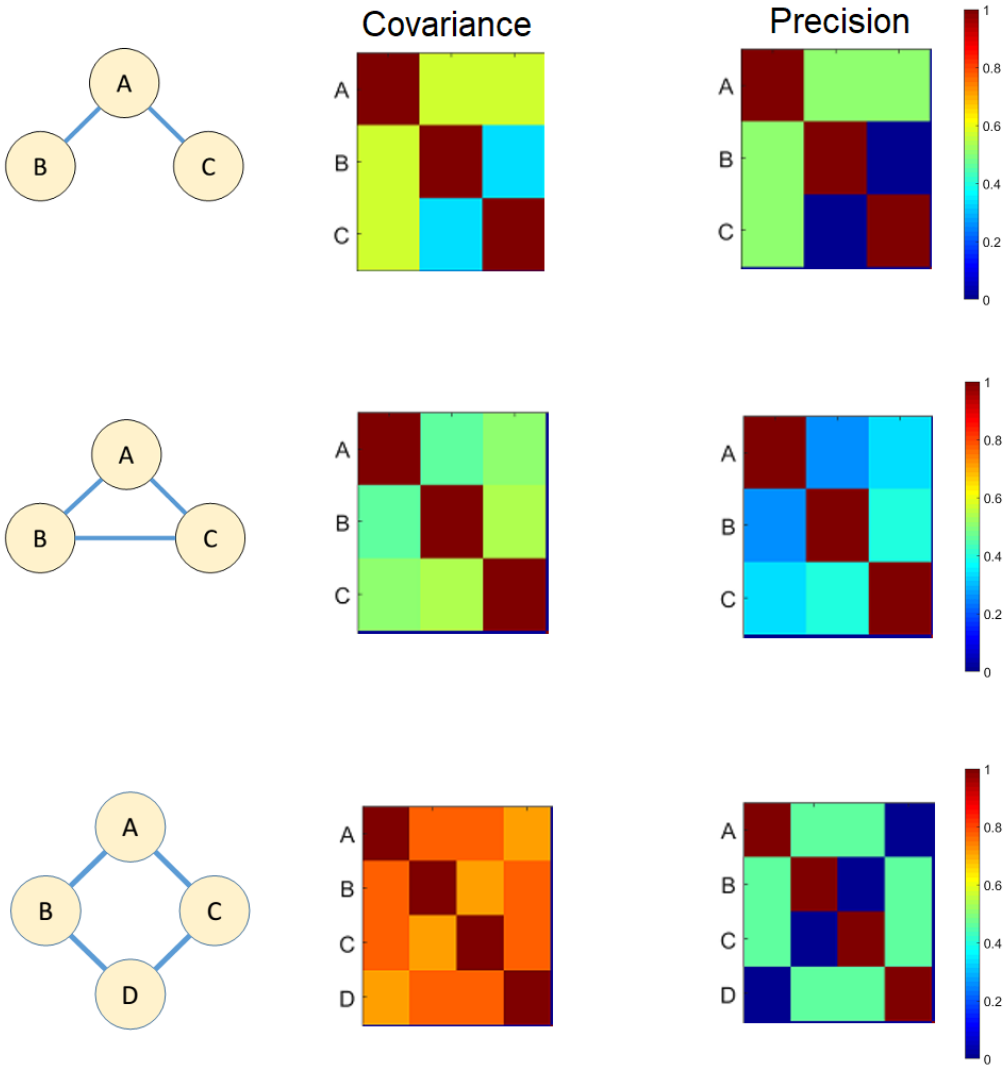

Figure 1.1: Common Input Problem: The common input problem asks whether a relationship between two sources is driven by the presence of a third source. We represent these sources here by A, B and C and we see in the top figure that when there is a relationship between A with B and C, the covariance is unable to distinguish this difference from B being connected to C whereas the precision does in fact make this difference visible. In the second from top figure we see that when there is in fact a relationship between B and C this is well reflected in both covariance and precision. In the bottom set of figures we show how multiple sources of common inputs can be detected if using the precision.

1.3 Gaussian Graphical Models of Effective Connectivity

We utilize the statistical framework of Gaussian Graphical Models (GGMs [31]) to estimate the effective connectivity. At the heart of the GGM is the estimation of precision, inverse of the covariance. The precision matrix quantifies the statistical dependence between any pair of random variables independent of linear effects from all other random variables. The non-zero values of the GGM represent the graph $G = (V, E)$, where V are the random variables and E is a binary matrix (adjacency matrix) representing the existence of a relationship between any pair from V, i.e., an edge. All edges of the graph G represent direct effects between a pair of random variables - which in our work will represent sources of neural activity in the brain. Therefore, an edge represents the direct effects between brain regions. We show examples of the covariance, precision and how it represents direct connections in Figure 1.1.

In this thesis we present the statistical framework that allows us to estimate graphical models for M/EEG and BOLD data. We apply and extend ideas from the graphical lasso literature [32, 33] - a method to estimate regularized solutions to the precision. We test the model with simulations (discussed in Chapters 2 and 3) and demonstrate that the Gaussian Graphical Model provides veridical estimates of effective connectivity, reducing the influence of common inputs and (in the case of M/EEG data) minimizing the effect of leakage effects.

1.3.1 Using GGM to Examine fMRI Networks

Past work has explored estimation of graphical models for fMRI data. Several papers advocate for estimation of the BOLD partial correlation (normalized precision) and show that it is a more consistent alternative to estimating linear correlation[34–36]. Partial correlation

has been used to identify differences in effective connectivity between disease and control, identify network structure in resting state and in task states [37–40]. Further, it has been applied to examine the link between connectivity in fMRI data and the anatomical connectivity [41, 42]. We further this body of research in chapter 4.

1.3.2 Using GGM to Examine M/EEG Networks

The application of graphical models to estimate M/EEG networks has been less prolific. In particular, graphical models have been mainly used to examine amplitude envelope based networks in MEG [43]. More recently [44–46] graphical models have been used to estimate networks from complex-valued data from different frequency bands which incorporate phase information. So far, GGMs have only been used to discriminate clinical states, identify commonalities between fMRI and M/EEG networks and establish characteristics of resting and task based networks [22, 43, 45]. Little empirical work exists comparing graphical models of M/EEG data to anatomical connectivity. We do this in detail in chapters 2 and 4.

1.3.3 Applying Graph Theory

Brain networks from graphical models are comprised of hundred or even thousands of connections. To make any sense of this across groups we could do statistical tests and correct for multiple comparisons. In contrast, graph theory offers an elegant counter approach. Graph theory examines the organizing characteristics of networks and thereby provides an efficient summary of the network.

Graph theory while useful to summarize networks depends on appropriate application i.e. valid assumptions [47]. One assumption when estimating graph theoretic metrics is that the distance (over the network) between two brain regions is correctly estimated. If we use

correlation to define a network, distance becomes corrupted due to indirect connections being present in the correlation. Graphical models on the other hand estimate direct connections and provide a sensible definition of distance.

In M/EEG, network estimation is made difficult due to common input effects, volume conduction/field spread and leakage effects. While using graphical models to estimate networks goes some way in reducing their impact, noise still affects network estimates. We examine in chapters 2 whether using graph theory instead as summary statistics helps further reduce the impact of noise.

1.4 Linking Structural to Functional Connectivity

The set of functional connections during the resting state between all pairs of brain areas is referred to as the functional connectome. One simple explanation for how the functional connectome might be generated is that neurons in one area of the brain project axons that synapse with neurons in another areas facilitating the correlation in neural activity recorded at the two locations. In practice establishing this simple mechanistic explanation for MEG/EEG/fMRI functional connectivity has proved immensely challenging.

In the past two decades tools (Diffusion Weighted Imaging + tractography) have been developed that allow us to non-invasively estimate axonal pathways. The set of all fiber tracts (axonal pathways) is referred to as the structural connectome. A number of studies have investigated relationship between the structural connectome and fMRI functional connectivity ([48–52]). Pairs of brain areas without a structural connection have significantly weaker functional connectivity strength [48], supporting a relationship between structural and functional connectivity. However, across these studies, the structural connectivity explains between 10 - 65 % ([53]) of the fMRI functional connectivity variance across different studies. Some of

this variability may be the results of using different ways to carve up the cortex into different brain areas and different measures of fMRI functional connectivity.

Fewer studies have examined the link between structural and functional connectomes in M/EEG data [54–57]. One study found that structural connectivity explained 23% of the variance in EEG coherence. Another study found structural connectivity explained 9% of the variance in EEG coherence. This latter study also showed that statistically, low structural connectivity was linked to low coherence. Structural connectivity explained 4% [56] MEG coherence in one study, while in another the structural connectivity explained 20% of the variance [57] (Spearman's rank correlation) when functional connectivity was estimated using amplitude envelope correlations. Some of the variability here lies in the source localization approach applied, the method of estimation of the functional connectivity and finally, the frequency band in which functional connectivity is estimated. Consistent with the fMRI literature, structural connectivity alone could potentially constrain the M/EEG functional connectivity, but only to a limited extent.

Current theories suggest the functional connectivity is driven both by mono-synaptic and poly-synaptic connections [49, 58] over the structural connectivity. These theories provide potential explanations for functional connectivity generation when it is estimated using correlation (or coherence). Correlation by definition (if C is correlated to A and B through structural connections, A and B are also correlated) permits poly-synaptic pathways to influence the functional connectivity strength, however, it is difficult to distinguish this from the pitfall of common inputs. One polysynaptic generative mechanism for the functional connectivity is that of Gaussian noise becoming correlated due to the anatomical connectivity. Given this model, we can use the graphical models to examine the effective connectivity which are "direct" connections between nodes representing potential connections in the structural connectome. A strong effective connectivity estimate implies that the relationship between two areas exists independent of their relationship to other potentially intermediary areas,

which may better reflect the wiring of the brain, and be more closely related to the structural connectome.

1.5 Structure of the Dissertation

In Chapter 2, we build methods to estimate graphical models for MEG frequency domain data, examining features of MEG data that emphasize slow and fast timescales of neural dynamics. We know that several problems make estimation of statistical dependence difficult - leakage effects and common input. We test the efficacy of effective connectivity and graph theory in approximating structure through extensive simulations. We apply our understanding to MEG data to see the ability to detect the influence of the structural connectome within individuals. We follow up this study by looking at the how variance in structural connectivity modifies the functional and effective connectivity across subjects. We use the case of stroke patients, who show heterogeneity in structural connectivity due to lesions in the brain, to examine the relationship of altered structural connectivity to effective connectivity as estimated with fMRI. Finally, we examine the same relationship, structure to function in stroke patients, but for two different subgroups of stroke patients - subacute ($<$ 1 month post stroke) and chronic ($>$2 months post stroke) when using EEG effective connectivity. Our work informs us of how structural connectivity constrains function across different spatial and temporal scales.

Chapter 2

Contribution of the Structural Connectome to different Temporal scales of MEG connectivity

2.1 Introduction

Functional connectivity (FC) in macroscopic brain data (fMRI, EEG, MEG) refers to evidence of statistical dependence between signals recorded in two different locations. This broad definition encompasses different measurement techniques, signal processing methods, and statistical models that emphasize different aspects of the underlying brain activity. MEG signals are sampled on a millisecond time scale capturing aggregate synaptic activity in populations of neurons. These neurophysiological signals have intrinsic time scales of dynamics, usually organized in terms of frequency bands that exhibit distinct behaviors in different cognitive tasks and clinical disease states [13, 59–62].

Functional connectivity in MEG is usually estimated within frequency bands, using a vari-

ety of methods that prioritize different time scales of dynamics. A widely used measure is coherence. Coherence is a measure of consistency of relative phase and relative amplitude within a frequency band between signals recorded in two areas. Consistent phase difference between two signals is equivalent to a consistent time delay between the signals. For instance a consistent 45 degree phase difference between two signals at 10 Hz corresponds to a 20 ms delay. Coherence has long been interpreted as reflecting consistent axonal delays along white-matter tracts of the brain [12, 27]. The communication through coherence theory suggests that the brain uses consistency in phase between areas to help in supporting communication between them, as this consistency in phase helps alignment of spikes and thereby communication between areas [2].

More recently, there have been a number of studies that investigated correlation of the amplitude envelope of MEG signals. The amplitude of an oscillatory signal only varies at time scales slower than period of the oscillations. Thus amplitude correlation investigates statistical structure at a much slower timescale on the order of 100s of milliseconds, or even seconds. The motivation for investigating correlation of the intensity of the signals (while ignoring the precise phase synchronization) is to match the time scales of MEG functional connectivity to fMRI functional connectivity. Indeed a number of studies have shown that correlation of the slow fluctuations of the MEG amplitude envelope in different frequency bands show similarities to fMRI resting-state networks [19, 23, 24, 63].

Studies of MEG functional connectivity commonly assume that correlation between brain areas is constrained by axonal pathways between regions (structural connectivity). However, several studies that have investigated the relationship of electrophysiological (MEG/EEG/ECoG) functional connectivity with structural connectivity have found variable results[56, 57]. One study found that group averaged structural connectivity explains only 4% [56] MEG functional connectivity (estimated using coherence) in one dataset while in another study [57], using the amplitude envelope and Spearman's rank correlation, structural connectivity ex-

plained 20% of the MEG functional connectivity variance. There are a number of potential causes for the variability across studies. First, all MEG (or EEG) based functional connectivity studies makes use of source localization algorithms that vary in approach and parameter choices across studies. Second, the frequency band(s) in which functional connectivity is estimated varies across studies. And finally, the statistical metric of functional connectivity, emphasizes different types of dynamics, e.g, amplitude or phase correlation.

While previous studies indicate a potential relationship between structural connectivity and MEG functional connectivity, the relationship is a weak one. Structural connectivity provides a substrate for communication over axonal fiber bundles with time delays on the order of milliseconds (cite) to conduct action potentials. Thus, on theoretical grounds, phase based estimates of connectivity, such as coherence, would be expected to have a close relationship to structural connectivity. However, empirically, MEG amplitude correlation is more closely related to fMRI functional connectivity [23, 24] which has been shown to correlate with structural connectivity [48, 53]. Both measures are susceptible to leakage effects and common input effects which can lead to the presence of false positive connections and poor estimates of connection strengths. Leakage effects occur when two sources in the brain aren't completely distinguishable via MEG source localization due to the nature of their location and orientation. Leakage effects show up as spurious correlated source activity. A second issue is common input effects - two sources receiving (either simultaneously or at a delay) activity from a third source will show correlated activity without any structural connection.

An accurate estimate of functional connectivity that reduces the influence of common inputs and leakage effects is crucial for studies examining the nature and dynamics of brain function using MEG, and by extension, increase the alignment of connectivity from MEG with the structural connectivity. *Effective connectivity* or *model based connectivity* estimates such as graphical models to estimate the precision (inverse of the covariance) potentially offer a better connectivity estimate which is more closely aligned with the underlying structural

connectivity. Precision estimates the *conditional dependence*, i.e., the strength of statistical dependence between two sources when accounting for variance shared with all other sources, thereby estimating "direct" connections between two sources. Estimating conditional dependencies reduces the problem of common inputs (and by extension false positive connections).

In this study we estimated two different graphical models for MEG effective connectivity at distinct time scales. The complex-valued Gaussian graphical model (cGGM) for millisecond time scale functional connectivity estimates effective connectivity for complex valued data accounting for both amplitude and phase [46]. The amplitude Gaussian graphical model (aGGM) estimates effective connectivity from the real-valued amplitude envelope and accounts for correlated amplitude fluctuations at slower time scales [43]. Both graphical models shared a common underlying structure based on the structural connectome. The complex valued Gaussian graphical model (cGGM) can be used to estimate the summary statistic of partial coherences on each edge, and amplitude Gaussian Graphical models to allow us to estimate the summary statistic of partial correlation on each edge. Partial coherence is an estimate of the conditional dependence structure between brain areas when accounting for shared variance across both amplitude and phase while partial correlation accounts only for amplitude. In empirical tests, Colclough et al. [64] showed that partial coherence appeared to be a slightly more consistent an estimate of connectivity over multiple sessions for the same subject relative to partial correlation. Further, both partial coherence and partial correlation appeared to be more consistent across multiple sessions relative to other measures of effective connectivity.

Networks from Graphical modelling provide a better approximation to the definition of an edge (connection) of a brain network needed for graph theoretical analysis[47]. Examinations of the brain network structure using various graph theoretic metrics have helped us understand brain function better (e.g., which areas are well connected? how are areas functionally organized?[49, 58, 65]) while also helping generate potential biomarkers for clinical

groups [60]. Graph theoretic metrics provide spatially reduced descriptions of networks that retain information about the structure of its connectivity. We see the process of representing a network using source level graph theoretic metrics as being akin to identifying summary statistics for probability distributions. These are summary statistics for connectivity information. We expect that by reducing the network using graph theoretic metrics we will further minimize the influence of leakage effects and common inputs and identify critical features of the networks estimated from the graphical models that are closely related in structural and functional connectivity.

In this paper, we examine different ways to summarize MEG networks between sources in the brain. We identify which methods of modeling effective connectivity provide greater alignment to structural connectivity in simulations. We examine for the first time (to our knowledge) which frequency bands and what statistical features of MEG data (phase versus amplitude) are more tightly facilitated by the structural connectivity. We expect that effective connectivity (from graphical models) provides estimates of direct connections between sources which reflect the structural connectivity more closely. Additionally, we examine through simulations if using graph theory leads to increased accuracy in characterizing structural connectivity relative to the edge weights from the full network (from partial coherence or partial correlation). The central question of this study is determine which aspects of network topology are better preserved after source localization and effective connectivity estimation across a range of signal-to-noise ratios and to apply this knowledge to examine networks in MEG data.

2.2 Methods

2.2.1 Modeling Framework

Overview

A template of brain connectivity was developed for use in the simulation studies and MEG data analysis presented here. This model is based on tractography analysis of the group average template of DTI constructed from 842 subjects from the HCP 842 data set (Yeh et al., 2018). We combine these streamlines with the Lausanne parcellation [66] to define 129 regions of interest (ROI) and a structural connectivity model. The Lausanne parcellation was also used to define a source model for MEG simulations and inverse solutions.

At the core of the simulation and data analytic strategy presented here is the notion that the structural connectivity model constrains the statistics of MEG signals. We develop two multivariate Gaussian models of effective connectivity to constrain the source activity: (1) complex-valued Gaussian graphical model, where the structural connectivity determines the precision (inverse covariance) of the complex-valued multivariate normal distribution that generates the *amplitude and phase* of source activity in a frequency band, and (2) amplitude Gaussian graphical model, where the structural connectivity determines the precision of a multivariate normal distribution that generates the *amplitude envelope* of source activity in a frequency band. The first model is a generative model of coherence, as widely used in EEG and MEG studies ([21, 26, 27]). The second model is a generative model of amplitude correlation which has been recently introduced in the MEG literature, as an analog of fMRI functional networks [19, 24, 67].

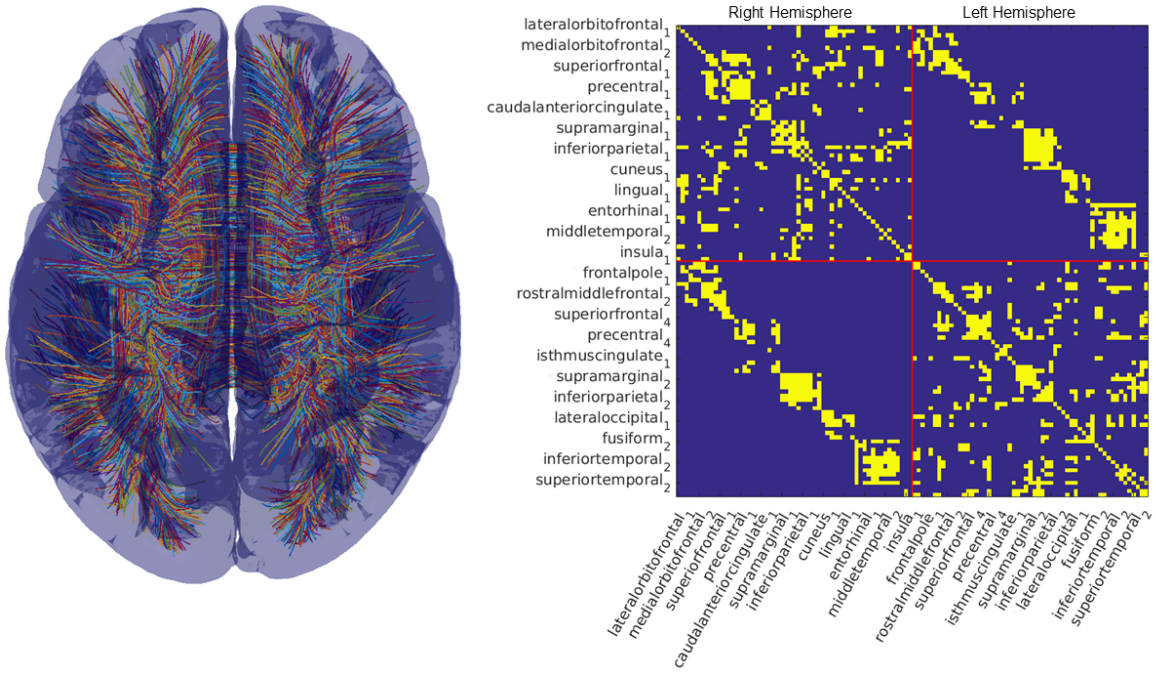

Figure 2.1: Structural Connectome: We show the streamlines derived from [68] on the right and the structural connectome for the 114 areas of the Lausanne parcellation on the left. We show the binarized SC, with any non-zero edge being assigned a weight of 1.

Structural Connectome (SC) Model

We used streamlines generated with deterministic tractography by Yeh et al. [68] using the HCP842 dataset [8] transformed to the MNI152 template brain pulled from FSL. We transformed the Lausanne parcellation [66] of 114 cortical and 15 subcortical ROIs to the MNI152 template brain and generated a volumetric representation for each ROI using the *easy_lausanne* toolbox (Cieslak, 2015). Each streamline was approximated by a single 100-point cubic spline using code adapted from the along-tract-stats toolbox [69]. By identifying the streamlines which ended in a pair of ROIs we were able to create the structural connectome for the Lausanne parcellation. Each streamline only connected a single pair of ROIs. Any edge $W_{ij}$was defined as (for ROIs i and j connected by streamlines s of length l):

$$W_{ij} = \sum_{s_{ij}} \frac{1}{l_{ij}} \tag{2.1}$$

We weight the streamlines by length to reduce the bias of tractography algorithms towards longer streamlines [70]. From this process we built the $129 * 129$ weighted structural connectome with 1132 edges. We reduced this matrix to $114 * 114$ with 720 edges (see Figure 1) after removing all the subcortical structures and limiting interhemispheric connections to known homologous white-matter tracts. This latter step helped remove potentially noisy estimates of connections where streamlines intersected and passed outside the cortical surface before reaching the terminal point in a brain region. The resulting model of structural connectivity shown in Figure 1 is referred to as the structural connectome (SC). This model is incomplete in that it does not include thalamocortical projections, and thus there maybe functional connectivity that is a result of structural connections outside of this SC. Our estimation procedure described in the next section allows for such connections.

Effective Connectivity Model - Complex Valued Gaussian Graphical Model (cGGM)

The template of structural connectivity derived from HCP 842 (Yeh et al., 2018) gives us potential constraints on the connection strengths between ROIs, and more importantly, which ROIs are not connected by white-matter tracts observable with DTI. In order to use this information to simulate current source activity and to model MEG data, we assume that the vector of source activity ($\mathbf{Z}$) at all ROIs in one frequency band are samples drawn from a **complex-valued** multivariate Gaussian random process (where Φ is the precision):

$$\mathbf{Z} \sim N(\mathbf{0}, \mathbf{\Phi}) \tag{2.2}$$

The band-limited MEG signal is characterized by samples of amplitude and phase, or equivalently, by analytic signal coefficients with real and imaginary parts corresponding to sine and cosine components of the signal in each epoch. For frequency domain data that are complex-valued, we make use of a complex-valued multivariate normal distribution.

The complex-valued multivariate Normal for a zero-mean (where $E(\mathbf{Z}) = 0$) complex-valued Gaussian process [71] is defined as:

$$\rho(\mathbf{Z}) = \frac{1}{\pi^n det^{\frac{1}{2}}(\mathbf{\Theta})} \exp\left(-\frac{1}{2}\mathbf{Z}\mathbf{\Theta}^{-1}\mathbf{Z}^H\right) \tag{2.3}$$

where

$$\mathbf{\Theta} = \begin{bmatrix} \mathbf{R_{zz}} & \widetilde{\mathbf{R}}_{\mathbf{zz}} \\ \widetilde{\mathbf{R}}_{\mathbf{zz}}^H & \mathbf{R_{zz}}^H \end{bmatrix} \tag{2.4}$$

and

$$\mathbf{R_{zz}} = E[\mathbf{z}\mathbf{z}^H]; \widetilde{\mathbf{R}}_{\mathbf{zz}} = E[\mathbf{z}\mathbf{z}^T] \tag{2.5}$$

The key parameter in this model is the covariance matrix $\mathbf{\Theta}$ and its inverse, the precision matrix $\mathbf{\Phi} = \mathbf{\Theta}^{-1}$. As defined in equation and , the covariance matrix for complex valued data is composed of the familiar cross-spectrum $\mathbf{R_{zz}}$ and the complementary cross-spectrum $\widetilde{\mathbf{R}}_{\mathbf{zz}}$. Most spectral analysis methods only make use of R_{zz} and implicitly assume circular symmetry, i.e., $R_{z_1 z_2} = 0$ (Schrier and Scharf, 2010 [71]). In this case, the complex-valued data is labeled as *proper*. With the assumption of circular symmetry, we can parameterize the complex-valued Gaussian using the precision defined as the inverse of the cross-spectrum, $\mathbf{\Phi} = \mathbf{\Theta}^{-1} = \mathbf{R_{zz}}^{-1}$.

Each value in the precision matrix $\mathbf{\Phi}$ is the conditional covariance between any two variables (here, sources representing two ROIs) given the other variables (here, sources representing all other ROIs). The precision removes linear effects from all other sources from the covariance between any pair of sources, and provides a model of *effective connectivity* between sources. For any pair of sources, if the precision is zero, there is no need for a direct connection

between the sources in order to account for observed coherence (functional connectivity). Such apparent coherences arise from connections mediated via other sources in the model.

In our model, the precision matrix $\mathbf{\Phi}$ captures the statistics of effective connectivity and has nonzero entries only at edges (pairs of ROIs) that have a connection estimated from DTI in the structural connectome (SC). We are assuming that in each frequency band the connectivity we estimate arises from random fluctuations at each area becoming correlated by the structural connectome. This generative model of the source activity giving rise to MEG signals is used in the simulation studies. In the MEG data analysis, we estimate the source precision matrix $\mathbf{\Phi}$ from the MEG data in each frequency using graphical modeling techniques that inform the precision estimate with the SC estimated from the HCP-842, but allowing the precision values to be determined by the data.

Effective connectivity model - Amplitude Gaussian Graphical Model (aGGM)

We use the structural connectivity to constrain potential connections due to correlated amplitude envelope fluctuations between ROIs, thereby defining the generative model of amplitude correlation. We assume that the vector of source activity amplitudes ($\mathbf{X}$) at all ROIs in one frequency band are samples drawn from a **real-valued** multivariate Gaussian random process (where Φ is the precision with non-zeros entries where there are structural connectome connections):

$$\boldsymbol{X} \sim N(\mathbf{0}, \mathbf{\Phi}) \tag{2.6}$$

When examining amplitude, we look at samples X of amplitude estimates from the analytic signal of bandpass filtered MEG signal across epochs. So for amplitude data we use a real valued multivariate normal distribution as characterizing the fluctuations of amplitudes in different frequency bands. And the multivariate normal for a zero mean, i.e., (where

$E(\boldsymbol{X}) = 0)$ is defined as:

$$\rho(\boldsymbol{X}) = \frac{1}{\pi^n det^{\frac{1}{2}}(\boldsymbol{\Theta})} \exp\left(-\frac{1}{2}\boldsymbol{X}\boldsymbol{\Theta}^{-1}\boldsymbol{X}^T\right) \tag{2.7}$$

This distribution is fully parameterized by the precision matrix $\boldsymbol{\Phi} = \boldsymbol{\Theta}^{-1}$. Each value in the precision matrix $\boldsymbol{\Phi}$ is the conditional covariance between the amplitude envelope of any two sources given the other sources. The precision provides a model of *amplitude envelope effective connectivity* between sources. For any pair of sources, if the precision is zero, there is no need for a direct connection between the sources in order to account for observed amplitude envelope correlation (functional connectivity).

In our graphical model of amplitude fluctuations, the precision matrix $\boldsymbol{\Phi}$ captures the statistics of effective connectivity and has nonzero entries only at edges (pairs of ROIs) that have a connection estimated from DTI in the structural connectome (SC). We are assuming that in each frequency band the connectivity we estimate arises from random fluctuations in amplitude envelopes at each area becoming correlated by the SC. In the MEG data analysis (both for the simulation and real data), we estimate the source precision matrix $\boldsymbol{\Phi}$ in each frequency band using graphical modeling techniques that inform the precision estimate with the SC estimated from the HCP-842, but allowing the precision values (edge weights) to be determined by the data.

MEG Forward Model

The MEG forward model is an estimate of the magnetic field measured at MEG sensors above the scalp generated by current sources located in the brain. For both the simulations and the data analysis presented in this paper, we made use of the orthogonal pair of planar gradiometer coils at 102 locations above the scalp (shown in in Figure 2.2). Planar gra-

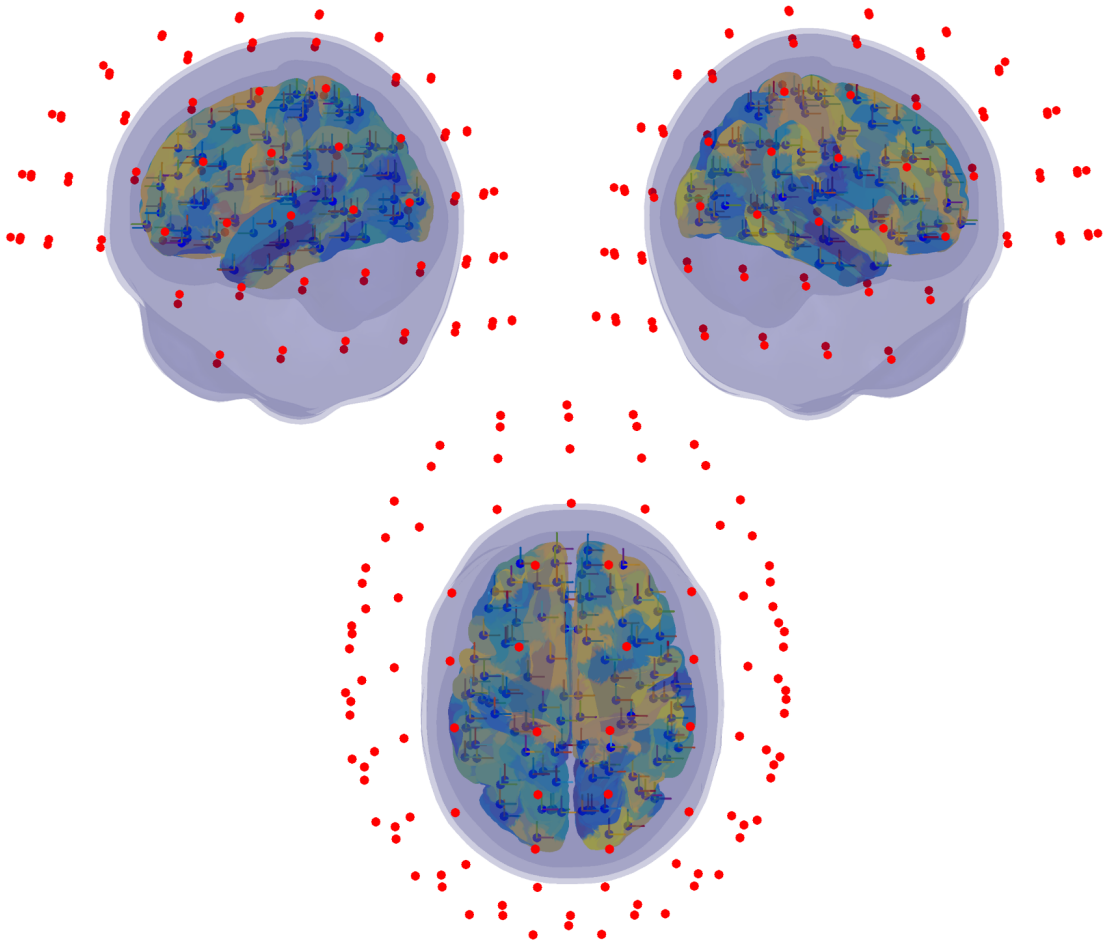

Figure 2.2: MEG Forward Model: We show the brain, with x, y, z oriented dipoles for each brain region of interest, the CSF, skull and scalp boundaries and the location of MEG gradiometers with respect to the scalp for the $fsaverage$ head. Each of 102 red dots indicates the location of a pair of orthogonal planar gradiometers.

diometer coils have higher spatial resolution than magnetometer coils [72], which we did not consider in this study.

The head model was developed from the fsaverage MRI images from the Freesurfer toolbox [73]. The tesselated cortical surfaces for right and left hemisphere were extracted using the recon-all pipeline in Freesurfer and then downsampled to 81000 (81k) vertices (*mris_decimate* from Freesurfer). We used this surface to constrain dipole orientation and define the volume of the model corresponding to the cortex. We generated the inner skull,

outer skull and scalp surfaces approximated with 2562 vertices from the fsaverage head generated using the *mri_watershed* function. Using these surfaces, and with the conductivities of scalp, CSF and brain set at 1 S/m and the skull at 0.025 S/m (i.e., 40 times lower conductivity), we used OpenMEEG [74] to compute a Boundary Element Model (BEM) to generate the MEG forward matrix. Each row of the MEG forward matrix is the magnetic field gradient detected across all 204 gradiometers from a unit current density source at one of the 81k cortical surface vertices (expected to be maximum in the part of the cortex immediately below the gradiometer).

Using the Lausanne parcellation for 114 cortical ROIs [66], we divided the cortical surface and identified vertices belonging to each ROI using the volumetric parcellation of the fsaverage brain. Using this organization of vertices we then reduced the representation for each ROI down to a set of 3 dipoles in the x, y and z directions at a single location. The location for each ROI (Loc_i for the i'th ROI) was selected by taking a weighted average of vertex locations (V_{ij} for the j'th vertex of the i'th ROI), using the following equation (where c is channels and W represents the number of vertices in an ROI):

$$Loc_i = \frac{1}{\sum_{j=1:W} \sum_{c=1:256} L_{ijc}^2} \sum_{j=1:W} ((\sum_{c=1:256} L_{ijc}^2) * V_{ij}) \tag{2.8}$$

In this way we reduced our source model to 114 source locations, with 3 sources at each location in the canonical x,y, and z directions. We computed a new MEG forward matrix ($\boldsymbol{M}$) of dimension 204 * 342 using OpenMEEG. This MEG forward matrix approximates the (linear) mixing of source activity at the gradiometers to generate the measured MEG signals, and will be used in the inverse solution discussed in the section on estimation of the model.

2.2.2 Estimation of Effective Connectivity

Overview

The estimation of the complex-valued Gaussian graphical model or the amplitude Gaussian graphical model from the MEG data proceeds in three steps. First, MEG data is bandpass filtered into each frequency band of interest. Second, an inverse solution is applied to estimate the source activity over the observations. After the inverse solution, the Hilbert Transform is used to estimate amplitude and phase of the signals. The average of the analytic signal over seconds represents ensemble activity over sources. Third, graphical modelling methods are used to estimate the precision matrix of a Gaussian graphical model of the effective connectivity. Graphical modeling involves the choice of regularization parameters and these parameters are selected by cross-validation. The estimation procedure is tested through a set of simulation studies discussed in the next section.

Inverse Solution to estimate source activity from MEG

We can represent each sample of the MEG data within a frequency band, after bandpass filtering, as a vector $\boldsymbol{B}$ of length equal to the number of MEG sensors. The set of samples of $\boldsymbol{B}$ is related to source activity $\boldsymbol{S}$ of length equal to the number of MEG sources

$$\boldsymbol{B} = \boldsymbol{M}\boldsymbol{S} \tag{2.9}$$

where $\boldsymbol{M}$ is the MEG forward matrix. For each participant, we localized activity to the 342 sources by inverting the reduced lead field using regularized minimum norm estimation (weighted L2 norm [29]) and applying it to data at the scalp. We estimate the inverse $\boldsymbol{M}^{-}$

using (where ν is a penalization):

$$diag(\boldsymbol{W}) = ||\boldsymbol{M}||_2^5 \tag{2.10}$$

$$\boldsymbol{M}^- = (\boldsymbol{MW})^T((\boldsymbol{MW})^T * (\boldsymbol{MW}) \ + \ \nu I)^{-1} \tag{2.11}$$

The estimated source activity $\boldsymbol{S} = \boldsymbol{M}^-\boldsymbol{B}$. We identify the time series for the three dipoles along the x, y and z directions.Using a singular value decomposition at each ROI we identified the optimal orientation of the dipole as the first singular vector. Using the first singular vector at each ROI, we reduced the lead field from 204x342 to 204x114. This reduced lead field was the individual specific (adaptive) lead field. We source localized data to the 114 ROIs for the individual lead field.

Frequency-domain transformation

Source localized data at each ROI is Hilbert transformed to yield the analytic signal $\boldsymbol{A}$ which is complex valued. We reduced $\boldsymbol{A}$ by averaging either $\boldsymbol{A}$ over each second of data to get an ensemble of complex-valued data that capture the amplitude and phase of the signals or $|\boldsymbol{A}|$ (absolute value of A) to get an ensemble of the real valued amplitude data.

Adaptive Graphical Lasso using SC-QUIC

The graphical lasso [32] is a method that has been applied in multiple fields in the past decade, from genomics [75], to fMRI functional connectivity ([76], [37]) and climate models [77]. This is a method used to identify a sparse approximation to the precision matrix. In this way, estimates in the precision are more robust for the values that are retained. In order to apply the lasso, we use the penalized likelihood function as follows ([33]) to estimate the

precision (where Θ is the covariance or cross-spectral density):

$$\hat{\mathbf{\Phi}} = argmin_{\mathbf{\Phi} \succ 0} \left(-log(det\mathbf{\Phi}) + tr(\mathbf{\Theta}\mathbf{\Phi}) + \lambda \sum_{j<k} |\mathbf{\Phi}_{jk}| \right) \tag{2.12}$$

The penalization parameter λ in the graphical lasso determines the important set of cGGM/aGGM precision values. The output of the lasso from Equation 4.12 is the precision matrix $\hat{\mathbf{\Phi}}$, which represents directly the complex Gaussian Graphical (cGGM) or amplitude Gaussian Graphical model. Our purpose was to make use of the lasso that takes advantage of our prior knowledge of the structural connectome (SC) which are the likely locations of nonzero precision values. We made use of the lasso optimization from QUIC ([78]) using a matrix penalty term (this process is also called the adaptive lasso - [79]) determined by the SC with edges W (and $\lambda_1 = \lambda_2$):

$$\hat{\mathbf{\Phi}} = argmin_{\mathbf{\Phi} \succ 0} \tag{2.13}$$

$$\left(-log(det\mathbf{\Phi}) + tr(\mathbf{\Theta}\mathbf{\Phi}) + \lambda_1 * \sum_{j<k; W_{jk} \in SC} |\mathbf{\Phi}_{jk}| + \lambda_2 * \sum_{j<k; \boldsymbol{W}_{jk} \notin SC} |\mathbf{\Phi}_{jk}| \right) \tag{2.14}$$

Note that in the limiting case of $\lambda_1 = \lambda_2$ we are using the same likelihood as the graphical lasso. Past work along these lines [43] has used the SC weights directly to determine the penalization weighting, which imposes more structure that appropriate. We expect that the SC weights will potentially constrain connectivity strengths. However, we do not expect the SC strengths to map directly onto the effective connectivity strengths due to individual differences, and variations within individuals across brain states. By using a template, we are assuming a common SC across participants, so the expected weight may differ. Further, the SC can be expected to be used differently across frequency bands yielding different effective

connection weights. For this reason we use the binarized SC to determine the penalization structure. We estimated the penalization values λ_1 and λ_2 using cross validation as described in the next section.

By optimizing the above penalized likelihood, we leveraged the information in the SC as a prior for our lasso estimate. The output of the lasso when optimizing Equation 3.3 is the (c/a)GGM. We derive our graph G with vertices $V = 1, 2, ...C$ and edges $W_{est} = G_{ij} = 1, i, j \in V$ from the (c/a)GGM based on the non-zero values in $\hat{\mathbf{\Phi}}$. The final precision matrix $\tilde{\mathbf{\Phi}}$ is estimated under the Gaussian likelihood for the set of edges $\boldsymbol{W}_{est}$ defined by the graphical model using the function $ggmFitHtf$ (PMTK3 toolbox [80]) which optimizes (unpenalized Gaussian log-likelihood):

$$\tilde{\mathbf{\Phi}} = argmin_{\Phi \succ 0; |\Phi| > 0 = G} - (log(det\Phi) + tr((\Theta + \delta * I)\Phi)) \tag{2.15}$$

Since $\mathbf{\Theta}$ (covariance) is usually rank deficient, we add a small value (δ) along the diagonal to make it full rank. We define *delta* as 0.001 times the maximum value along the upper triangle of the covariance.

Cross-validation

The adaptive graphical lasso imposes the structural connectome (SC) onto the functional data potentially allowing for more robust reconstructions of the precision. We tested whether the adaptive graphical lasso produced estimates of the precision that show reduced error relative to applying the graphical lasso. Note that applying the graphical lasso would be equivalent to having the penalization inside and outside the SC be equal i.e. $\lambda_1 = \lambda_2$. We estimated the appropriate value for λ_1 and λ_2 using cross validation.

We split the MEG data (both simulation and real data) into four contiguous pieces of 120

samples each. We estimated the precision $\tilde{\Phi}_i$ on one segment of the data (i) and estimated the deviance when using this precision as the inverse for the covariance $\mathbf{\Theta}_j$ for all the other segments j of the data (and vice versa). Deviance was estimated as:

$$Dev = \sum_{i=1:4} \sum_{j=1:4; j \neq i} (-log(det\ \tilde{\Phi}_i) + tr(\Theta_j \tilde{\Phi}_i)) \tag{2.16}$$

We found that (in the majority of cases), both in simulation and in data, using the prior of the SC proved useful and reduced cross validated deviance relative to using graphical lasso directly, i.e., the minimum cross-validated deviance always occurred with $\lambda_1 < \lambda_2$.

Summary Statistics - Partial Coherence and Partial Amplitude Correlation

In every frequency band, or for each iteration of our simulation, we estimated two graphical models. We estimated the complex Gaussian Graphical model to estimate the precision for complex valued data incorporating amplitude and phase and the amplitude Gaussian Graphical model for the real valued amplitude data. For the cGGM we estimate the partial coherence (PC) as a summary statistic [81]:

$$PC_{z_1 z_2} = \left| \frac{\Phi_{z_1 z_2}}{\sqrt{\Phi_{z_1 z_1} * \Phi_{z_2 z_2}}} \right|^2 \tag{2.17}$$

For the aGGM we estimate the amplitude partial correlation (APC) as a summary statistic as (assuming the precision matrix Φ here is the output from estimating an aGGM):

$$APC_{x_1x_2} = \left| \frac{\Phi_{x_1x_2}}{\sqrt{\Phi_{x_1x_1} * \Phi_{x_2x_2}}} \right| \tag{2.18}$$

Summary Statistics - Graph Theory

In silico we compare the accuracy of using the estimates for PC and APC relative to using reduced characteristics of networks derived from graph theory. Graph theory being a summary of the network potentially boosts the accuracy in estimating network characteristics. We derive our graph G with vertices $V = 1, 2, ...114$ and edges $W_{est} = G_{ij} = PC_{ij}$ or $APC_{ij}, i, j \in V$ from the graphical model based on the non-zero values. We estimate graph theoretic metrics using the Brain Connectivity Toolbox [82]. We make use of several measures in this study:

1. The basic measure of a network is the **degree** of a node (connectivity), that is, the number of edges a node shares with other nodes in an undirected graph. This measures how many nodes can communicate with any given node.

2. The local integration of functional clusters of the network is measured by the **clustering coefficient**. The clustering coefficient is the ratio of the number of triangles to number of triples in a network and helps give an estimate of how often nodes one degree apart are connected to one another.

$$C_i = \frac{number\ of\ triangles\ connected\ to\ node\ i}{number\ of\ possible\ triangles\ centered\ on\ vertex\ i} \tag{2.19}$$

$$C = \frac{1}{n} \sum_i C_i \tag{2.20}$$

3. A metric that describes the global segregation of the network is the **path length**.

Path length (L) is the average shortest path (d) between all pairs of nodes.

$$L = \frac{1}{\frac{1}{2}n(n+1)} \sum_{i \leq k} d_{ij} \tag{2.21}$$

4. **Closeness Centrality** uses the path length matrix between every pair of nodes to define centrality. The closeness centrality for a node is the average path from it to all other nodes in the largest connected network. It is defined as:

$$C_{Cent} = \frac{N}{\sum_{j=1:n} L_{ij}} \tag{2.22}$$

5. **Betweenness Centrality** is an estimate of how central a node is based on the number of shortest paths it participates in. A node which lies on more shortest paths in a network has a higher betweenness centrality.

6. **Eigenvector Centrality** is an estimate of the closeness of a node to nodes that are strongly connected to the rest of the network.

The closeness centrality and betweenness centrality can only be estimated for a connected network. Some reconstructed partial coherence and partial correlation networks weren't fully connected. When the network had multiple connected components we selected the largest connected component and estimated closeness and betweenness centrality for that component alone. In the majority of cases this component tended to include over 100 (out of 114) sources.

2.2.3 Simulations

Overview

We simulate effective connectivity from the structural connectome by assuming that the structural connectome weights constrain the precision matrix for a circularly symmetric complex-valued multivariate normal distribution. In the simulations, we generate novel networks with random weights for edges. While the edge locations are always retained, we randomized the weights on the edges by shuffling the original weights across edges. Each edges was then multiplied with a uniform random value between $\{-1, 1\}$. Finally, each edge is assigned a random phase based on sampling from a uniform distribution for conduction velocities between $\{4, 14\}m/s$ applied to estimated streamline lengths [12]. We then generate random weights for the diagonal and ensure positive definiteness of the precision matrix. This is the complex valued, circularly symmetric precision matrix ($\mathbf{\Phi}$) representing the precision matrix for a frequency band. We match the data analysis for real data by working with 4 epochs of 120 samples each when estimating the appropriate penalization for the adaptive graphical lasso using cross validation.

Cross Spectral Density and Amplitude Covariance

Using the previously defined precision, we can generate the cross spectral density (covariance) as its inverse ($\mathbf{\Theta} = \mathbf{\Phi}^{-1}$). As the CSD has a real-valued equivalent[71],treating real and imaginary components as separated variables governed by the single covariance structure, we sample $480x114$ complex Gaussian values using the Matlab function *mvnrnd* operating on the equivalent real-valued covariance matrix. The complex-valued samples are used to estimate the cross spectrum (covariance) $\hat{\mathbf{\Theta}}$ and its inverse, the precision $\hat{\mathbf{\Phi}}$). We normalize the precision to get the partial coherence following equation 2.17.

We get the amplitude estimates by taking the absolute value for all $480x114$ samples i.e. $\boldsymbol{X}_{amp} = |\boldsymbol{X}|$. Using this data we estimate the original amplitude covariance and invert it to estimate the amplitude precision matrix. The normalized amplitude precision is the amplitude partial correlation (see Eq. 3.7) .

The estimated source partial coherence and amplitude partial correlation at this stage serve as the optimal solutions if we were directly measuring sources. We compare all reconstructed estimates (after forward modeling data, source localization and adaptive graphical lasso) to these matrices.

Forward Solution and Source Localization

As described earlier we built our MEG forward matrix from 114 sources using the fsaverage head projecting to MEG gradiometers. We simulated sources of different orientations on every run of our simulation. Complex-valued data (Z) is projected using this forward matrix (see Eq 2.9) to the sensors. Noise is added to all sensors while controlling SNR, estimated as (C is sensor covariance, and N is noise covariance):

$$SNR = 10 * log_{10}(\frac{trace(C)}{trace(N)}) \tag{2.23}$$

We examined reconstruction of networks with SNR of approximately 1, 5, 10, 20, 30 and 50 dB. Source localization was performed using weighted L2 norm inverse solutions as discussed in section 2.2.2. We generated inverse solutions across a range of penalizations and examined correlation between reconstructed cross spectrum and original source cross spectrum. We chose the optimal penalization based on the value that yielded maximum correlation between the reconstructed cross spectrum and original source cross spectrum.

Estimating Partial Coherence and Partial Correlation

After source localization, we have 480 samples of analytic signal at 114 sources. Using this data we estimate the CSD and the amplitude covariance which serves as the input to the adaptive graphical lasso. To run our structural connectome (SC) based models, we need to decide on two penalization values: penalization inside the SC edges - λ_1 and penalization outside the SC edges - λ_2. We decide these values based on cross validation. This procedure is discussed in detail in the section on Cross validation.

Estimating Accuracy of Network Reconstruction

We examined reconstruction error for both sets of graphical models (partial coherence and partial correlation) and error of graph theoretic metrics. Reliability of effective connectivity reconstruction was assessed in two ways. First, we examined the sensitivity and false discovery rate in simulations since we possessed a ground truth of the structural connectome (SC) that give rise to the observed covariance. Sensitivity was estimated as:

$$S = \frac{\sum(W_{est} \in W_{SC})}{\sum(W_{SC})} \tag{2.24}$$

Sensitivity tells us the ratio of edges recovered within the structural connectome relative to the total number of SC edges. A higher value of sensitivity indicates we are able to recover more edges from the SC. Note that the relevance of using sensitivity as a measure of performance when we have biased our estimates with the SC comes from the virtue of deciding the penalization values based on cross validation. In our procedure, it is inherently possible for there to be a effective connectivity model identified by the adaptive graphical lasso that does not use the SC prior at all, i.e. $\lambda_1 = \lambda_2$ is the optimal solution (minimum deviance in cross-validation).

We also examined the false discovery rate or FDR, which was defined as:

$$FDR = \frac{\sum(W_{est} \notin W_{SC})}{\sum(W_{est})} \tag{2.25}$$

FDR is the ratio of number of false positive edges estimates, i.e. edges outside the SC, relative to the total number of edges being estimated. An FDR of 0.5 indicates that of the, say 100 edges estimated, 50 edges were outside the SC. Note that there is a difference in interpretation of the FDR in simulations vs in real data. While in simulations, we know the ground truth (SC), in real data, there is the influence of thalamocortical connections and neuromodulatory systems which can lead to an increased "False Discovery Rate". Thus, in data the FDR can be (potentially) interpreted as edges necessary to the model rather than directly as false positives.

We also examined reconstruction of original connection weights. We estimated the Pearson correlation between the Fisher r-to-z transformed original, sampling based estimate of the partial coherence/correlation with the Fisher r-to-z transformed reconstructed estimate over the set of SC edges as well as edges estimated ($W_{est} \cup W_{SC}$).

Finally, we used Spearman rank correlation to correlate the different graph theory metrics estimated from the original and reconstructed networks.

2.2.4 Application to MEG data

MEG Data

We wanted to examine whether we saw similar results as we did in our simulation when we applied our methods to real data. Data collection and sharing for this work was provided by the Cambridge Centre for Ageing and Neuroscience (CamCAN). CamCAN funding was

provided by the UK Biotechnology and Biological Sciences Research Council (grant number BB/H008217/1), together with support from the UK Medical Research Council and University of Cambridge, UK. This data was obtained from the CamCAN repository (available at http://www.mrc-cbu.cam.ac.uk/datasets/camcan/), (Taylor et al., 2016, Shafto et al., 2015).

The MEG data was collected using a 306 sensor VectorView MEG system (Electa Neuromag, Helsinki). The 306 sensors consisted of 102 magnetometers and 204 planar gradiometers. As planar gradiometers have much higher spatial resolution than magnetometers, we focused the analysis in this paper on the planar gradiometer data. The data were sampled at 1000 Hz and highpass filtered at 0.3 Hz. This data was run through temporal signal space separation (tSSS, Taulu et al., 2005; MaxFilter 2.2, Elekta Neuromag Oy, Helsinki, Finland) to remove noise from external sources and to help correct for head movements (location of the head was continuously estimated using Head Position Indicator coils). Maxfilter was also used to remove the 50 Hz line noise and also to automatically detect and reconstruct noisy channels.

Spectral Analysis

We extracted 480 seconds of resting state gradiometer data for individuals aged between 30 to 40 years of age. This yielded 91 subjects (50 male). We first applied a bandpass filter between 0.5 to 100 Hz and a notch filter at 50 Hz to remove line noise. We then bandpass filtered data (elliptic filters with stop band set to 0.5 Hz below and above pass band, stopband attenuation set to 100 dB, and passband ripple set to 0.02) into five bands: delta (1-3 Hz), theta (4-7 Hz), alpha (8-13 Hz), beta (14-29 Hz) and gamma (30-80 Hz). For each subject, and within each band we optimized the dipole orientation across 114 ROIs as described in section 2.2.2. Source localized data was Hilbert transformed and the analytic signal A was computed.

We split the analytic signal A into 1 second epochs so that we have a 480x1000x114 matrix for each frequency band. As input for estimating the cGGM, the complex valued data we used was derived by averaging the original complex valued analytic signal over each second. We split the 480 samples from 114 sources into 4 continuous epochs of 120 samples each based on the expectation that we would have robust, stationary networks estimable with 120 seconds [83] and this also allowed for extensive cross-validation. As input for estimating the aGGM, we estimated amplitude envelope data by taking the absolute value of A and averaging it over 1 second segments. We then followed the same procedure as described earlier in the section 2.2.2 on Cross Validation before estimating the summary statistics from the cGGMs as the partial coherence and from the aGGMs as the amplitude partial correlation. Thus, we had at the end of the analysis for each subject, 5 graphical models (across all frequency bands) of cGGM and 5 graphical models of aGGM.

Alignment to SC

We examined sensitivity and false discovery rate (FDR) of the estimated cGGM and aGGM networks across different frequency bands and all subjects. A higher sensitivity and lower FDR indicates better alignment to the SC. In application to real MEG data its important to note that unlike the simulation studies FDR in data analysis indicates edges needed to model the effective connectivity that are not in the structural connectome (SC). This is to be expected since the SC is an estimate of anatomical connectivity based on a group average, and that the SC we are using does not include connections mediated by subcortical structures. These latter connections would appear as edges outside the SC. Thus FDR in the MEG data analysis is a measure of whether the SC is a good model for effective connectivity in the MEG data.

In addition, we used the other summary statistics discussed previously - metrics from graph theory. Using the graph theoretic metrics that were most accurate in our simulations we

categorized centrality of the cGGM and aGGM networks. We estimated the median centrality across all subjects for the frequency bands with the highest sensitivity in the cGGM and aGGM networks. We used a Spearman rank correlation to compare it to the estimated centrality from the weighted structural connectome.

2.3 Results

2.3.1 Simulation

We ran 500 iterations of our simulation where on each iteration a novel network was generated that represented the complex valued precision in a single frequency band. This precision had non-zero edges only at SC edges. We then forward modeled data generated from this precision (480 samples) to the MEG sensors before source localizing it to see the extent to which we can reconstruct the SC network. We reconstructed the precision using the cGGM and aGGM before estimating summary statistics. We understood the reconstruction performance of the full network using sensitivity (what percent of the SC edges were detected?), FDR (of total edges, how many are false positives?) and correlation of reconstructed weights with the original weights. We compared the correlation of weights to the correlation of reconstructed network graph theory metrics with the original network characteristics.

Partial Coherence more sensitive to SC than Partial Correlation

From the reconstructed precision using the cGGM and aGGM, we estimated the partial coherence (PC) and amplitude partial correlation (APC) respectively. We then estimated sensitivity, false discovery rate (FDR) and correlation. Sensitivity and FDR are estimated using the binarized PC and APC (using non-zero edges) and compared to the binarized

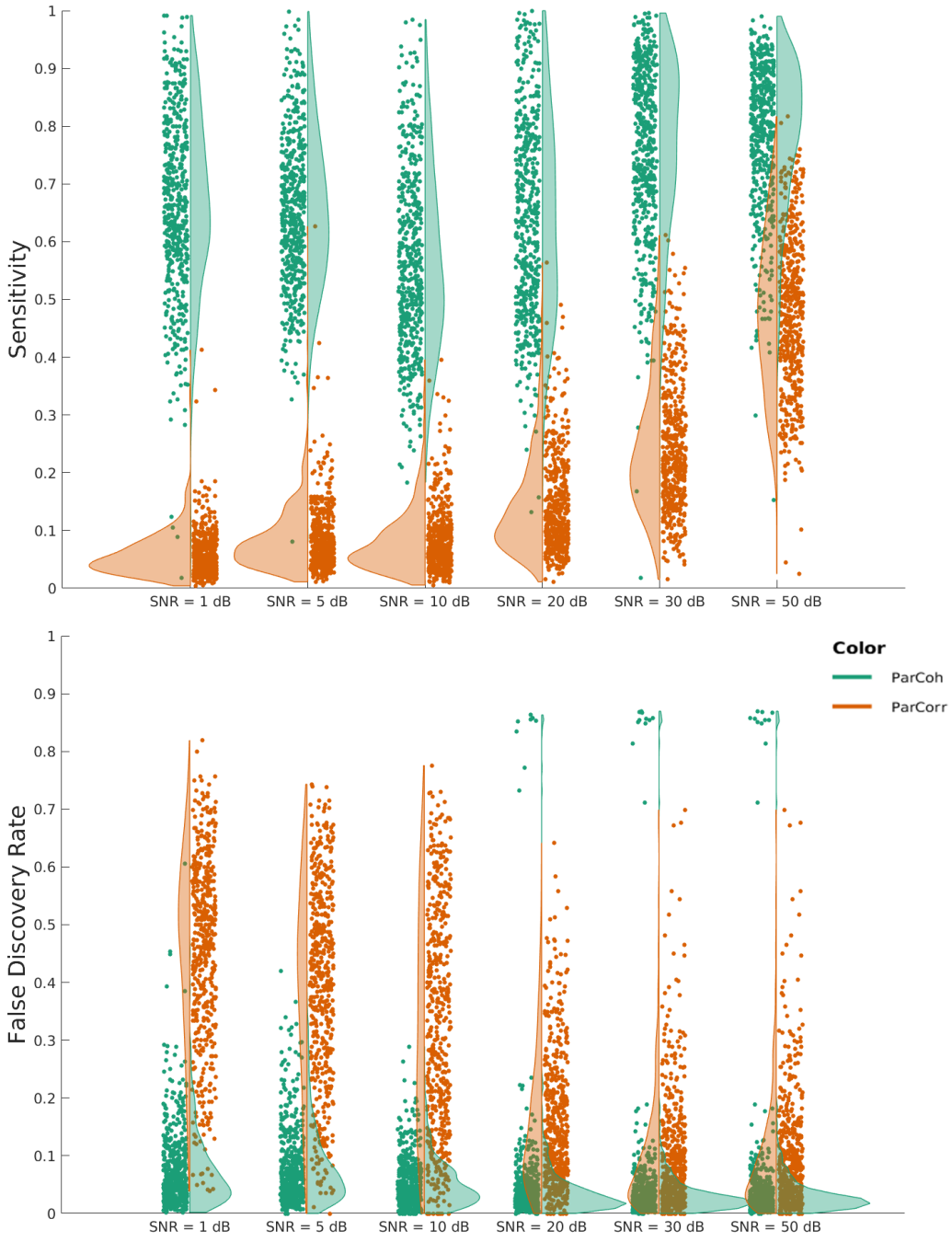

Figure 2.3: Sensitivity and False Discovery Rate in Simulation: We estimated networks using the cGGM and aGGM at different signal to noise ratios. We compared these networks to the binarized SC and examined the sensitivity (upper figure) and false discovery rate (lower figure) between them. cGGM models are more sensitive to the SC across all SNR. cGGM and aGGM have comparable false discovery rates when the SNR rises above 30 dB.

	1 dB		5 dB		10 dB		20 dB		30 dB		50 dB	
	PC	**APC**	**PC**	**APC**	**PC**	**APC**	**PC**	**APC**	**PC**	**APC**	**PC**	**APC**
Sensitivity	0.66	0.06	0.65	0.09	0.56	0.08	0.64	0.14	0.76	0.24	0.78	0.48
FDR	0.08	0.46	0.08	0.4	0.05	0.33	0.05	0.16	0.05	0.1	0.03	0.04
Edge Correlation	0.07	0.03	0.14	0.08	0.25	0.14	0.4	0.29	0.58	0.42	0.83	0.65
Betweenness Centrality	0.31	0.25	0.36	0.29	0.4	0.3	0.48	0.35	0.56	0.38	0.72	0.5
Closeness Centrality	0.34	0.24	0.41	0.3	0.47	0.35	0.56	0.42	0.66	0.48	0.8	0.55
Clustering Coefficient	0.15	0.1	0.17	0.11	0.2	0.12	0.18	0.15	0.17	0.15	0.23	0.13
Degrees	0.32	0.18	0.35	0.22	0.41	0.23	0.49	0.28	0.58	0.32	0.73	0.4
Eigenvector Centrality	0.21	0.21	0.27	0.23	0.32	0.27	0.39	0.31	0.47	0.34	0.57	0.37

Table 2.1: Simulation Results: We show the averages across all simulation iterations for the different metrics computed on both the partial coherence and amplitude partial correlation.

SC. We found that sensitivity, false discovery rate and correlation for both the PC and APC increased with increasing SNR. We report the average sensitivity, FDR and correlation results in Table 1, while the full distributions are shown in Figure 2.3. Sensitivity for the partial coherence increased from 0.66 (1 dB) to 0.78 (50 dB) while for the APC it improved from 0.06 (1 dB) to 0.48 (50 dB). Remarkably even at very low signal to noise ratios, our simulations show that the cGGM can recover the majority of the SC edges.

False discovery rates for the PC decreased from 0.08 (1 dB) to 0.03 (50 dB) and for APC it decreased from 0.46 (1 dB) to 0.04 (50 dB). While network metrics for both PC and APC improve with SNR, the partial coherence remains a consistently better predictor of the original network across all metrics (sensitivity, false discovery rate and correlation) and SNR levels relative to the partial correlation. Remarkably, even at very low SNR very few false edges are estimated by the cGGM.

Finally, we observed that sensitivity shows a non-monotonic relationship to SNR and we believe this to be a trade-off occurring in the optimization of the AGL as at low SNR recovery of accurate weights is difficult so instead the algorithm optimizes edge recovery. However, as SNR increases, weights are more recoverable allowing the SC-QUIC process to optimize for reduced edges but improved accuracy in weights for edges retained. This is clear when we examine the monotonic increase in correlation of edge weights across SNR

(see Table 2.1).

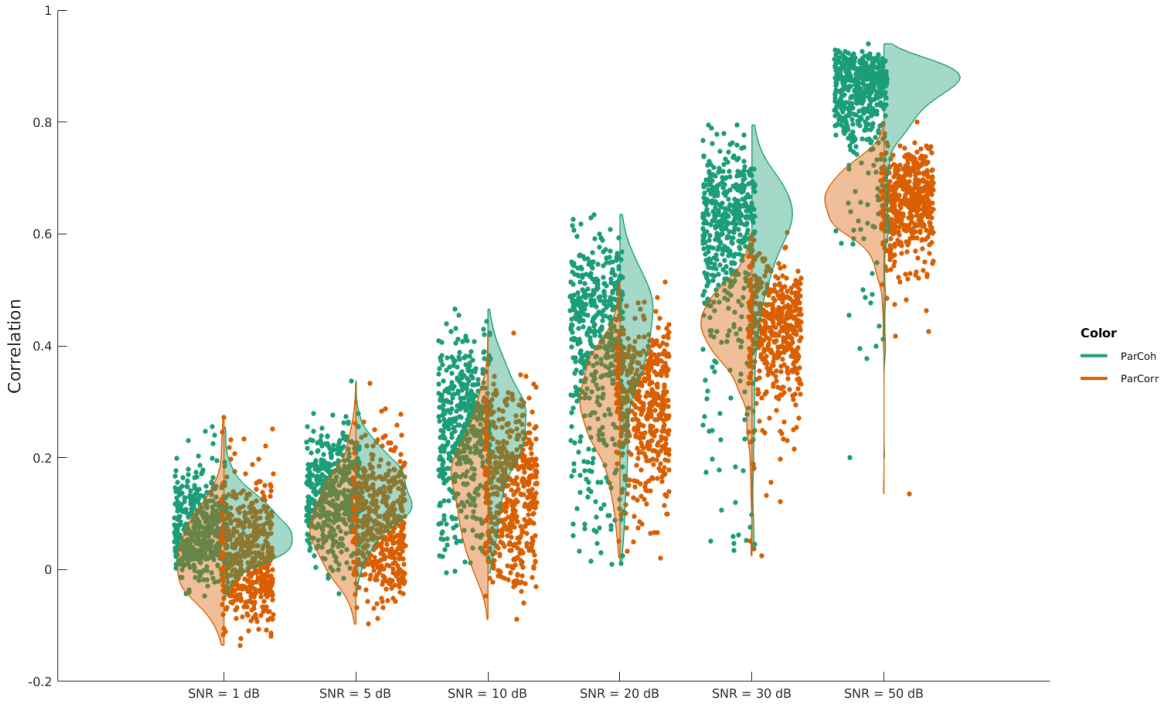

Figure 2.4: Weight Correlation in Simulation: We estimated networks using the cGGM and aGGM at different signal to noise ratios. We compared the partial coherence (cGGM) and partial correlation (aGGM) to the SC and examined the correlation between the set of SC edges and edges estimated. Partial coherence is more correlated to the SC than partial correlation across all SNR. Partial coherence has a correlation greater than 0.5 for almost all reconstructions at an SNR above 30 db while this is true for partial correlation only at 50 dB.

Several Centrality Measures are Accurately Reconstructed

For each reconstructed network in simulation we estimated (weighted) degrees, clustering coefficient, eigenvector centrality, closeness centrality and betweenness centrality. We correlated these measures with the estimates from the original networks (prior to forward modeling and source localization) across all nodes using a Spearman rank correlation. Alongside this, we correlated the reconstructed edge weights with the original edges weights. This was done separately for the cGGM and aGGM networks to see if accuracy in reconstructing graph

theoretic metrics improved on accuracy in reconstructing edge weights.

We found that across all metrics with networks estimated by the cGGM there was monotonic improvement in accuracy with SNR, though the degrees, closeness centrality and betweenness centrality show more rapid improvement with SNR. The full distribution of correlations across all simulations is shown in Figure 2.5. Degrees, closeness centrality and betweenness centrality outperformed the reconstruction reliability (correlation of edge weights) of the partial coherence over all SNR except at $50db$. The range of correlation for degrees was: 0.32 at 1 dB to 0.73 at 50 dB, for closeness centrality it was 0.34 to 0.8 and for betweenness centrality it was: 0.31 at 1 dB to 0.72 at 50 dB. In contrast, we found that the correlation in edge weights followed a range of 0.07 at 1 dB to 0.83 at 50 dB. Eigenvector centrality was comparable or slightly worse at some SNR ($1\ to\ 20\ dB$) to the reliability of the network edge weight reconstruction while clustering coefficient was consistently worse. We show the average correlations for all graph theory metrics and the average correlation in edge weights in Table 2.1.

When examining the same graph theory metrics for the aGGM networks we found similar results. We compared the graph theory metrics calculated from the original partial correlation (prior to forward modeling and source localization) to the reconstructed partial correlation. All graph theory metrics improved with increasing SNR (see Figure 2.6). Closeness centrality and betweenness centrality were more (or equally as) accurate estimators of the original network than partial correlation edge weights across all SNR below 50 dB. Degrees and eigenvector centrality were better only at SNR below 20 dB, while clustering coefficient was a better estimate below 10 dB SNR. Unlike for the partial coherence, we found degrees and eigenvector centrality showed comparable performance when using the partial correlation. The range of correlation (averaged over simulations at each SNR) for degrees was: 0.18 at 1 dB to 0.4 at 50 dB, for closeness centrality it was 0.24 to 0.55 and for betweenness centrality it was: 0.25 at 1 dB to 0.5 at 50 dB. In contrast, we found that the correlation in edge

weights followed a range of 0.03 at 1 dB to 0.65 at 50 dB. Thus, graph theory metrics were more accurately reconstructed than edge weights for both the cGGM and aGGM networks, however, the difference in accuracy is lower at higher SNR.

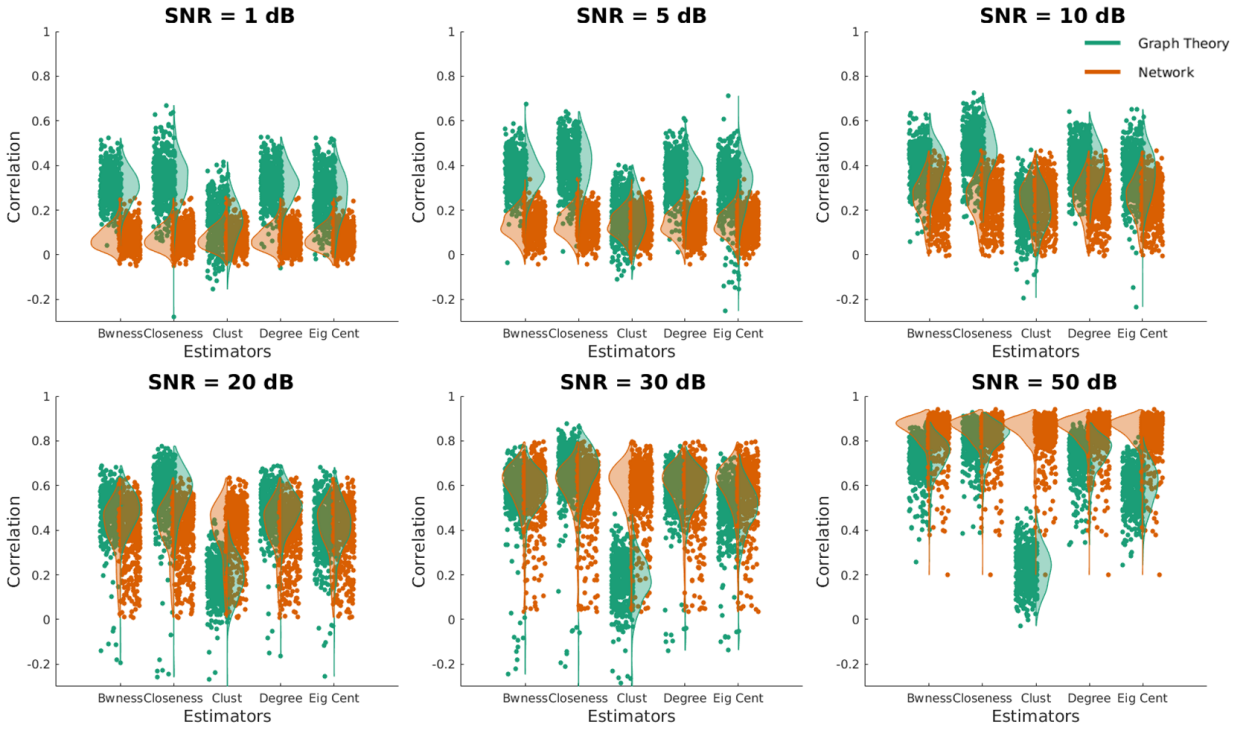

Figure 2.5: Graph Theory and Partial Coherence: We show how well using different graph theoretic metrics does at capturing the structural connectivity characteristics relative to using the reconstructed partial coherence weights. At each SNR, we plot the correlation between graph theory metrics calculated from reconstructed network with the original network across 500 iterations in green. In orange we show the correlation of the weights of reconstructed partial coherence with the original partial coherence. For comparison purposes we show the same set of correlations (of edge weights) alongside all graph theory metrics. We examine the two methods across different SNR and find that at SNR below 50 dB, closeness centrality, betweenness centrality and degrees provide more accurate reconstruction.

2.3.2 MEG Data

We extracted 480 seconds of preprocessed resting state MEG data from 91 subjects from the open source CAMCAN dataset. We source localized this data to the 114 sources of the Lausanne parcellation before using the AGL and our cross validation procedure (see section

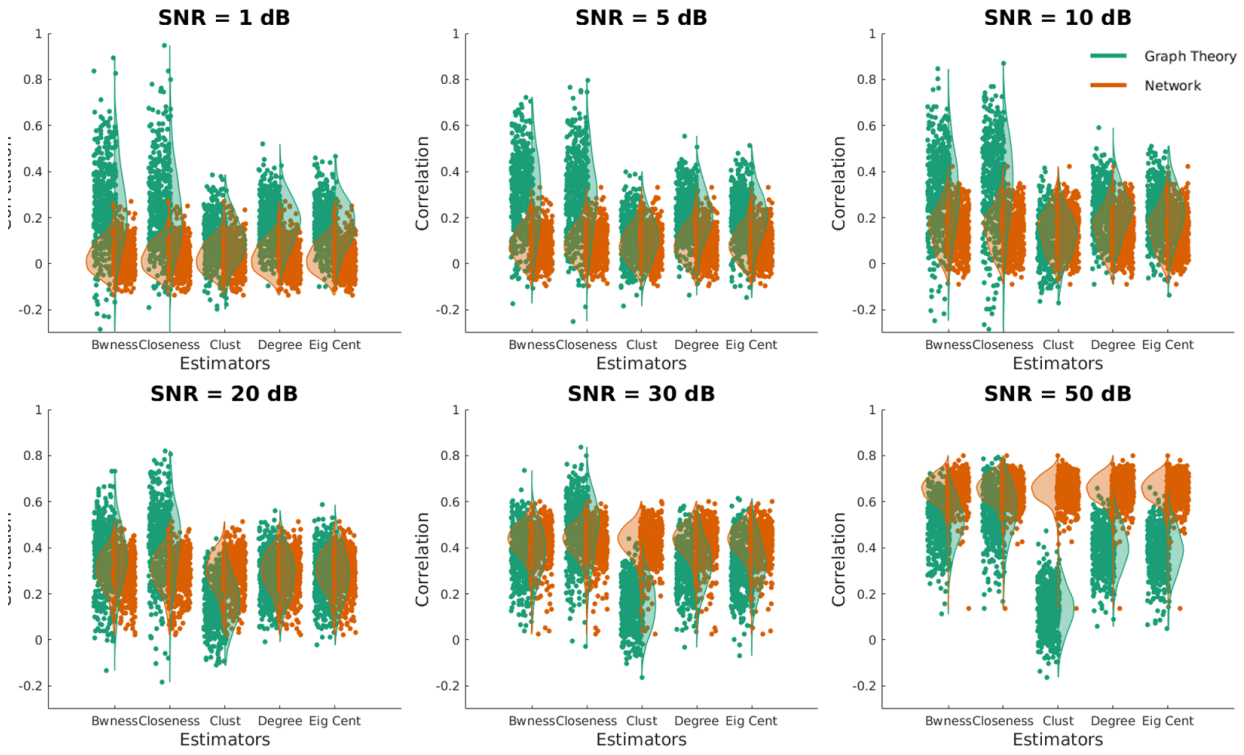

Figure 2.6: Graph Theory and Amplitude Partial Correlation: We show how well different graph theoretic metrics can capture the structural connectivity characteristics relative to using the reconstructed partial correlation weights. At each SNR, we plot the correlation between graph theory metrics calculated from reconstructed network with the original network across 500 iterations in green. In orange we show the correlation of the weights of reconstructed partial correlation with the original partial correlation. For comparison purposes we show the same set of correlations alongside all graph theory metrics. We examine the two methods across different SNR and find that at SNR below 30 dB, closeness centrality, betweenness centrality and degrees provide more accurate reconstruction.

on Cross Validation in Methods) to estimate the most representative cGGM and aGGM models in each of five frequency bands - delta, theta, alpha, beta and gamma bands. From this we estimated the summary statistics of partial coherence (PC) and amplitude partial correlation (APC). We also estimated graph theory metrics we saw as most accurate from out simulation - weighted degrees, closeness centrality and betweenness centrality.

cGGM and aGGM

We estimated partial coherence and amplitude partial correlation for all five frequency bands and estimated the sensitivity and false discovery rate (See Figure 2.7). Sensitivity is informative about the number of edges within the SC that were discovered while FDR tells us how often edges outside the SC were a part of the graphical model. Note that since we use cross validation to determine penalization, sensitivity and FDR are informative about how useful the SC prior is, and by extension, the relevance of the SC to effective connectivity. We found that on average the sensitivity across subjects when networks were estimated with cGGM were: Delta (mean $\pm$ standard deviation) - 0.09 ± 0.14, Theta - 0.15 ± 0.16, Alpha - 0.18 ± 0.19, Beta - 0.42 ± 0.26 and Gamma - 0.75 ± 0.25. This indicates that in the gamma band cGGM, of the 720 edges in the SC, on the average across subjects we identified 540 edges. When using aGGM on the other hand we found sensitivity across bands was: Delta (mean $\pm$ standard deviation) - $.21 \pm .18$, Theta - 0.27 ± 0.22, Alpha - 0.48 ± 0.25, Beta 0.57 ± 0.21, and Gamma - 0.45 ± 0.19. So in the beta band, we were able to, on average, estimate 57% of the SC connections, i.e. 410 edges. Sensitivity in aGGM compared to sensitivity in cGGM was significantly higher across delta, theta, alpha and beta bands (Wilcoxon rank-sum test, $p < 0.001$) but in gamma band it was significantly lower (Wilcoxon rank-sum test, $p < 0.001$). So at lower frequencies ($< 30\ Hz$) partial correlation has higher sensitivity, but at higher frequencies, partial coherence has considerably higher sensitivity. Importantly, the single measure with the highest sensitivity to the SC was the gamma band cGGM which incorporates phase information.

We also examined the false discovery rate (see Figure 2.7) and found that beta and gamma band in cGGM had the lowest FDR. In partial coherence FDR for different bands were: Delta (mean $\pm$ standard deviation) - 0.48 ± 0.26, Theta - 0.37 ± 0.25, Alpha - 0.4 ± 0.27, Beta - 0.29 ± 0.22 and Gamma - 0.28 ± 0.18. This indicates that, if in the gamma band we estimated 1000 edges on average, of those 1000 edges 280 edges were found outside the

SC. While for aGGM, FDR for different bands were: Delta (mean ± standard deviation) - 0.32 ± 0.25, Theta - 0.3 ± 0.19, Alpha - 0.28 ± 0.22, Beta - 0.32 ± 0.19 and Gamma - 0.4 ± 0.22.

Centrality

From our simulations we identified that degree, closeness centrality and betweenness centrality were potentially more accurate than directly examining the recovered weights of reconstructed networks. We estimated the degree, closeness centrality and betweeness centrality for the aGGM in beta band and for the cGGM in gamma band based on the high sensitivity to the SC in these networks. Taking the median across subjects in each measure and for each set of networks (gamma cGGM, beta aGGM) we estimated Spearman rank correlation to the degrees, closeness centrality and betweenness centrality estimated from the original weighted structural connectome. Similar to our analysis for the simulations, we also correlated the median edge weights for the gamma cGGM and the beta aGGM with the weighted structural connectome. Note that since all networks are weighted and we used cross validation to estimate penalization, it is possible for estimates to be divergent between the effective connectivity and the structural connectome. When using the edge weights directly, we found weak but significant correlations between the gamma band edge weights and the structural connectome ($r = 0.08,\ p < 0.05$) and also for the beta band edge weights ($r = 0.08,\ p < 0.05$). In contrast, we saw that the graph theory metrics outperformed edge weight reconstruction. We found that gamma band degrees ($r = 0.29, p < 0.01$) and beta band degrees ($r = 0.33, p < 0.001$) were significantly correlated to the SC degrees. We show the degrees over areas for the gamma, beta and SC in Figure 2.8, where it is clear that, while there is a strong tie to the SC centrality, gamma and beta bands support different patterns of connectivity. Beta band has higher degrees in the precentral gyrus and superior parietal areas while in gamma band, we see greater connectivity in frontal areas. Closeness centrality in gamma ($r = 0.26, p < 0.05$) band was linked to the SC closeness centrality while

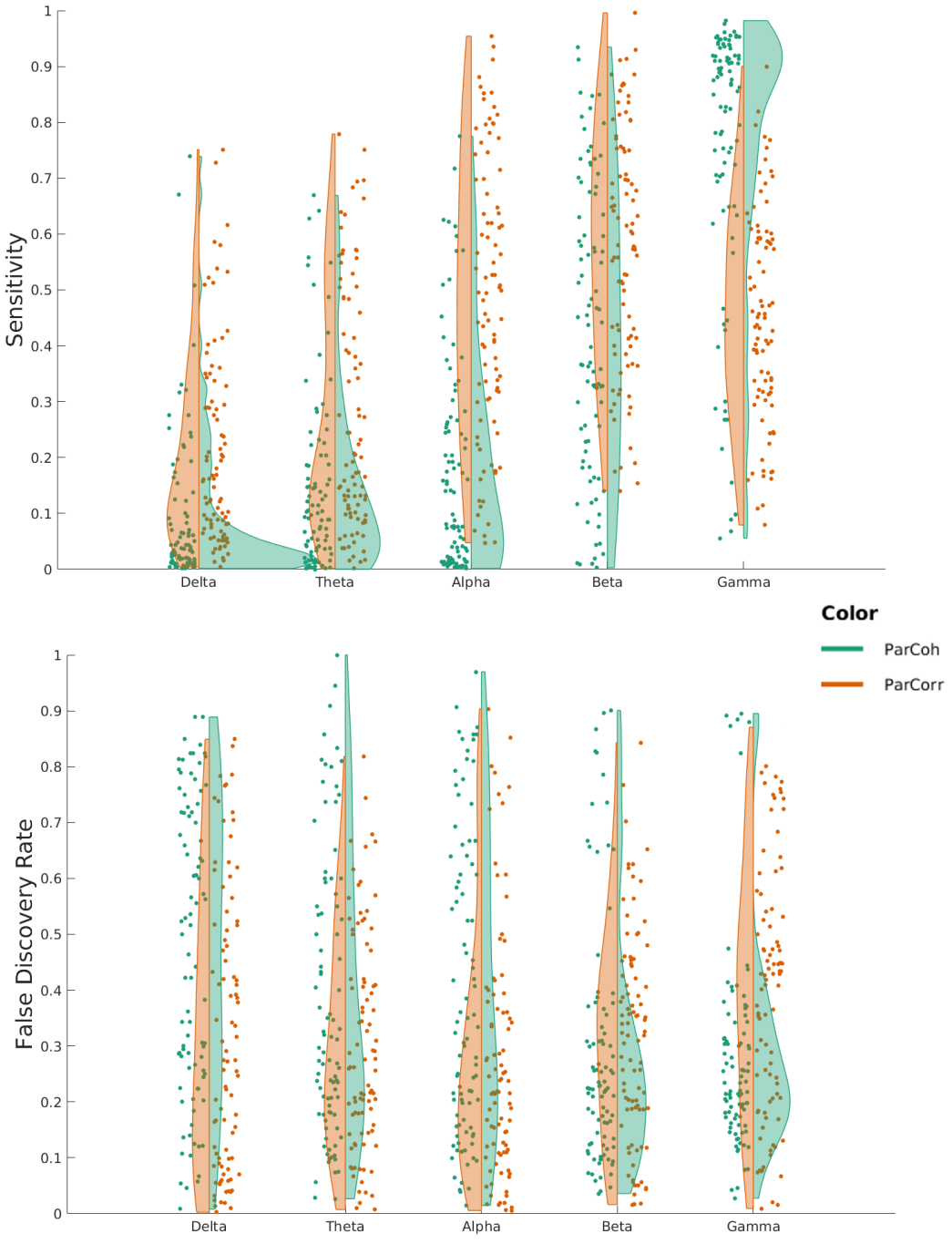

Figure 2.7: Sensitivity and False Discovery Rate in MEG data: We estimated networks using the cGGM and aGGM at different signal to noise ratios. We compared these networks to the binarized SC and examined the sensitivity (upper figure) and false discovery rate (lower figure) between them. cGGM networks are more sensitive to the SC in the beta and gamma bands while aGGM networks are more sensitive to SC in alpha and beta bands. The cGGM network has lower false discovery rates relative to aGGM networks in beta and gamma bands.

beta band only showed a weak relationship ($r = 0.17$). We saw that with SC betweenness centrality, gamma ($r = 0.28, p < 0.01$) and beta band ($r = 0.21, p < 0.05$) betweenness centrality showed strong relationships. As expected from our simulations, the correlations of the graph theoretic metrics outperformed the edge weight reconstructions.

2.4 Discussion

2.4.1 Partial Coherence and Partial Correlation

Using a simulation that generates pseudo-MEG data constrained to one frequency band and forward models this data to the scalp, we examined the ability to reconstruct source level partial coherence and partial correlation based networks. We found that PC based networks recover original network weights betterand have higher sensitivity than APC networks across a range of SNR. When we examined partial coherence and partial correlation in real data, we found gamma band partial coherence to be highly sensitive (75%) to the SC and have low false discovery rates across subjects. Alpha and beta band partial correlation showed significantly higher sensitivity (50%) than their partial coherence counterparts.

Past work on showing the link between electrophysiological networks and structural connectivity have been few but have shown significant relationships between structure and function. Our study extends this line of research. No study to our knowledge, thus far, has examined the relationship of the SC to both estimates of connectivity based on amplitude and phase, and estimates of connectivity based on only amplitude, in humans. We examined the summary statistics of the cross-validated cGGM and aGGM - the partial coherence and partial correlation networks using simulations and showed that at reasonable SNR ($> 10dB$), sensitivity above 50% is possible (effectively learning that field spread and common input effects can be significantly reduced). In data we then identified that, gamma band cGGM

reflects the SC more closely than any other network estimate (75% sensitivity). This result indicates that the coherence has information about the connectome, but primarily in higher frequencies. The slower amplitude modulation reflects information about the SC primarily in lower frequencies, reaching a peak in the beta band (57% sensitivity). On average, across all these measures, false discovery rates was around 30%, indicating that only 30% of edges recovered were outside the SC. There are three consequences of these results (1) The binarized SC provides a valid and useful blueprint from which to estimate the effective connectivity using partial coherence and partial correlation;(2) There are potentially edges that we have failed to include because our SC estimate fails to account for some genuine anatomical connections; (3) Both the coherence based and amplitude based networks reflect the SC to varying degrees, with cGGM reflecting the SC more strongly at higher frequencies (>30 Hz) while aGGM reflects it better at lower frequencies (1-30 Hz).

Why do the cGGM and aGGM models reflect divergent results? One possibility is that at lower frequencies the uncertainty in phase is much greater than the range of possible phases. For example in the theta band, at axon conduction velocities of 10 m/s, for a 20 cm axonal fiber, we can see that the phase difference between the areas connected can only be expected to be in the range of $\pi/10$. In these cases, leakage effects (which only occur at zero lag) might overwhelm the possibility of being able to estimate genuine phase consistency relationships. the amplitude might serve as a better connectivity estimate by providing greater signal to noise ratios. At higher frequencies however, more of the phase spectrum is accessible, possibly improving the ability to estimate genuine phase relationships. Thus, it is possible that the higher sensitivity of gamma band partial coherence relative to the partial correlation could be due to the amplitude correlation being biased by genuine phase relationships in the gamma band [84]. A second possibility is that proposed by the authors in [67]. They use Kuramoto oscillators (at 40 Hz) connected by the structural connectome and tuned to maximize fit to empirical amplitude envelope correlations. They show how frequency modulation due to the presence of temporarily synchronized (phase difference of

0) groups of areas (chimera states) could yield the amplitude envelope modulation on the rate of $0.1Hz$ as reported in the literature. This idea even has some empirical backing [85]. Note that given this mechanistic model, coherence in lower frequencies would be too noisy (when we have too few samples) and thus not a robust estimate for connectivity. A third possibility, using the framework of envelop and phase intrinsic coupling modes[3], is that the envelope intrinsic coupling modes (the networks expressed when using the amplitude) is more tightly coupled to the structural connectome while phase based relationships (coherence) vary more so that phase relationships can be used to manage information transfer during tasks (communication through coherence [2]). However, this framework does not explain why amplitude correlation relationships between areas in lower and higher frequencies should differ. Yet another possibility is that lower frequencies simply are not expressed well in the way we have parcelled the brain,and in fact, it may be a good idea to build parcellations separately for lower and higher frequencies given prior knowledge that oscillatory activity in lower frequencies tends to recruit larger groups of neurons [1] - though this may not relevant at the M/EEG spatial resolutions.

2.4.2 Using Graph Theory

Using graph theoretic metrics to summarize networks showed reduced error when using degree, closeness centrality and betweenness centrality over the majority of SNR levels for both PC and APC networks. However, in contrast, clustering coefficient and eigenvector centrality showed increased error in reconstructed networks relative to other graph theoretic metrics. We estimated degree, CC and BC for the gamma band MEG-PC, and the alpha and beta band MEG-APC. We found significant correlations between all centrality estimates with the SC estimates, however, there was considerable unexplained variance indicating the hubs in data do not exactly map onto the hubs from the SC. In summary, these results suggest that using graph theory to collapse connectivity structures of nodes is useful and

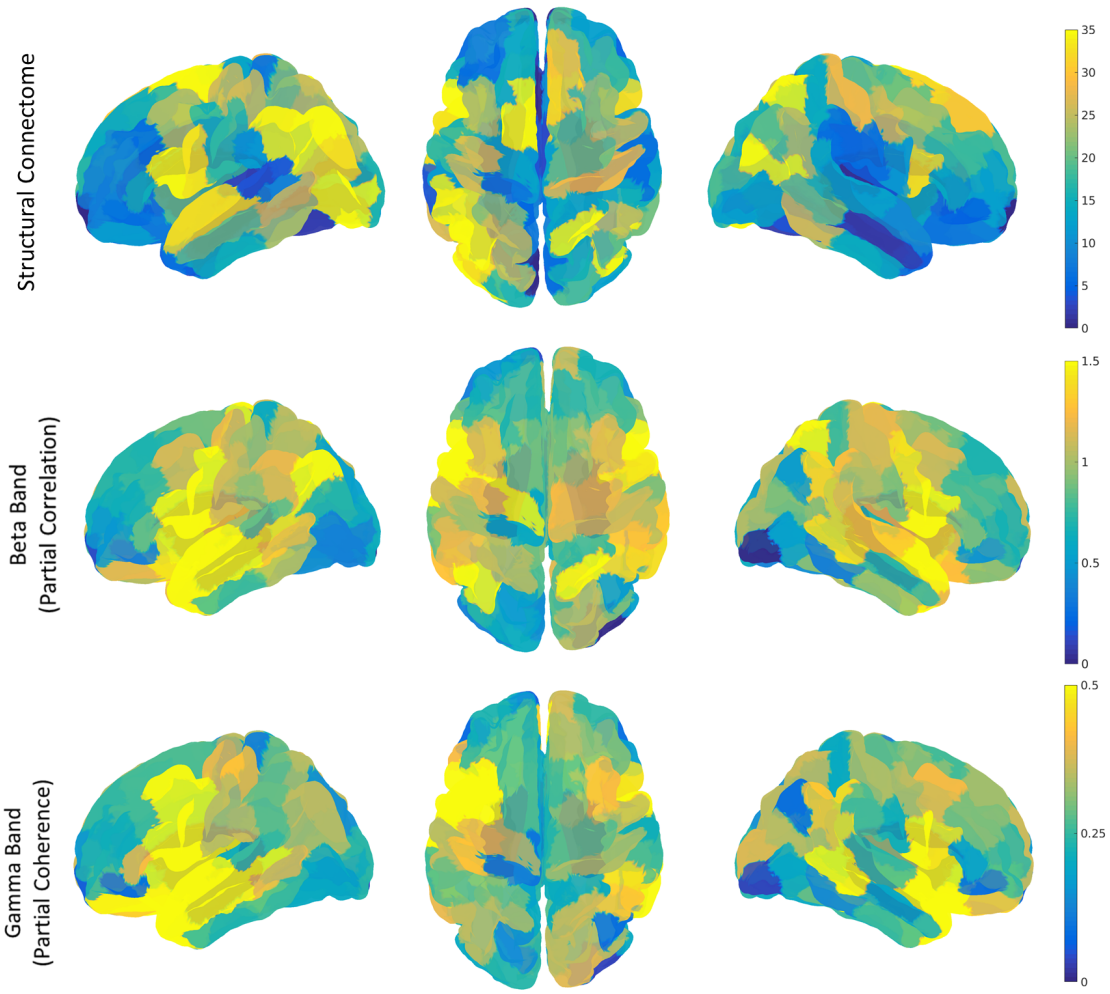

Figure 2.8: Degrees Across Connectomes: We show degrees across different areas in the structural connectome. Similarly we show median degrees across subjects in the beta band when using partial correlation, and in gamma band when using partial coherence.

robust but only for a subset of metrics.

Using graph theoretic tools to summarize networks has been suggested and applied in highly specific ways in the literature, such as by examining the minimum spanning tree of a network [86]. The minimum spanning tree (MST) represents the skeletal backbone of the network and the underlying interpretation is that using this approach improves robustness of the inference on the networks. A recent empirical study examined MST properties for networks constructed at the scalp and at source level. They found that for most network characteristics (as estimated using the MST) there was weak correlation between scalp and source level.

Other simulation work [87] has shown that identifying the generative process that created a network is difficult to impossible when analyzing scalp based networks. For these reasons estimation of graph theoretic metrics are better done at source level given the theoretical and empirical justifications of using source localized data. We expanded on these questions by examining which GT tools can be estimated well at source level after field spread and volume conduction. Further, we examined whether the accuracy of GT tools improved on directly using the weight structure of the networks. We have shown that we can in fact identify hub nodes using degree or closeness centrality or betweenness and expect those estimates to be closer to the underlying structural connectome relative to using the weights of the network. However other GT tools such as the clustering coefficient and eigenvector centrality were poor estimates. Clustering coefficient has been shown to be biased (underestimated) when using partial correlation estimates [88] and this may be part of the reason it is a poor estimate.

Our results suggested that maximum accuracy with respect to reconstructing networks that aligned with the structural connectome, when using weighted networks, was found using the degrees, closeness centrality and betweenness centrality. We estimated these measures for the networks that the highest sensitivity to the SC from the empirical MEG networks-gamma band partial coherence, alpha and beta band partial correlation. We found that for these networks when we collapsed the three centrality estimates across subjects, there was a significant correlation to the centrality estimated from the weighted SC. This result indicates that graph theory metrics provide useful information about the network properties in different bands.

2.4.3 Other Methods to Reduce Leakage Effects

In the literature, a common method to reduce the influence of leakage effects when estimating amplitude envelope based connectivity is to orthogonalize the amplitude envelopes [19].

When estimating phase based connectivity, it is common to use the imaginary coherence[89]. Both of these approaches operate on the (valid) assumption that there is field spread effects only at zero lag under pseudo-static assumptions. However, three notable problems with imaginary coherence and orthogonalized AEC are that (1) It may be too conservative an estimate and chooses to lose considerable information about connectivity in the data; (2) It is susceptible to spurious ghost connections where long range connections exist at a delay but only due to local leakage effects (a particular instance of common input effects) [84]and (3) Common input driven connectivity. Thus, we believe that using partial coherence or partial correlation estimated using cGGM or aGGM with the SC prior is a more robust connectivity estimate when making inference on connectivity.

2.4.4 Limitations

Several limitations exist in our work. In our simulation to simplify the analysis we assumed a generative model where different parts of the brain show random oscillatory behavior linked by the structural connectome. This could be represented using a zero mean complex multivariate normal with a circularly symmetric precision. More detailed mean field models of neural activity may be more phenomenologically accurate, however, past work suggests there is limited gain in using them when explaining empirical data [51, 54]. Another issue is that we assumed a common generative model for both the amplitude and the coherence based networks. Other work suggests that potentially there may be independent mechanisms at play in generating these two modes of neuronal coupling [3, 67, 90].

Source localization can be formulated in several ways based on prior assumptions. While we used a weighted L2 norm inverse, beamformer reconstruction approaches are also quite common. More detailed bayesian techniques potentially account for priors more explicitly and afford better source reconstruction [91]. Examining these approaches was beyond our

scope for the purposes of our simulation and data analysis. Additionally we chose to limit our analysis to a case where there are 114 sources, a future extension to this work might examine cases with more (fewer) sources.

We ignore for our purposes subcortical source activity and connectivity. This may lead to large variation in the estimated results, however, estimation of subcortical activity in MEG while possible is difficult without explicit prior knowledge [92]. An important note is that the influence of subcortical-cortical connectivity could bias graphical model based connectivity approaches.

Coming to the application of graph theory, we have limited our analysis to common metrics. However, there is a wide range of graph theoretic tools [82] whose use is justified as a function of the question being asked. Our simulation approach could well be used to test whether other metrics can be well estimated when working with MEG data.

2.4.5 Conclusion

In summary, we used simulations and data to determine the extent to which structural connectivity instantiates effective connectivity. Using real and complex valued graphical models we showed that partial coherence is a high sensitivity, low false discovery rate estimate of the SC in simulations. Further, we saw that graph theory can improve accuracy in reconstructing structural connectome characteristics. In data, we found that cGGM models of the gamma band showed the highest sensitivity. Across cGGM and aGGM models of data we found that the false discovery rate hovered around 30% suggesting that our SC may be incomplete, or there are unaccounted for influences on the effective connectivity. Finally, we saw that our results using graph theory in simulations were borne out in the data where graph theoretic metrics of gamma band partial coherence and beta band partial correlation showed a stronger correlation to the SC than the edge weight correlation.

Chapter 3

Influence of damage to the Structural Connectome on Functional and Effective Connectivity in resting state fMRI

3.1 Introduction

A sub-field of systems neuroscience focuses on examining the structure of spontaneous neural activity when subjects are at rest. A large body of evidence shows that there exist significant statistical dependencies, labeled functional connectivity, between brain areas during rest (e.g.,[17, 93]) in the blood oxygen level dependent (BOLD) fMRI signal. In the most direct analyses, functional connectivity is measured by linear correlation of the BOLD signal averaged over voxels in two regions of interests (ROI). Resting state networks, defined by groups of brain areas with significant functional connectivity [17, 94, 95], have been shown

to predict task performance and discriminate clinical states (for a detailed review see [18]).

One obvious question is "what mechanism gives rise to resting state functional connectivity?". One simple explanation is that axons of neurons in one area of the brain make a synapse onto neurons in another area facilitating the correlation in neural activity recorded at the two locations. In practice, establishing this anatomical basis for fMRI functional connectivity has proved immensely challenging. In the past two decades new brain imaging protocols (Diffusion Weighted Imaging) and analysis methods (tractography) have been developed that allow for non-invasive estimation of axonal fiber tracts of the human brain. The set of all fiber tracts is referred to as the structural connectome [6].

A large number of studies have investigated relationship between the diffusion imaging based estimate of the structural connectome and fMRI functional connectivity ([48–52, 96, 97]). Pairs of brain areas without a structural connection have significantly weaker fMRI functional connectivity [48], supporting a direct relationship between structural and functional connectivity. However, across studies, the group average structural connectome weights explains between 10 - 65 % ([53]) of the group averaged fMRI functional connectivity across different studies. The wide range of these results suggests that the structural connectome wiring doesn't fully determine functional connectivity, which in any case must vary across brain states. Moreover, structural connectome estimates are susceptible to error due to crossing fibres and difficulty in following fibre orientation showing both false positives and false negatives. ([98]). In addition, estimates of fMRI functional connectivity are strongly influenced by the parcellation applied to carve up the brain into different regions of interest (ROIs) [99] and the method used to estimate functional connectivity [100]. Finally, across different datasets ([48, 101, 102]), structural to functional connectivity association doesn't depend on having an individual specific estimate of the structural connectome for the subject whose functional connectivity is being estimated. Individual differences in structural connectivity are less pronounced than the individual difference in functional connectivity [101] in

fMRI as the structural connectivity examined ROI by ROI shows globally lower variability relative to the functional connectivity variance.

This limited variability of the structural connectome suggests that quantifying the contribution of the structural connectivity to functional connectivity is challenging when working with data from healthy brains. In this study, we set out to examine the relationship between structural connectivity and fMRI functional connectivity using data from stroke patients. Patients who suffer stroke have lesions that damage their brain anatomy, most commonly the white-matter tracts. Each stroke patient has unique lesions, indicating considerable individual differences in damage to the structural connectome. We leverage this resulting heterogeneity in structural connections to investigate the relationship between structural connections and fMRI functional connectivity. In our work we examine the edge by edge relationships of the structural connectivity to fMRI functional connectivity across patients with lesions due stroke, to identify how structural damage modulates functional connectivity, providing a strong test of the relationship between structural connectivity and fMRI functional connectivity.

Current theories suggest that functional connectivity is driven both by mono-synaptic and poly-synaptic connections through the structural connectome[49, 51, 58, 103, 104]. These theories provide potential explanations for fMRI functional connectivity estimated using correlation. Correlation by definition permits poly-synaptic pathways to influence fMRI functional connectivity - if C is correlated to A and B through structural connections, A and B are also correlated. One polysynaptic generative mechanism for the fMRI functional connectivity is Gaussian noise becoming correlated due to structural connections. Under this model, partial correlations are normalized precision estimates that reflect conditional dependence. A strong partial correlation implies that the relationship between two areas exists independent of their relationship to other potentially intermediary areas, which potentially directly reflect the wiring of the brain, and may be more closely related to the structural

connectome. We introduce a a novel model-based estimate of fMRI effective connectivity in terms of the partial correlation that explicitly models FMRI functional connectivity using the structural connectome.

This study offered an opportunity to examine what type of communication pattern could explain the generation of functional connectivity by the spread of activity over structural connections. In a monosynaptic model that only considers direct connections, functional connectivity would be expected to simply reflect the weights of the structural connectome and damage to the strongest structural connections would have the strongest effects of functional connectivity. We anticipate this direct relationship could only be found for fMRI effective connectivity, which is based on partial correlations which enforces direct connections. Functional connectivity estimates based on correlation include both mono-synaptic and polysnaptic connections. One way that neural activity may spread across the SC is through diffusion. Under diffusion, functional connectivity is determined by how often random walks from A or B end up at the other area. If diffusion is the critical model, we expect that damage to connections with higher rates of diffusion would have the strongest effects on functional connectivity. The alternative is that activity always passes through shortest path between A and B and not all possible paths. If the spread of activity is constrained to shortest paths, we expect that damage to connections between nodes which are relevant to more of the shortest paths in the network would have the strongest effects on functional connectivity. We test whether diffusion or shortest path routing are active over the SC by examining which provides an estimate of functional connectivity that better predicts the edges where structural connectome damage is reflected in functional or effective connectivity.

In this study we examined the relationship between structural connectivity and functional connectivity in 20 stroke patients. We estimate the structural connectome (SC) for each patient using virtual tractography [105, 106] across the pairs of 114 cortical ROIs from the Lausanne parcellation[66]). We measured fMRI-functional connectivity (fMRI-FC) using

conventional linear correlation between ROI-averaged signals as well as a finely resolved (voxel-level) estimate of fMRI functional connectivity which we refer to as streamline functional connectivity (fMRI-sFC). We also used the Adaptive Graphical Lasso to develop a SC-based model of fMRI effective connectivity (fMRI-EC) to estimate direct connections, and remove polysynaptic (indirect) functional connections. We expected that damage to the SC would more clearly influence the model based fMRI-EC than fMRI-FC due to the effects of polysynaptic connections. Our results support the effectiveness of fMRI-EC over fMRI-FC in identifying damage to the structural connectome. However, the results also indicate that even more information about the SC is available in functional connectivity estimates at the voxel level in our measure of streamline functional connectivity (fMRI-sFC).

3.2 Methods

3.2.1 Patient Details

Subjects were recruited from the UC, Irvine Medical Center inpatient rehabilitation facility (N=20) having suffered stroke between 3 to 26 days prior to being enrolled in the study. The mean age of subjects was 57.45 $\pm$ 12.05 years (range 27-79), and their Fugl-Meyer score ranged from 10 to 65 (with an expected score of 66 for someone without motor difficulties). Of these 20 patients, 7 patients were found to have lesions that damage both gray and white matter, while 13 had lesions that primarily impact white matter.

3.2.2 MRI

Neuroimaging was acquired on a 3.0 T Philips Achieva (Best, the Netherlands) scanner. Anatomical imaging included a high-resolution T1-weighted scan that utilized a three-dimensional

magnetization-prepared rapid gradient echo sequence (TR=8.1 ms, TE=3.7 ms, 150 slices) and T2-weighted FLAIR scan (TR= 9,000 ms, TE=120 ms, 33 slices). Following preprocessing, lesions were flipped to the left side so that the left hemisphere was the ipsilesional hemisphere for all subjects.

3.2.3 fMRI

Individuals (N=20) with subacute stroke completed a resting-state fMRI scan: TR=2,000 ms, TE= 30 ms, 180 volumes, voxel size= 3.38x3.38x3 mm^3. Subjects were instructed to remain still and keep eyes open to avoid falling asleep. We discarded the initial 8 fMRI volumes. Structural and fMRI data were preprocessed using the CONN toolbox [107]. Preprocessing steps included functional slice-time correction, functional realignment (six rigid-body motion parameters), structural segmentation and normalization to MNI space, functional normalization to MNI space and co-registration to structural volumes, functional outlier detection using the artifact removal toolbox (ART), and functional smoothing using a $6mm^3$ Gaussian kernel. Functional MRI data also underwent denoising procedures to remove unwanted motion, physiological effects, artifacts, and the global signal from the BOLD signal. These additional procedures included: bandpass filtering (0.008-0.09 Hz) and regression.

3.2.4 Virtual Tractography

We used streamlines generated with deterministic tractography by Yeh et. al. [68] using the HCP842 dataset [8] transformed to the MNI152 template brain pulled from FSL. We transformed the Lausanne parcellation [66] of 114 cortical and 15 subcortical ROIs to the MNI152 template brain and generated a volumetric representation for each ROI using the *easy_lausanne* toolbox (Cieslak, 2015). The MNI coordinates of the areas are listed in Appendix A1. Each streamline was approximated by a single 100-point cubic spline using

code adapted from the along-tract-stats toolbox [69].

We drew lesion masks on T1-weighted MRIs, informed by the corresponding T2 FLAIR images. For one subject unable to complete an MRI scan, we drew the lesion mask on their corresponding CT scan. Infarct masks were binarized and spatially transformed to MNI space. We intersected these lesion masks with the predefined streamlines for the undamaged SC. Right hemisphere lesions were flipped to the left hemisphere. Using the reduced set of streamlines, we define individual structural connectomes. We graphically show this process in Figure 4.1. By identifying the streamlines which ended in a pair of ROIs we were able to create the structural connectome for the Lausanne parcellation. Any edge $W_{ij}$was defined as the sum over the streamlines biased by the length of the streamline. So for ROIs i and j connected by streamlines s of length l:

$$W_{ij} = \sum_{s_{ij}} \frac{1}{l_{ij}} \tag{3.1}$$

We weight the streamlines by length to reduce the bias of tractography algorithms towards longer streamlines [70]. From this process we built the $129 * 129$ weighted structural connectome with 1132 edges. We reduced this matrix to $114 * 114$ with 720 edges after removing all the subcortical structures and limiting interhemispheric connections to known homologous white-matter tracts. This latter step helped remove potentially noisy estimates of connections where streamlines intersected and passed outside the cortical surface before reaching the terminal point in a brain region. The resulting model of structural connectivity shown in Figure 1 is referred to as the structural connectome (SC). This model is incomplete in that it does not include thalamocortical projections, and thus there may be functional connectivity that is a result of structural connections outside of this SC. Our estimation procedure described in the next section allows for such connections.

There was considerable variability in the set of connections that were damaged by the lesions

across 20 patients. We found through visual examination of the distribution of damage to edges that the distribution was skewed or showed bimodal behavior. We decided to stratify damage based on this observation. Each edge for each patient was designated as either high or low damage. High damage indicated that, for that edge, connection strength was less than the midpoint of the range of connection strengths seen for that edge. We show how many edges have high damage across patients in Figure 4.1. We found that over half of the connections showed high damage in few to no patients. When categorizing the damage in this way, we found that 341 edges showed high damage across at least 3 patients. Majority of the edges modeled connected frontal (111), parietal (72) and motor (48) areas in the damaged hemisphere to the rest of the brain. We show the edges modeled by area in Figures 3.5 and 3.6.

3.2.5 Measures of fMRI Functional Connectivity

We use the pre-processed time series from fMRI averaged over ROIs from the Lausanne parcellation and estimate the covariance in the time domain. We labeled this ROI-averaged functional connectivity fMRI-FC. In addition we estimated a model based effective connectivity using the adaptive graphical lasso that we labeled as fMRI-EC. Finally, as described below we also examine a finely-resolved (voxel-level) estimate of the functional connectivity biased by the streamlines that we label as streamline functional connectivity or fMRI-sFC.

3.2.6 Adaptive Graphical Lasso to Estimate fMRI Effective Connectivity

FMRI-FC was estimated using the linear correlation between ROIs. By default, it includes indirect connections representing connections formed over poly-synaptic paths and through

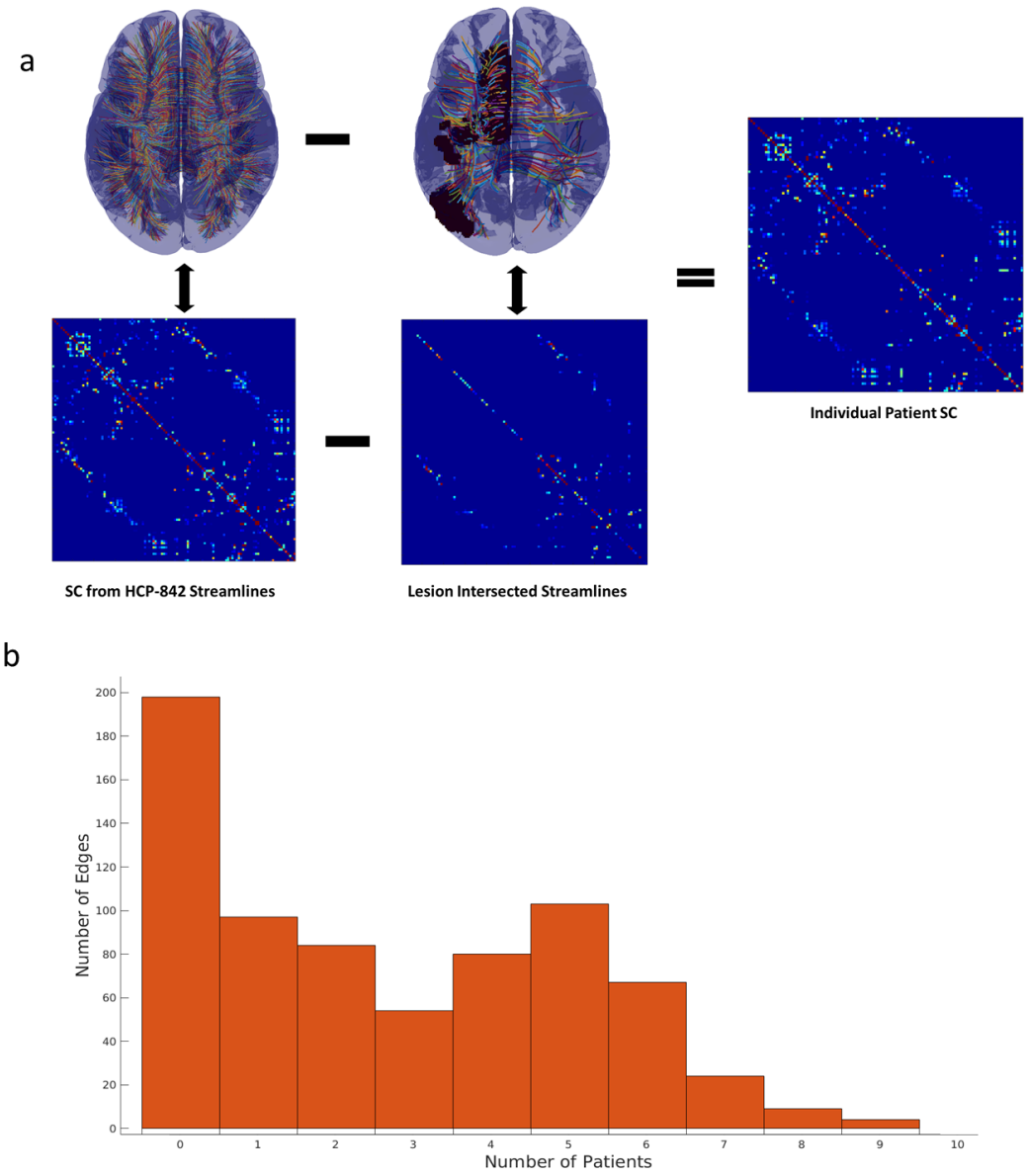

Figure 3.1: Virtual Tractography - in (a) we show the pipeline for virtual tractography. We remove from the set of streamlines that represent the undamaged structural connectome (top left) the streamlines intersecting any particular patient's lesion(s), as shown in the top middle figure. Using the reduced set of streamlines we apply the Lausanne parcellation to get the final structural connectome for that patient (shown on the right). (b)Edges Showing High Damage Across Patients - We show the number of edges where patients show high damage. We found that for over 50% of edges there are few (1 or 2) to no patients showing the presence of high damage. In our analysis we used all edges where 3 or more patients had high damage (341).

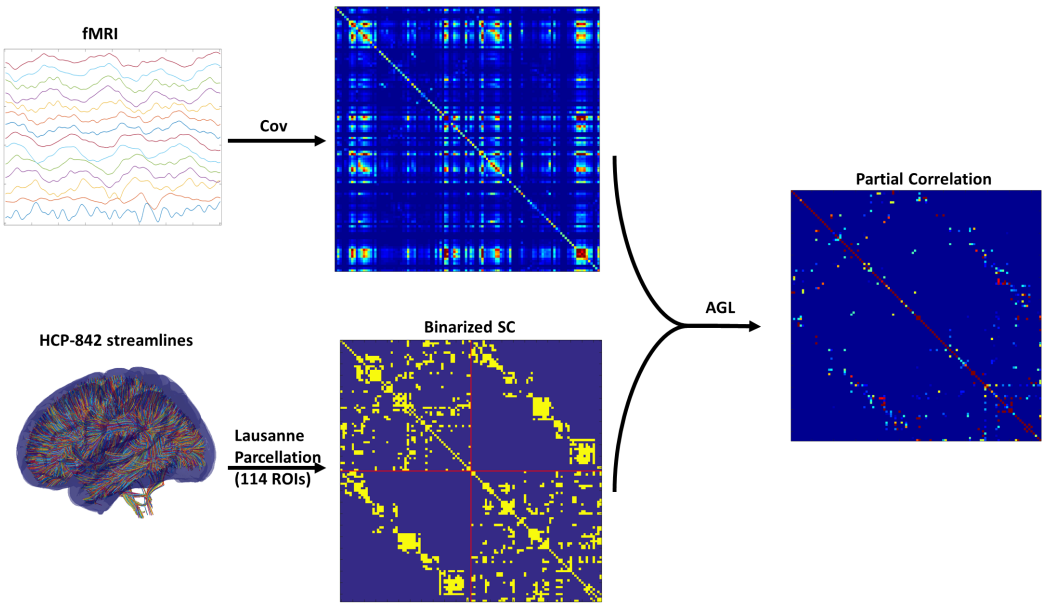

Figure 3.2: Using the Adaptive Graphical Lassso - This was the general processing pipeline for applying the AGL to fMRI covariance from patients. The binarized undamaged SC is used to bias the penalization used when optimizing under the AGL to estimate the precision(which after normalization gives us the partial correlation).

common inputs. Instead by using graphical models (effective connectivity) to estimate the precision, we can examine direct connections. Partial correlation is estimated using the normalized inverse (precision) of the covariance of the fMRI time series. The estimate of precision from direct inversion tends to be noisy due to an ill-conditioned covariance matrix. To improve the robustness of the precision, it is usually estimated using the graphical model estimated from the graphical lasso. The graphical lasso [32] is a method that has been applied in multiple fields in the past decade, from genomics [75], to fMRI functional connectivity ([76], [37]) and climate models [77]. In order to apply the lasso, we use the penalized likelihood function as follows ([33]) to estimate the precision (where Θ is the covariance):

$$\hat{\Phi} = argmin_{\Phi \succ 0} \left(-log(det\Phi) + tr(\Theta\Phi) + \lambda \sum_{j<k} |\Phi_{jk}| \right) \tag{3.2}$$

Our purpose was to make use of the lasso while taking advantage of our prior knowledge of the structural connectome (SC) which are the likely locations of nonzero precision values. We made use of the lasso optimization from QUIC ([78]) using a matrix penalty term (this process is also called the adaptive lasso - [79]) determined by the SC with edges W (and $\lambda_1 = \lambda_2$):

$$\hat{\mathbf{\Phi}} = argmin_{\mathbf{\Phi} \succ 0} \tag{3.3}$$

$$\left(-log(det\mathbf{\Phi}) + tr(\mathbf{\Theta\Phi}) + \lambda_1 * \sum_{j<k; W_{jk} \in SC} |\mathbf{\Phi}_{jk}| + \lambda_2 * \sum_{j<k; \boldsymbol{W}_{jk} \notin SC} |\mathbf{\Phi}_{jk}| \right) \tag{3.4}$$

Past work along these lines [43] has used the SC weights directly to determine the penalization weighting, which imposes more structure that appropriate. We expect that the SC weights will potentially constrain connectivity strengths. However, we do not expect the SC strengths

to map directly onto the effective connectivity strengths due to individual differences, and variations within individuals accross brain states. By using a template, we are assuming a common SC across participants, so the expected weight may differ. Further, the SC can be expected to be used differently across frequency bands yielding different effective connection weights. For this reason we use the binarized SC to determine the penalization structure. We estimated the penalization values λ_1 and λ_2 using cross validation as described in the next section.

To run both lasso optimizations we used QUIC [78]. By using the adaptive lasso, we leveraged the information in the SC as a prior for our estimate of fMRI effective connectivity which we summarize as partial correlation. We heavily penalized the non-existent edges in the SC (λ_2), while being more gentle on those that do exist (λ_1). The penalization parameters λ_1 and λ_2 in the graphical lasso determine the set of precision values retained. The output of the lasso when optimizing Equation 4.12 or Equation 3.3 is the gaussian graphical model (GGM). We derive our graph G with vertices $V = 1, 2, ...C$ and edges $W_{est} = G_{ij} = 1, i, j \in V$ from the GGM based on the non-zero values. The precision matrix $\hat{\Theta}^{-1}$ is estimated under the Gaussian likelihood for the set of edges W_{est} defined by the graphical model using the function $ggmFitHtf$ (PMTK3 toolbox [80]) which optimizes (unpenalized Gaussian log-likelihood):

$$\tilde{\mathbf{\Phi}} = argmin_{\Phi \succ 0; |\Phi|>0=G} - (log(det\Phi) + tr((\Theta + \delta * I)\Phi)) \tag{3.5}$$

Since $\mathbf{\Theta}$ (covariance) is usually rank deficient, we add a small value (δ) along the diagonal to make it full rank. We define *delta* as 0.001 times the maximum value along the upper triangle of the covariance.

Cross-validation to test the Structural Connectome model of Effective Connectivity

The adaptive graphical lasso allows us to impose the structural connectome onto the functional data potentially allowing for more robust reconstructions of the precision. We tested whether the adaptive graphical lasso produced estimates of the precision that show reduced error relative to applying the graphical lasso. We split the fMRI data from patients into two halves. Using graphical lasso and adaptive graphical lasso we estimated the precision $\tilde{\Phi}_1$ on one half of the data and estimated the deviance when using this precision as the inverse for the covariance of the other half Θ_2 of the data (and vice versa). Deviance was estimated as:

$$Dev = .5(-log(det\tilde{\Phi}_1) + tr(\Theta_2\tilde{\Phi}_1) - log(det\tilde{\Phi}_2) + tr(\Theta_1\tilde{\Phi}_2)) \tag{3.6}$$

We tested whether the adaptive graphical lasso lead to improved estimation of the fMRI-EC relative to the graphical lasso. We applied the process of cross-validation over the same range of penalization for λ_1 in the adaptive graphical lasso (3.3) and for λ in the graphical lasso (Equation 4.12). For the adaptive graphical lasso (Equation 3.3) we maintained λ_2 (the penalization for non-SC edges) constant at 0.2. The results from this analysis are shown in Figure 3.3. We found that with the graphical lasso a sparser model (fewer connections) is always better (indicated by the decreasing cross-validated deviance). However, when using the adaptive graphical lasso, we find there is an optimal set of SC edges while minimizing non-SC edges which minimizes the deviance. Further the adaptive graphical lasso leads to consistently lower cross-validated deviance relative to using the graphical lasso. Based on the minimum deviance from cross-validation, we estimated fMRI-EC using the adaptive graphical lasso with the penalization value of 0.125 inside the SC (i.e. λ_1 from Equation 3.3) and 0.2 (λ_2 from Equation 3.3) outside the SC.

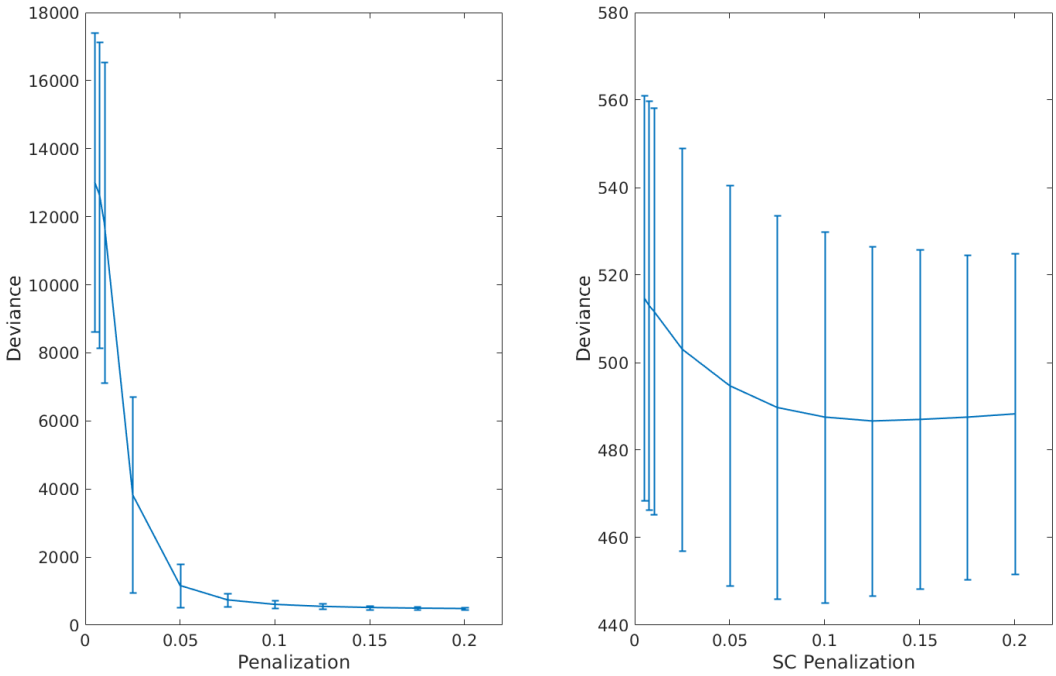

Figure 3.3: GL vs AGL - We show performance (cross-validated deviance) across penalization for the graphical lasso (on the left) and adaptive graphical lasso (right figure). The error bars represent the standard deviation of the deviance across patients. We found that for all but very high penalization the AGL outperformed the GL. Further, the AGL shows minimal cross-validated deviance for an optimal set of SC edges (at an SC penalization of0.125) while the graphical lasso shows minimum deviance only for very sparse models.

Partial Correlation

We estimate partial correlation as the summary statistic for the Gaussian Graphical Model. We estimate the partial correlation (for any two areas x and y and estimated precision $\tilde{\mathbf{\Phi}}$):

$$PC_{xy} = \left| \frac{\Phi_{xy}}{\sqrt{\Phi_{xx} * \Phi_{yy}}} \right| \tag{3.7}$$

We use PC as our estimate of the effective connectivity and refer to it as the fMRI-EC. We use this partial correlation similarly to the correlation matrix when estimating the impact of damage to the SC edges. This is discussed in section 4.2.3.

3.2.7 Modeling Impact of SC damage

We transformed the correlation and partial correlation across subjects by taking their absolute value and applying Fisher r-to-z transforms. For the partial correlation we added a small value (10^{-4}) to make all values non-zero (gamma distribution is undefined for 0). Let C_{ijk} represent the transformed correlation between ROIs i and j for subject k and P_{ijk} the transformed partial correlation. We treat the C_{ijk} and P_{ijk} as Gamma distributed variables because the values are positively valued and tend to be skewed towards the positive axis of the real line. Using this notation, $C_{ij:}$ and $P_{ik:}$ represent the response vectors for a gamma generalized linear models using a log link function. We used the stratified SC damage as a predictor for the GLM (represented as $SC_{ij:}$). Thus the models built for each structural connection W_{ij} can be represented as (E is the expectation):

$$ln(E(C_{ij:})) = \beta_0 + \beta_1 * SC_{ij:} \tag{3.8}$$

$$ln(E(P_{ij:})) = \beta_0 + \beta_1 * SC_{ij:} \tag{3.9}$$

The fMRI correlation and partial correlation edge by edge models were multiple comparisons corrected using FDR correction with α set to 0.05.

3.2.8 fMRI streamline Functional Connectivity

fMRI data being averaged over an ROI is a heuristic rather than a necessity and enforces possibly unnecessary spatial homogeneity. To account for this, we ran a fine-grained streamline-by-streamline analysis to examine the impact of averaging fMRI data over an ROI. Using the unique pairs of voxel end-points for every streamline, we estimated the fMRI-streamline Functional Connectivity (sFC) using the correlation of that pair of voxels (see Figure 3.4). This resulted in, for every edge of the SC matrix for 114 ROIs, a set of fMRI correlations from streamlines across subjects which were intact, and a set of fMRI correlation from streamlines that were disconnected. Disconnection was inferred from whether a streamline intersected the infarct volume. We took the absolute value of these correlations and applied the Fisher r-to-z transform. We again assumed that the correlation sC_{ijkl} for ROIs i and j and streamline k for each subject l is Gamma distributed and used this as the response variable. We used an indicator variable sSC_{ijkl} that defined for ROIs i and j whether streamline k for a specific subject l was disconnected (1) or connected (0) as the dependent variable. We built Gamma GLMs that collapsed the correlation and whether a streamline was cut over subjects:

$$ln(E(sC_{ij::})) = \beta_0 + \beta_1 * sSC_{ij::} \tag{3.10}$$

We corrected for multiple comparisons using false detection rate with α set to 0.05.

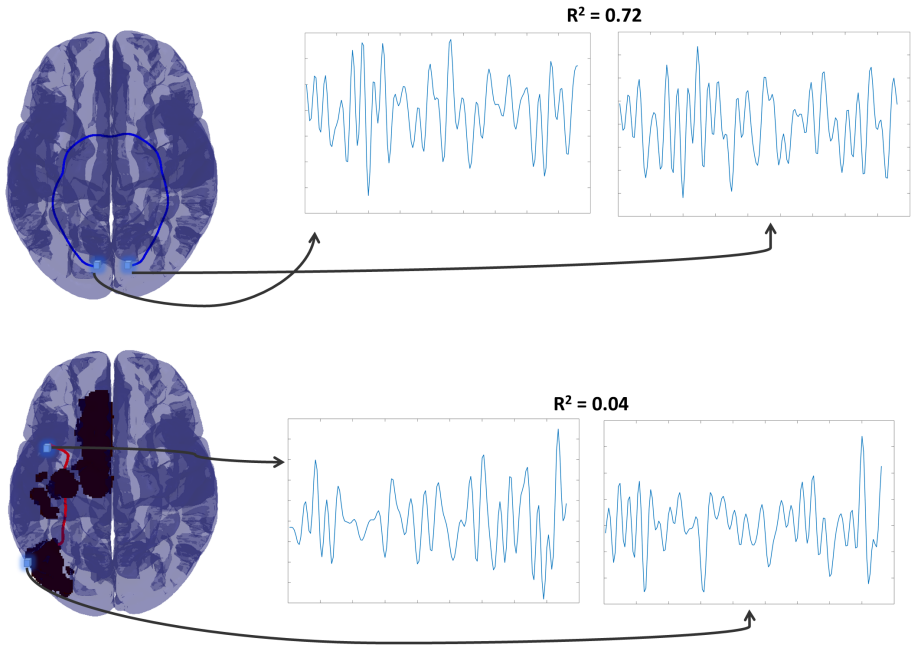

Figure 3.4: Streamline Functional Connectivity (sFC) - We show how sFC was calculated for two streamlines in two different patients. For each streamline the end points were identified as fMRI voxels and we estimated the correlation between them. We did the same for both connected (top) and disconnected streamlines (bottom).

3.2.9 Communication Models of FC

Past work [49, 51, 58, 103] has examined whether functional connectivity is generated from structural connectivity using diffusion and shortest path models of how neural activity traverses the connectome. Similarly, we simulated fMRI-FC strengths given models of diffusion and shortest path. Under diffusion, it's assumed neural activity randomly travels across the connectome when passing between any two ROIs. In contrast, under shortest path, it's assumed that neural activity takes the shortest weighted path between any two ROIs.

We estimate functional connectivity under a diffusion process using the *mean_first_passage_time.m* function from the Brain Connectivity Toolbox [82]. This function estimates the "mean first passage time" (MFPT) between any two nodes a and b which is the expected number of weighted steps for a random walker going from a to b. We standardize (subtract the mean and divide by the standard deviation) the MFPT across nodes and make it symmetric for

analyses. A lower value of MFPT for an edge indicates it is more rapidly reached by a random walker, indicating a higher expected functional connectivity. We estimate functional connectivity under a shortest path routing process using the betweenness centrality (cite) for every edge. The betweenness centrality (BC) calculates how many shortest paths use any edge in the structural connectome. We standardized the BC for our analysis. A higher value of the betweeness centrality indicates greater use by a shortest path routing process and thus, a higher expected functional connectivity. We also directly used the standardized SC weights as a third possible predictor of functional connectivity. All simulated functional connectivity were estimated using an undamaged weighted SC.

The set of edges (represented by W_{dmg}) where SC damage influenced any of our connectivity measures (FC/EC/sFC) was assumed to be a binomially distributed random variable (1 where damage influenced connection strength and 0 otherwise). We first examined using Wilcoxon rank-sum tests whether there was a significant difference in MFPT, SP and SC_{weight} between edges where damage altered connection strength and edges where it didn't. When there was a significant difference between the two groups for multiple predictors, we built a logistic regression model as follows (assuming for this example case that all three showed significant differences):

$$logit(E(W_{dmg})) = \beta_0 + \beta_1 * MFPT + \beta_2 * SC_{weight} + \beta_3 * SP \tag{3.11}$$

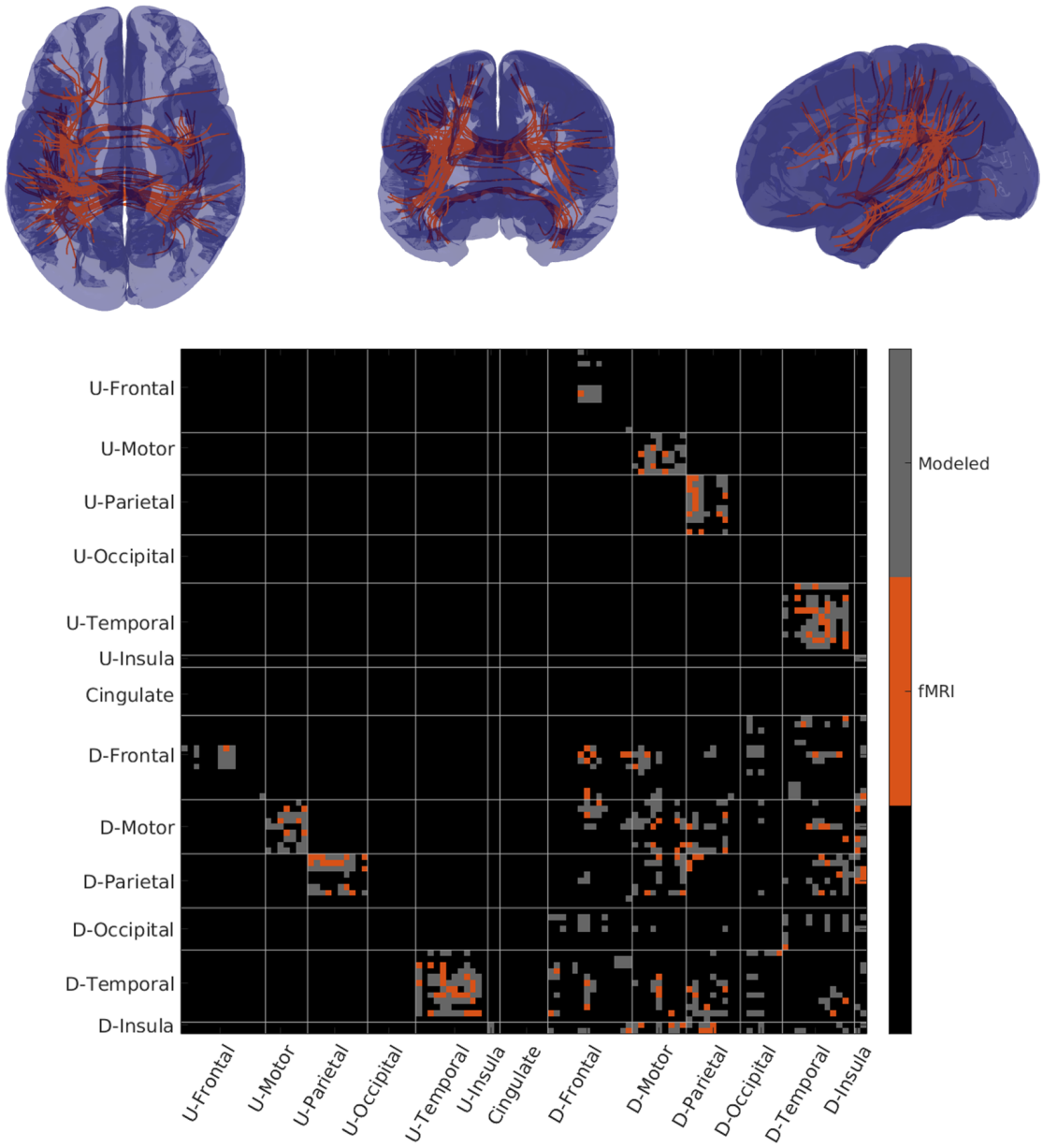

Figure 3.5: Effective Connectivity and Structural Connectivity - On the top we show representative streamlines connectivity areas for which damage influenced effective connectivity. In the center is a matrix with edges modeled in gray and edges where EC was modulated in orange. U-Areas represents sets of areas in the undamaged hemisphere and D-Area represents groups of areas in the damaged hemisphere.

3.3 Results

3.3.1 ROI level analysis show that SC damage modulates fMRI-EC but not fMRI-FC

We averaged the fMRI data over each ROI of the Lausanne parcellation. Using this data we computed the fMRI-FC and fMRI-EC between the 114 cortical ROIs. We estimated the fMRI-EC using the adaptive graphical lasso. We examined the models built between all pairs of appropriate SC edges when the response is the partial correlation/correlation, where the predictor is the presence of white matter damage. We initially only examined the set of edges where at least 3 patients showed the presence of high damage. When examining fMRI-FC we found only 1 edge was significantly modulated by damage. When using the fMRI-EC (Figure 3.5) on the other hand, 24% (80/341) edges were significantly modulated by damage (applying a FDR correction for multiple comparisons). We also tested how many edges were modulated by damage when we altered the number of patients who needed to show the presence of high damage before we modeled that edge. When we set the threshold to 5 patients, we again only found 1 edge showing the presence of damage in fMRI-FC and 22% (23/104 edges) using fMRI-EC. Finally, when we set the threshold to 7 people, in fMRI-EC 23% (3/13) edges showed the presence of damage and no edges in the correlation showed the presence of damage.

3.3.2 Voxel level analysis shows that SC damage modulates fMRI-sFC

Similar to the analysis we used when we averaged fMRI data over ROIs, we examined the streamline based functional correlation. The sFC analysis was also organized using the

114 ROI Lausanne parcellation. We built gamma GLMs between sFC and the presence of streamline disconnection for the set of edges where at least 3 patients showed high damage. We found that we could identify modulation from disconnection in the fMRI-sFC in 38% (129/341) of the edges we modeled (see Figure 3.6). We also compared how many edges showed the influence of disconnection when the set of edges was chosen based on at least 5 and 7 patients showed high damage. When 5 patients showed high damage, 36.5% (38/104) edges had sFC that was influenced by streamline disconnection and when 7 patients showed high damage then 6 out of 13 edges had sFC modulated by disconnection.

We examined the breakdown of where damage influenced EC and sFC by looking at groups of ROIs. For the sFC, we found that damage could be detected in 40% (19/48) of damaged motor connections (inter+intrahemispheric connections), 50% (8/16) of damaged occipital connections (inter+intrahemispheric connections) and 43% (48/111) of frontal connections. On the other hand for the EC, we found that damaged temporal (30% - 25/78 edges) and damaged parietal (33% - 24/72 edges) showed the impact of damage the most. For the sFC, intrahemispheric connections were more easily identified relative to interhemispheric connections - 42.5%(77/181) of edges modeled relative to 31% (50/160) of edges modeled. However, we saw this reversed for the EC where interhemispheric connections were more easily identified 27% (43/160) relative to 20% (37/181) of intrahemispheric connections modeled.

3.3.3 Relevance of SC edges modulating fMRI-FC

Using the undamaged structural connectome we estimated the mean first passage time or MFPT and betweenness centrality or BC between all pairs of nodes. We then extracted and standardized the SC weights (SC_{weight}), MFPT and BC for the 341 edges where we modeled the impact of damage (3 or more patients showing high damage). We treated these values as FC weight estimates and examined if they predicted the set of edges where we could estimate

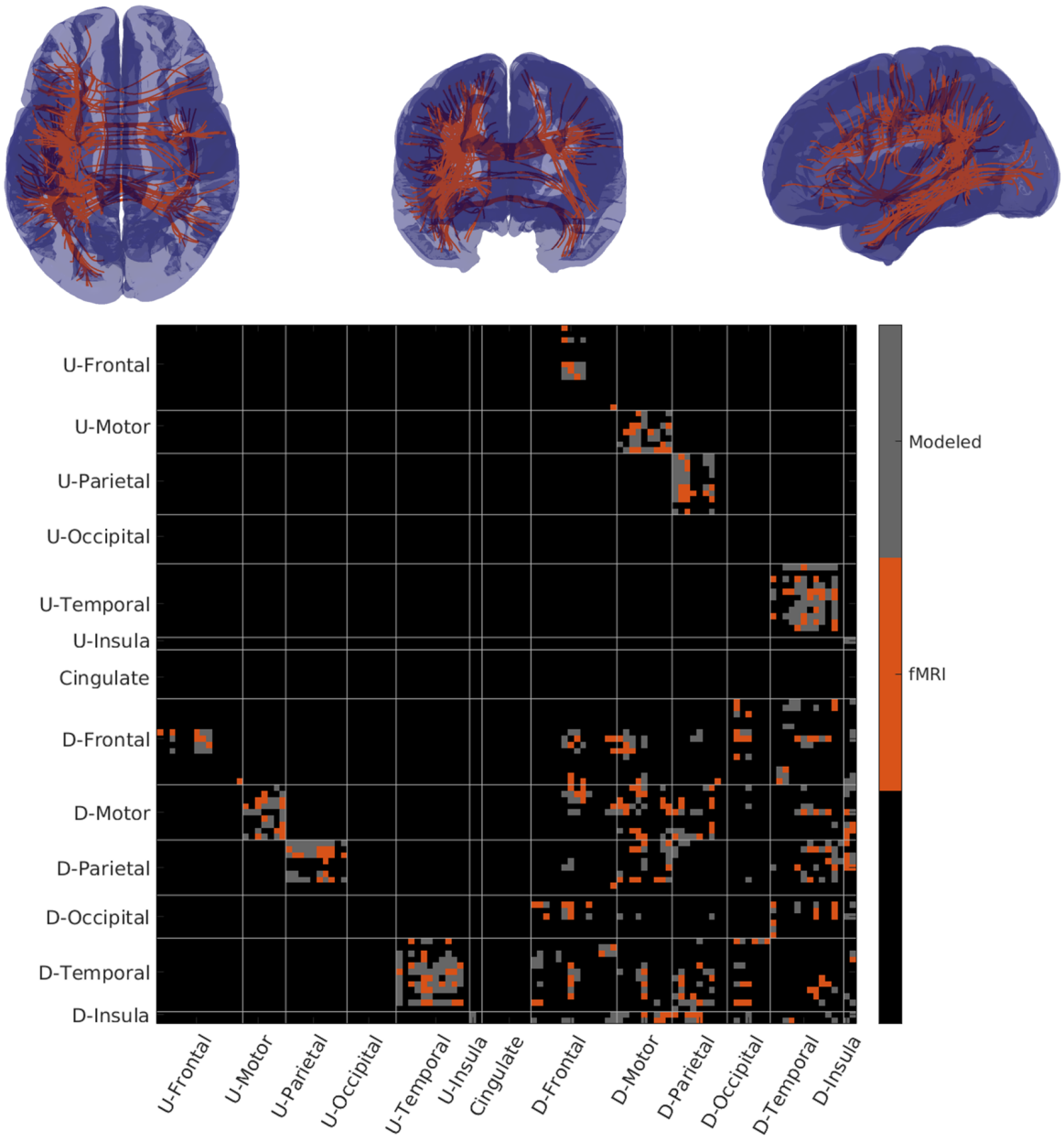

Figure 3.6: Streamline Functional Connectivity and Structural Connectivity - On the top we show representative streamline connectivity for areas for which damage influenced sFC. In the center is a matrix with edges modeled in gray and edges where sFC was modulated in orange. U-Areas represents sets of areas in the undamaged hemisphere and D-Area represents groups of areas in the damaged hemisphere.

the presence of damage in sFC and EC.

We found that all three FC weight estimates (MFPT, BC and SC_{weight}) were significantly different (Wilcoxon rank-sum test, $p < 0.05$) between edges where fMRI-sFC was modulated or unmodulated by structural damage. To see their relative influence, we used them together in a logistic regression model, with the response as a vector of length 341 x 1 with zeroes for non-modulating edges and ones for modulating edges. We found that MFPT ($\beta_{MFPT} = -0.63 \pm 0.4$; p=0.003) had a stronger influence on the odds than the betweenness centrality ($p > 0.1$) and the raw SC weights ($p > 0.1$). The negative value indicates that for a unit increase in MFPT, which indicates a reduced FC weight estimate, the odds of damage impacting the FC are multiplicatively reduced by 0.52.

We found that for the SC edges where partial correlation (fMRI-EC) was altered by damage, both MFPT and SC weights were significantly different (Wilcoxon rank-sum test, $p < 0.05$) between edges where fMRI-EC was modulated or unmodulated by structural damage. To identify which predictor was most important we first put both predictors into a single model. In a single model, neither of the predictors were significant, further the full model itself was also not significant. In separate models for each predictor, we again found neither predictor to be significant. Examining the parameter estimates in the separated models, $\beta_{SC_{weight}} = 0.19 \pm 0.11$ ($p = 0.11$) and $\beta_{MFPT} = -0.14 \pm 0.12$ ($p = 0.24$) suggested that SC weight has relatively stronger influence on the odds. This is consistent with the fMRI-EC being a measure of direct statistical dependence, removing the influence of any indirect connections.

3.4 Discussion

Using an estimate of structural connectivity damage in stroke using virtual tractography and novel model based estimates of fMRI-EC we examined how SC damage modulates fMRI-FC,fMRI-EC and fMRI-sFC. We estimated structural connectivity damage in stroke using virtual tractography. Further, we examined novel model based estimates of fMRI-EC. We found that using an estimate of the effective connectivity, the partial correlation, allowed us to estimate modulation of EC under damage in 24% of the edges modeled. Edges that showed the influence of damage were edges with stronger SC weights. Using our fine-grained, streamline by streamline correlation analysis we identified that SC damage modulated 38% of the edges modeled. The edges where SC damage modulated the fMRI-sFC were edges that were reached more rapidly by neural activity traversing the SC through a diffusion process (random walks).

The relationship between structural and functional connectivity when there is damage to brain anatomy is less clear has been investigated in animal models. In an fMRI study with macaques[50], corpus callosectomy lead to significantly decreased fMRI functional connectivity between hemispheres but only when both anterior commissure and corpus callosum were transected. In one monkey where the anterior commissure was spared, fMRI functional connectivity between hemispheres was nearly the same as prior to transection, suggesting anatomical damage may not always lead to reduced functional connectivity because functional connectivity is influenced both by mono-synaptic and poly-synaptic pathways ([49, 58]). In another macaque study, the amygdala was inhibited using DREADDs and functional connectivity between amygdala and the rest of the brain was shown to decrease [52]. The decrease in functional connectivity could be predicted by a model of neural communication over the structural conectome that incorporated all walks (potentially repeated poly-synaptic pathways) across the structural connectome (communicability). In a mouse study of the structure to function link link[42], demyelination lead to reduced partial cor-

relations for long range connections in the mouse brain. Thus, damage to the structural connectivity may or may not influence functional connectivity (which includes indirect connections) but a measure of effective connectivity (partial correlation) is more likely to be sensitive to damage.

In this study we found that damage doesn't modulate fMRI functional connectivity measured at the ROI level. Effective connectivity, as we expected, does show the impact of damage, though in a circumscribed set of edges. Past work employing the partial correlation to examine structural connectivity to effective connectivity relationships have been few. In humans, partial correlation was used to study the voxel-level effective connectivity and its relationship to the structural connectome [41]. In [41], the authors found that while a significant relationship existed between voxel-level effective connectivity and the structural connetome, the correlation between them was comparable to the correlation between voxel-level functional and structural connectivity. Another study [108] found that that structural connectome edge strength was more correlated to the variability of effective connectivity across multiple sessions but not functional connectivity suggesting effective connectivity is a more robust estimate. Our work is in line with this, since, first, damage seems more linked to fMRI-EC than to fMRI-FC and second, by assuming partial correlation was gamma distributed, we constrained both the mean and the variance.

fMRI data has millimeter scale spatial resolution of neural activity. However, when estimating the fMRI-FC and fMRI-EC, we removed this source of variability by averaging over an ROI in an effort to improve signal to noise ratio. By using fMRI-sFC, we tried to examine fMRI data at the scale at which it measures neural activity. One other study followed a similar approach [109]. The authors of [109] found that when only examining pairs of voxels with a direct structural connection, and estimating a pseudo functional connectivity from the structure using all polysynaptic paths, they saw a correlation of 0.26 between the pseudo functional connectivity and empirical functional connectivity. When the authors of [109]

used all voxels and correlated their estimate of the pseudo functional connectivity with the empirical functional connectivity, they saw a correlation of 0.18 across 5000 voxels (note that 61% of voxels were disconnected i.e. pseudo functional connectivity was 0). However, when looking at the correlation between structural and functional connectivity at the voxel level [41], correlations are much weaker - 0.046 at 40000 voxels. This suggests that choosing voxels using streamlines may be a good approach to constrain the fMRI data space to that accessible to tractography applied to diffusion weighted imaging. In our work, we saw this was indeed the case, with fMRI-sFC being modulated by streamline disconnection across 38% of the edges modeled.

We know the structural connectome to functional connectome link is highly variable [53] and depends upon the parcellation applied [99] and how the functional connectome is estimated [100]. However, by assuming a generative model operating over the structural connectome studies have shown greater alignment between structural and functional connectivity [49, 51, 58]. Following up on this work, we examined whether specific communication models (diffusion/shortest path) could be distinguished based on the set of edges where damage was linked to altered fMRI-sFC and fMRI-EC. We found that edges where damage influences fMRI-sFC are relevant when neural activity passes through random walks across the SC than those where pairs of nodes had the shortest paths between ROIs. This suggests that we cannot ignore how an edge is placed relative to the rest of the network, and also that functional connectivity leverages diffusion over shortest paths for communication over a static structural connectome. On the other hand, fMRI-EC was more likely to show modulation for edges where the SC weight is higher. This suggests that, as we might expect, when using the effective connectivity, an estimate of direct connection strength, the SC weight differentiates modulated and non-modulated edges. Overall, this suggests that network context matters for seeing the influence of damage. However, the network context that is relevant depends on how connectivity is estimated.

Several factors influence our ability to see the influence of damage on the fMRI-sFC or fMRI-EC. First, virtual tractography ignores individual variability in white matter. Estimating structural connectivity damage even with diffusion imaging for patients of stroke is challenging ([110]). Kuceyeski et al. (2013) first suggested estimating structural connectivity relative to a template built from healthy controls. We used a streamline template generated by Yeh and colleagues from the HCP-842 dataset[68]. They filtered out streamlines based on anatomical priors and expert knowledge, thereby creating a template with fewer false positives (a known problem with tractography estimates[98]). Individual differences in the structural connectome are more limited than individual differences in functional connectivity [101] suggesting that virtual tractography a reasonable method to estimate SC damage. Future work will ideally compare an estimate of the white matter integrity in patients of stroke to estimates of the structural connectivity when using virtual tractography.

Another methodological limitation of this study is the use of a common space (MNI template) to run our analyses. While this is problematic, we saw it as a useful way to avoid issues of transformations [110] in the presence of lesions. Finally, we use streamline end points to estimate fMRI-sFC. However, there will be cases where these end points are distant from gray matter. In our analysis procedure, when this is the case, there will be no fMRI signal at the voxels, and hence this streamline does not contribute to discrimination using fMRI-sFC.

Despite these caveats, we found that we could see the influence of damage in 24% of edges when using a measure of effective connectivity and in 38% of the edges when using streamline functional connectivity. Given how we see that network context makes a large impact on the ability to see the impact of damage, we hypothesize that having data from multiple days or appropriate tasks will make it possible to see the impact of damage across all edges modeled when using fMRI streamline functional connectivity. However, there may be intrinsic limitations to using effective connectivity to see the impact of damage partly due to its coarse grained nature.

Chapter 4

Influence of damage to the Structural Connectome on EEG Effective Connectivity

4.1 Introduction

The ability to elucidate the human structural connectome, the set of anatomical connections between brain regions, using diffusion weighted imaging and tractography has been a huge leap forward for macroscale systems neuroscience [6]. The structural connectivity scaffold is expected to constrain and modulate the macroscale functional activity, as measured for example by electroencephalography (EEG). Studies probing this relationship have however been far and few between for several reasons [54, 55]. A major reason is the low intersubject variance in structural connectivity as opposed to functional connectivity (as estimated from both EEG). Studies examining the intersubject correlation of structural connectivity and functional connectivity have shown that there is much higher correlation between subjects'

structural connectomes than there is between their functional connectomes [55, 102]. Additionally, work has shown that there is simply greater variability in the functional connectivity (fMRI) than there is in the structural connectivity [101]. Also, functional connectivity measured with EEG will vary with brain state, so we can only expect any particular EEG signal to partly reflect the structural connectome.

In examining connectivity with EEG, several methodological difficulties must be overcome. After source localizing EEG data to reduce the effects of volume conduction (spread of current from sources in the brain through the tissues of the brain, skull and scalp [27]), we examine activity at regions of interest within the brain rather than at sensors. We are faced then with the problems of leakage effects [30, 84] and common inputs. Leakage effects occur when two sources in the brain aren't completely distinguishable due to the nature of their location and orientation. Leakage effects show up as spurious correlated source activations. A second issue is common input effects - two sources receiving (either simultaneously or at a delay) activity from a third source will show correlated activity. We reduce the problems of leakage effects and common inputs by using effective connectivity or model based connectivity estimates such as graphical models to estimate the precision (inverse of the covariance). The precision estimates the strength of a connection between two sources when accounting for variance shared with all other sources, so it estimates "direct" connections, and reduces the influence of leakage effects and common inputs. In this way we examined EEG estimates of effective connectivity that are the ideal points of comparison to the structural connectivity.

Each patient of stroke has unique lesions, leading to large individual differences in damage to the structural connectome. The variability in damage across patients provides an interesting window on the impact of structure on functional activity as measured in EEG, potentially informing us of how different frequency bands are modulated by the presence of structural damage. We estimate the SC for each patient using virtual tractography [105, 106] and use novel model-based estimates of EEG connectivity - partial coherence and partial correlation

- which we jointly refer to as EEG-Effective Connectivity or EEG-EC. We analyzed the relationship of the EEG-EC to the structural connectivity at two levels. The first is the broad connectome scale, where we examined the relationship between average connectivity strength in the structural connectivity and EEG-EC. The second spatial scale we examined is across the individual edges of the connectome that show the presence of damage. We look at these two levels because (1) we found that summarizing network characteristics is a robust way to identify the relationship between structural connectivity and EC (described in Chapter 2) and (2)Past work has shown that the impact of stroke can be diffuse and visible in connectivity changes between an ROI and the rest of the brain [111], and in the graph theoretic properties of the whole network [111–113]. However, this does not tell us how and whether individual edges are affected by the presence of damage, which we saw was possible to see when using fMRI effective connectivity (discussed in Chapter 3). To test this, across all pairs of 114 cortical ROIs from the Lausanne parcellation[66] where sufficient SC damage across subjects permitted modeling, we examined if SC damage altered the EEG-EC.

We examine two different stroke subgroups - subacute ($<$1 month) and chronic ($>$ 2 months). When using fMRI data for subacute patients we found that we could easily identify the influence of damage (discussed in Chapter 3). The authors of [114] used dynamic causal modeling to show how reinstatement of ipsilesional effective connectivity from subacute to chronic periods for the same set of subjects led to improved behavioral outcomes. We would expect based on these results that structural connectivity damage alters the EEG functional connectivity, and thus, by extension the EEG-EC. In subacute and chronic patients, we expect different patterns of EEG effective connectivity (and EEG-EC) due to plasticity and reorganization.

4.2 Methods

4.2.1 Modeling Framework

Overview

A template of brain connectivity was developed for use in the EEG data analysis presented here. This model is based on tractography analysis of the DTI data from the HCP 842 data set, which is a group average template constructed from 842 subjects [68]. We combine these streamlines with the Lausanne parcellation [66] to define 129 regions of interest (ROI) and a structural connectivity model. The Lausanne parcellation was also used to define a source model and inverse solutions.

At the core of the data analytic strategy presented here is the notion that the structural connectivity model constrains the statistics of EEG signals. We use two multivariate Gaussian models of effective connectivity to constrain the source activity: (1) complex-valued Gaussian graphical model, where the structural connectivity determines the precision (inverse covariance) of the complex-valued multivariate normal distribution that generates the *amplitude and phase* of source activity in a frequency band, and (2) amplitude Gaussian graphical model, where the structural connectivity determines the precision of a multivariate normal distribution that generates the *amplitude* of source activity in a frequency band. The first model is a generative model of coherence, as widely used in EEG and MEG studies ([21, 26, 27]). The second model is a generative model of amplitude correlation which has been recently introduced in the MEG literature, as an analog of fMRI functional networks ([19, 24, 67]).

Structural Connectivity (SC) Model

We used streamlines generated with deterministic tractography by Yeh et. al. [68] using the HCP842 dataset [8] transformed to the MNI152 template brain pulled from FSL. We transformed the Lausanne parcellation [66] of 114 cortical and 15 subcortical ROIs to the MNI152 template brain and generated a volumetric representation for each ROI using the *easy_lausanne* toolbox (Cieslak,2015). Each streamline was approximated by a single 100-point cubic spline using code adapted from the along-tract-stats toolbox [69]. By identifying the streamlines which ended in a pair of ROIs we were able to create the structural connectome for the Lausanne parcellation. Each streamline only connected a single pair of ROIs.

We drew lesion masks on T1-weighted MRIs, informed by the corresponding T2 FLAIR images. For one subject unable to complete an MRI scan, we drew the lesion mask on their corresponding CT scan. Infarct masks were binarized and spatially transformed to MNI space. Right hemisphere lesions were flipped to the left hemisphere, thus the ipsilesional hemisphere is always the left hemisphere. We intersected these lesion masks with the predefined streamlines for the undamaged SC. Using the reduced set of streamlines, we define individual structural connectomes. We graphically show this process in Figure 4.1. By identifying the streamlines which ended in a pair of ROIs we were able to create the structural connectome for the Lausanne parcellation. Any edge W_{ij} was defined as (for ROIs i and j connected by streamlines s of length l):

$$W_{ij} = \sum_{s_{ij}} \frac{1}{l_{ij}} \tag{4.1}$$

We weight the streamlines by length to reduce the bias of tractography algorithms towards longer streamlines [70]. From this process we built the $129 * 129$ weighted structural connectome with 1132 edges. We reduced this matrix to $114 * 114$ with 720 edges (see Figure

1) after removing all the subcortical structures and limiting interhemispheric connections to known homologous white-matter tracts. This latter step helped remove potentially noisy estimates of connections where streamlines intersected and passed outside the cortical surface before reaching the terminal point in a brain region. The resulting model of structural connectivity shown in Figure 1 is referred to as the structural connectome (SC). This model is incomplete in that it does not include thalamocortical projections, and thus there may be functional connectivity that is a result of structural connections outside of this SC. Our estimation procedure described in the next section allows for such connections.

There was considerable variability in the set of connections that were damaged by the lesions across chronic and subacute groups of patients. We found through visual examination of the distribution of damage to edges that the distribution was skewed or showed bimodal behavior. We decided to stratify damage based on this observation. Each edge for each patient was designated as either high or low damage. High damage indicated that, for that edge, connection strength was less than the midpoint of the range of connection strengths. We show how many edges have high damage across patients in Figure 4.1. We found that over half of the connections showed high damage in few to no patients. When categorizing the damage in this way, we found that 462 (343) edges showed high damage across at least 3 patients among chronic (subacute) patients.

EEG Forward Modeling

The EEG forward model is an estimate of the potentials measured at EEG sensors above the scalp generated by current sources located in the brain. For the data analysis presented in this paper, we made use of the 256 channels of the Hydrocel EGI cap.

The head model was developed from the fsaverage MRI images from the Freesurfer toolbox [73]. The tesselated cortical surfaces for right and left hemisphere were extracted

using the recon-all pipeline in Freesurfer and then downsampled to 81000 (81k) vertices (*mris_decimate* from Freesurfer). We used this surface to constrain dipole orientation and define the volume of the model corresponding to the cortex. We generated the inner skull, outer skull and scalp surfaces approximated with 2562 vertices from the fsaverage head generated using the *mri_watershed* function. Using these surfaces, and with the conductivities of scalp, CSF and brain set at 1 S/m and the skull at 0.025 S/m (i.e., 40 times lower conductivity), we used OpenMEEG [74] to compute a Boundary Element Model (BEM) to generate the EEG forward matrix. Each row of the EEG forward matrix is the potential gradient detected across all 256 sensors from a unit current density source at one of the 81k cortical surface vertices.

Using the Lausanne parcellation for 114 cortical ROIs, we divided the cortical surface and identified vertices belonging to each ROI using the volumetric parcellation of the fsaverage brain. Using this organization of vertices we then reduced the representation for each ROI down to a set of 3 dipoles in the x, y and z directions at a single location. The location for each ROI (Loc_i for the i'th ROI) was selected by taking a weighted average of vertex locations (V_{ij} for the j'th vertex of the i'th ROI), using the following equation (where c is channels and W represents the number of vertices in an ROI):

$$Loc_i = \frac{1}{\sum_{j=1:W} \sum_{c=1:256} L_{ijc}^2} \sum_{j=1:W} ((\sum_{c=1:256} L_{ijc}^2) * V_{ij}) \tag{4.2}$$

In this way we reduced our source model to 114 source locations, with 3 sources at each location in the canonical x,y, and z directions. We computed a new EEG forward matrix ($\boldsymbol{M}$) of dimension 256 * 342 using OpenMEEG. This EEG forward matrix captures the (linear) mixing of source activity at the sensors to generate the measured EEG signals.

Effective Connectivity Model - Complex Valued Gaussian Graphical Model (cGGM)

The template of structural connectivity derived from HCP 842 [68] gives us potential constraints on the connections between ROIs, and more importantly, which ROIs are not connected by white-matter tracts observable with DTI. In order to use this information to model EEG data, we assume that the vector of source activity ($\mathbf{Z}$) at all ROIs in one frequency band are samples drawn from a **complex-valued** multivariate Gaussian random process (where Φ is the precision):

$$Z \sim N(\mathbf{0}, \mathbf{\Phi}) \tag{4.3}$$

The EEG fourier transformed signal is characterized by samples of amplitude and phase, or equivalently, by a Fourier coefficient with real and imaginary parts corresponding to sine and cosine components of the signal. For frequency domain data that are complex-valued, we make use of a complex-valued normal distribution. The complex-valued multivariate Normal for a zero-mean (where $E(\boldsymbol{Z}) = 0$) complex-valued Gaussian process [71] is defined as:

$$\rho(\mathbf{Z}) = \frac{1}{\pi^n det^{\frac{1}{2}}(\mathbf{\Theta})} \exp\left(-\frac{1}{2}\mathbf{Z}\mathbf{\Theta}^{-1}\mathbf{Z}^H\right) \tag{4.4}$$

where

$$\mathbf{\Theta} = \begin{bmatrix} \mathbf{R}_{\mathbf{zz}} & \widetilde{\mathbf{R}}_{\mathbf{zz}} \\ \widetilde{\mathbf{R}}_{\mathbf{zz}}^H & \mathbf{R}_{\mathbf{zz}}{}^H \end{bmatrix} \tag{4.5}$$

and

$$\mathbf{R}_{\mathbf{zz}} = E[\mathbf{z}\mathbf{z}^H]; \widetilde{\mathbf{R}}_{\mathbf{zz}} = E[\mathbf{z}\mathbf{z}^T] \tag{4.6}$$

The key parameter in this model is the covariance matrix Θ and its inverse, the precision matrix $\Phi = \Theta^{-1}$. As defined in equation 4.5 and 4.6, the covariance matrix for complex valued data is composed of the familiar cross-spectrum R_{zz} and the complementary cross-spectrum $\widetilde{R}_{zz}$. Most spectral analysis methods only make use of R_{zz} and implicitly assume circular symmetry, i.e., $R_{z_1 z_2} = 0$ (Schrier and Scharf, 2010). In this case, the complex-valued data is labeled as *proper*. With the assumption of circular symmetry, we can parameterize the complex-valued Gaussian using the precision defined as the inverse of the cross-spectrum, $\Phi = \Theta^{-1} = R_{zz}^{-1}$. Each value in the precision matrix Φ is the conditional covariance between any two variables (here, sources representing two ROIs) given the other variables (here, sources representing all other ROIs). The precision removes linear effects from all other sources from the covariance between any pair of sources, and provides a model of *effective connectivity* between sources. For any pair of sources, if the precision is zero, there is no need for a direct connection between the sources in order to account for observed coherence (functional connectivity). Such apparent coherences arise from connections mediated via other sources in the model. In our model, the precision matrix Φ captures the statistics of effective connectivity and has nonzero entries only at edges (pairs of ROIs) that have a connection estimated from DTI in the structural connectome. We are assuming that in each frequency band the connectivity we estimate arises from random fluctuations at each area becoming correlated by the structural connectome. In the EEG data analysis, we estimate the source precision matrix Φ from the EEG data in each frequency using graphical modeling techniques that inform the precision estimate with the structural connectome estimated from the HCP-842, but allowing the precision values to be determined by the data.

Effective connectivity model - Amplitude Gaussian Graphical Model (aGGM)

We use the structural connectivity to constrain potential connections due to correlated amplitude envelope fluctuations between ROIs, thereby defining the generative model of amplitude

correlation. We assume that the vector of source activity amplitudes ($\mathbf{X}$) at all ROIs in one frequency band are samples drawn from a **real-valued** multivariate Gaussian random process (where Φ is the precision with non-zeros entries where there are structural connectome connections):

$$X \sim N(\mathbf{0}, \mathbf{\Phi}) \tag{4.7}$$

When examining amplitude, we look at samples X of amplitude estimates from the fourier coefficients from a single frequency band of the EEG signal across epochs. So for amplitude data we use a real valued multivariate normal distribution as characterizing the fluctuations of amplitudes in different frequency bands. And the multivariate normal for a zero mean, i.e., (where $E(\boldsymbol{X}) = 0$) is defined as:

$$\rho(\boldsymbol{X}) = \frac{1}{\pi^n det^{\frac{1}{2}}(\Theta)} \exp\left(-\frac{1}{2}\boldsymbol{X}\Theta^{-1}\boldsymbol{X}^T\right) \tag{4.8}$$

This distribution is fully parametrized by the precision matrix $\Phi = \Theta^{-1}$. As with the cGGM, each value in the precision matrix Φ is the conditional amplitude covariance between any two sources given the other sources. The precision provides a model of *amplitude effective connectivity* between sources. For any pair of sources, if the precision is zero, there is no need for a direct connection between the sources in order to account for observed amplitude correlation (functional connectivity).

In our graphical model of amplitude fluctuations, the precision matrix Φ captures the statistics of effective connectivity and has nonzero entries only at edges (pairs of ROIs) that have a connection estimated from DTI in the structural connectome. We are assuming that in each frequency band the connectivity we estimate arises from random fluctuations in amplitude at each area becoming correlated by the structural connectome. In the EEG data analysis (both for the simulation and real data), we estimate the source precision matrix Φ in each

frequency band using graphical modeling techniques that inform the precision estimate with the structural connectome estimated from the HCP-842, but allowing the precision values (edge weights) to be determined by the data.

4.2.2 Estimation of Effective Connectivity

Overview

The estimation of the complex-valued Gaussian graphical model or the amplitude Gaussian graphical model from the EEG data proceeds in three steps. First, the EEG data is transformed to the frequency domain using a fast fourier transform(FFT). Second, an inverse solution is applied to estimate the ensemble source activity over the observations, using broadband activity. Third, graphical modelling methods are used to estimate the precision matrix of a Gaussian graphical model of the effective connectivity. For the complex Gaussian Graphical Model we used took the mean over the cross spectral density matrices for the frequency band of interest before estimating the precision. While for the amplitude Gaussian graphical model we used the absolute value of the Fourier coefficients before estimating the covariance and taking the mean over the frequency band of interest. Graphical modeling involves the choice of regularization parameters. We set these parameters beforehand and examined performance over a range of penalization.

Inverse Solution to estimate source activity from EEG

We can represent each sample of the EEG data, as a vector $\boldsymbol{B}$ of length equal to the number of EEG sensors. The set of samples of $\boldsymbol{B}$ is related to source activity $\boldsymbol{S}$ of length equal to

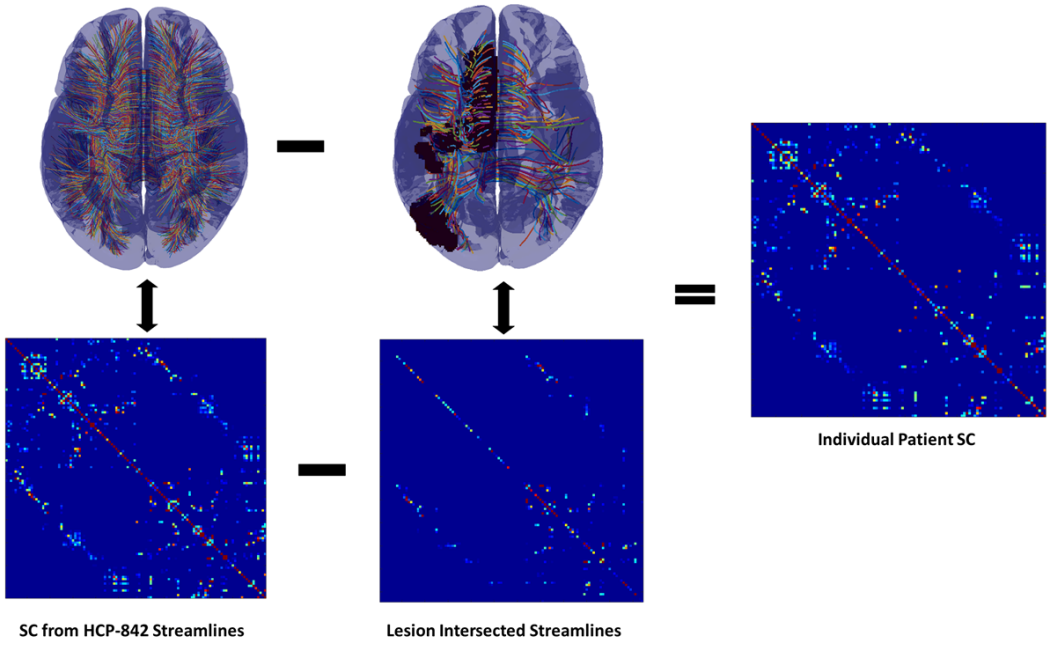

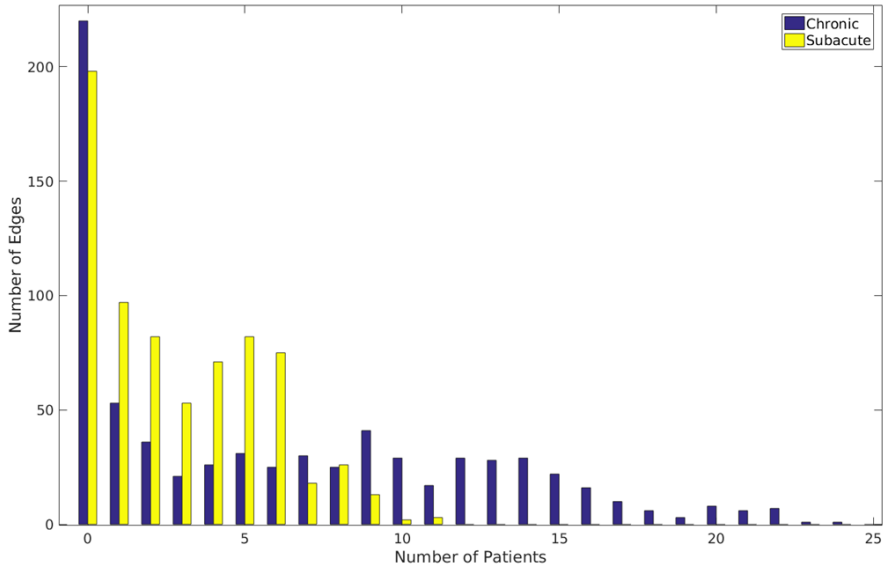

Figure 4.1: Virtual Tractography - in (a) we show the pipeline for virtual tractography. We remove from the set of streamlines that represent the undamaged structural connectome (top left) the streamlines intersecting any particular patient's lesion(s), as shown in the top middle figure. Using the reduced set of streamlines we apply the Lausanne parcellation to get the final structural connectome for that patient (shown on the right). (b)Edges Showing High Damage Across Chronic and Subacute Groups - We show the number of edges where patients show high damage.

the number of EEG sources:

$$\mathbf{B} = \mathbf{MS} \tag{4.9}$$

where $\boldsymbol{M}$ is the EEG forward matrix. For each participant, we localized activity to the 342 sources by inverting the reduced lead field using regularized minimum norm estimation (weighted L2 norm, [29]) and applying it to data at the scalp. We estimate the inverse M^{-} using (where ν is penalization applied):

$$diag(\boldsymbol{W}) = ||\boldsymbol{M}||_2 \tag{4.10}$$

$$\boldsymbol{M}^{-} = (\boldsymbol{MW})^T((\boldsymbol{MW})^T * (\boldsymbol{MW}) \ + \ \nu \boldsymbol{I})^{-1} \tag{4.11}$$

Using the estimated source activity S as $M^{-}B$, we identify the 3 x *samples* matrix at each ROI for the dipoles along the x, y and z directions. Using a singular value decomposition at each ROI of the 3x*samples* we identified the optimal orientation of the dipole as the first singular vector. Using the first singular vector, we reduced the lead field from 204x342 to 204x114. This reduced lead field was the individual specific (adaptive) lead field. We source localized data to the 114 ROIs for the individual lead field.

Adaptive Graphical Lasso using SC-QUIC

The graphical lasso [32] is a method that has been applied in multiple fields in the past decade, from genomics [75], to fMRI functional connectivity ([76], [37]) and climate models [77]. This is a method used to identify a sparse approximation to the precision matrix. In this way, estimates in the precision are more robust for the values that are retained. In order to apply the lasso, we use the penalized likelihood function as follows ([33]) to estimate the

precision (where Θ is the covariance or cross-spectral density):

$$\hat{\Phi} = argmin_{\Phi \succ 0} \left(-log(det\Phi) + tr(\Theta\Phi) + \lambda \sum_{j<k} |\Phi_{jk}| \right) \tag{4.12}$$

The penalization parameter λ in the graphical lasso determines the important set of partial coherence/correlation values. The output of the lasso from Equation 4.12 is the precision matrix $\hat{\Phi}$, which represents directly the complex Gaussian Graphical (cGGM) or Gaussian Graphical model. For our purposes, we ran the lasso optimization from QUIC ([78]) using a matrix penalty term (this process is also called the adaptive lasso - [79]) determined by the structural connectome (SC) with edges W (and $\lambda_1 = \lambda_2$):

$$\hat{\Phi} = argmin_{\Phi \succ 0}$$
$$\left(-log(det\Phi) + tr(\Theta\Phi) + \lambda_1 * \sum_{j<k; W_{jk} \in SC} |\Phi_{jk}| + \lambda_2 * \sum_{j<k; W_{jk} \notin SC} |\Phi_{jk}| \right)$$

We set the $\lambda_2 = 0.2$ - the penalization for edges outside the SC, and the penalization inside the SC - $\lambda_1 = 0.05$. We also examined the results for penalization within a range around λ_1 and ensured that our results weren't strongly influenced by the penalization applied. Past work along these lines [43] has used the SC weight directly to determine the penalization weighting, we choose not to do this. We expect that the SC weights will potentially constrain connectivity strengths. However, we do not expect the SC strengths to map directly onto the effective connectivity strengths. By using a template, we are assuming a common SC across participants, so the expected weight may differ. Further, the structural connectome can be expected to be used differently across frequency bands yielding different effective connection weights. For this reason we use the binarized SC to determine the penalization structure.

By optimizing the above penalized likelihood, we leveraged the information in the SC as a prior for our lasso estimate. The output of the lasso when optimizing Equation 3.3

is the (c)GGM. We derive our graph G with vertices $V = 1, 2, ...C$ and edges $W_{est} = G_{ij} = 1, i, j \in V$ from the (c)GGM based on the non-zero values in $\hat{\Phi}$. The final precision matrix $\tilde{\Phi}$ is estimated under the Gaussian likelihood for the set of edges W_{est} defined by the graphical model using the function $ggmFitHtf$ (PMTK3 toolbox [80]) which optimizes (unpenalized Gaussian log-likelihood):

$$\tilde{\Theta}^{-1} = argmin_{P \succ 0; |P|>0=G} - (log(detP) + tr((\Theta + \delta * I)P)) \tag{4.13}$$

Since Θ (covariance) is usually rank deficient, we add a small value (δ) along the diagonal to make it full rank. We define *delta* as 0.001 times the maximum value along the upper triangle of the covariance.

Partial Coherence and Partial Amplitude Correlation

In every frequency band, we estimated two graphical models. We estimated the complex Gaussian Graphical model to estimate the precision for complex valued data incorporating amplitude and phase and the amplitude Gaussian Graphical model for the real valued amplitude data. For the cGGM we estimate the partial coherence (PC) as a summary statistic [81]:

$$PC_{z_1 z_2} = \left| \frac{\Phi_{z_1 z_2}}{\sqrt{\Phi_{z_1 z_1} * \Phi_{z_2 z_2}}} \right|^2 \tag{4.14}$$

For the aGGM we estimate the partial correlation (APC) as a summary statistic as (assuming the precision matrix Φ here is the output from estimating an aGGM):

$$APC_{x_1x_2} = \left| \frac{\Phi_{x_1x_2}}{\sqrt{\Phi_{x_1x_1} * \Phi_{x_2x_2}}} \right| \tag{4.15}$$

4.2.3 Data Analysis

Subjects were recruited from the UC, Irvine Medical Center. Twenty five subacute patients had suffered stroke between 3 to 26 days prior to being enrolled in the study. Thirty seven chronic patients had suffered stroke between 76 days to 9 years prior to being enrolled. The mean age of patients with subacute stroke was 57.404 $\pm$ 14.46 years (range 27-79), while that of chronic patients was 56.38 $\pm$ 14.68 years (range 23-75). Fugl-Meyer scores for all patients ranged from 8 to 65 (with an expected score of 66 for someone without motor difficulties), subacute patients had a mean of 42.9 while chronic patients had a mean of 42.7 (no significant difference, $p > 0.1$, Wilcoxon rank sum test).

EEG

We recorded eyes open resting state EEG for 3 minutes from subjects using high-density electroencephalography (EEG) from Electrical Geodesics, Inc.s 256-channel Geodesic Sensor Net and Advanced Neuro Technologys amplifier at a sampling rate of 1000 Hz. This data was filtered between 0.5 Hz to 100 Hz before being epoched into seconds. We performed manual artifact removal of high variance trials and sensors and subsequent ICA based eyeblink artifact removal before transforming the data back into channel space. Sensors were flipped across hemispheres when necessary so that the left hemisphere was always the lesioned hemishphere. We defined six frequency bands for analysis - Delta (1-3 Hz), Theta (4-7 Hz), Alpha (8-13 Hz), Lower Beta (14 -20 Hz), Upper Beta (21-30 Hz) and Gamma (31-50 Hz).

Modeling Impact of SC damage

After estimating cGGM and aGGM models for the 6 frequency bands of interest, we estimated the summary statistics of partial coherence and partial correlation. We transformed the partial coherence and partial correlation across subjects by taking their absolute value and applying Fisher r-to-z transforms. We added a small value (10^{-4}) to make all values non-zero (gamma distribution is undefined for 0). Let P_{ijk} represent the transformed partial correlation or partial coherence between ROIs i and j for subject k. We treat the P_{ijk} as Gamma distributed variables because the values are positively valued and tend to be skewed towards the positive axis of the real line. Using this notation, $C_{ij:}$ and $P_{ik:}$ represent the response vectors for a gamma generalized linear models using a log link function. We used the stratified SC damage as a predictor for the GLM (represented as $SC_{ij:}$). Thus the models built for each structural connection W_{ij} can be represented as (E is the expectation):

$$ln(E(P_{ij:})) = \beta_0 + \beta_1 * SC_{ij:} \tag{4.16}$$

The edge by edge models were multiple comparisons corrected within each frequency band using FDR correction with α set to 0.05.

Modeling Degrees between SC and EC

Degrees for a weighted network $G = \{V, E\}$ represent the summed weight of connections E made by a node V in the network. In our analysis, nodes are the ROIs defined by the Lausanne parcellation. For a network G, the mean degrees across all ROIs is then defined

as (where n is number of ROIs and i and j represent ROIs):

$$D = \frac{1}{n} \sum_{i=1:n} (\sum_{j=1:n} E_{ij}) \tag{4.17}$$

We estimated the correlation between the D across patients from the SC with the D estimated from the amplitude partial correlation or the partial coherence.

4.3 Results

4.3.1 Edge Analysis Showed Weak Modulation from Damage

We source localized EEG data to the 114 regions of the Lausanne parcellation. Using this data we computed the cGGM and aGGM between the 114 cortical ROIs using the adaptive graphical lasso for each patient. We examined the models (gamma distributed GLMs) built for SC edges where the response is the partial coherence/partial correlation, and the predictor is the presence of white matter damage across subjects (subacute). We examined the set of edges where at least 3 patients showed the presence of high damage and at least 33% of (subacute) patients had a non-zero EC estimate to ensure robust models were being estimated. When examining EEG-PC (cGGM) across all frequencies (FDR corrected within frequency) we found only 8 (out of 132) unique edges were significantly modulated by damage. When using the EEG-APC (aGGM) on the other hand, we found only 16 (out of 157) unique edges among subacute patients were significantly modulated by damage.

We ran the same analysis edge by edge as described earlier now limited to patients in the chronic stroke group. Once again, we examined the set of edges where at least 3 patients

(from the chronic population) showed the presence of high damage and at least 33% of patients had a non-zero EC estimate to ensure robust Gamma GLMs were being estimated. When examining EEG partial coherence (cGGM) across all frequencies (FDR corrected within frequency) we found only 10 (out of 110) unique edges among chronic patients were significantly modulated by damage. When using the EEG amplitude partial coherence (aGGM) on the other hand, we found only 9 (out of 171) unique edges among chronic patients were significantly modulated by damage. In summary, it's clear that the edge-by-edge analysis is unable to identify the influence of damage.

4.3.2 Mean Degrees and Damage

Following the edge by edge analysis, we examined data on a broader scale. We looked at the relationship between damage and connectivity at the whole connectome scale by examining the mean degrees. We estimated mean degrees for all frequency bands when using EEG-PC to determine the weights of the cGGM network and EEG-APC for the aGGM network and the mean degrees for the structural connectivity. Using these measures, we estimated a correlation between mean degrees of effective connectivity and mean degrees of SC. In the subacute group, we found a negative correlation existed in the delta ($r = -0.47, p < 0.05$) band in the partial coherence. When examining the relationship between mean degrees in the amplitude partial correlation and mean degrees of damage, we found no relationship in subacute group. We found that for chronic group when using the partial coherence there was a robust negative correlation between the mean degrees in theta ($r = -0.46, p < 0.005$), alpha ($r = -0.49, p < 0.005$) and lower beta ($r = -0.39, p < 0.05$) bands and the mean degrees of SC across patients. When examining the same relationship between mean degrees in the amplitude partial correlation and mean degrees of damage, we found weak but non-significant relationships in the chronic group. To ensure that the relationship between mean degrees and damage is truly a function of the network properties rather than the influence of

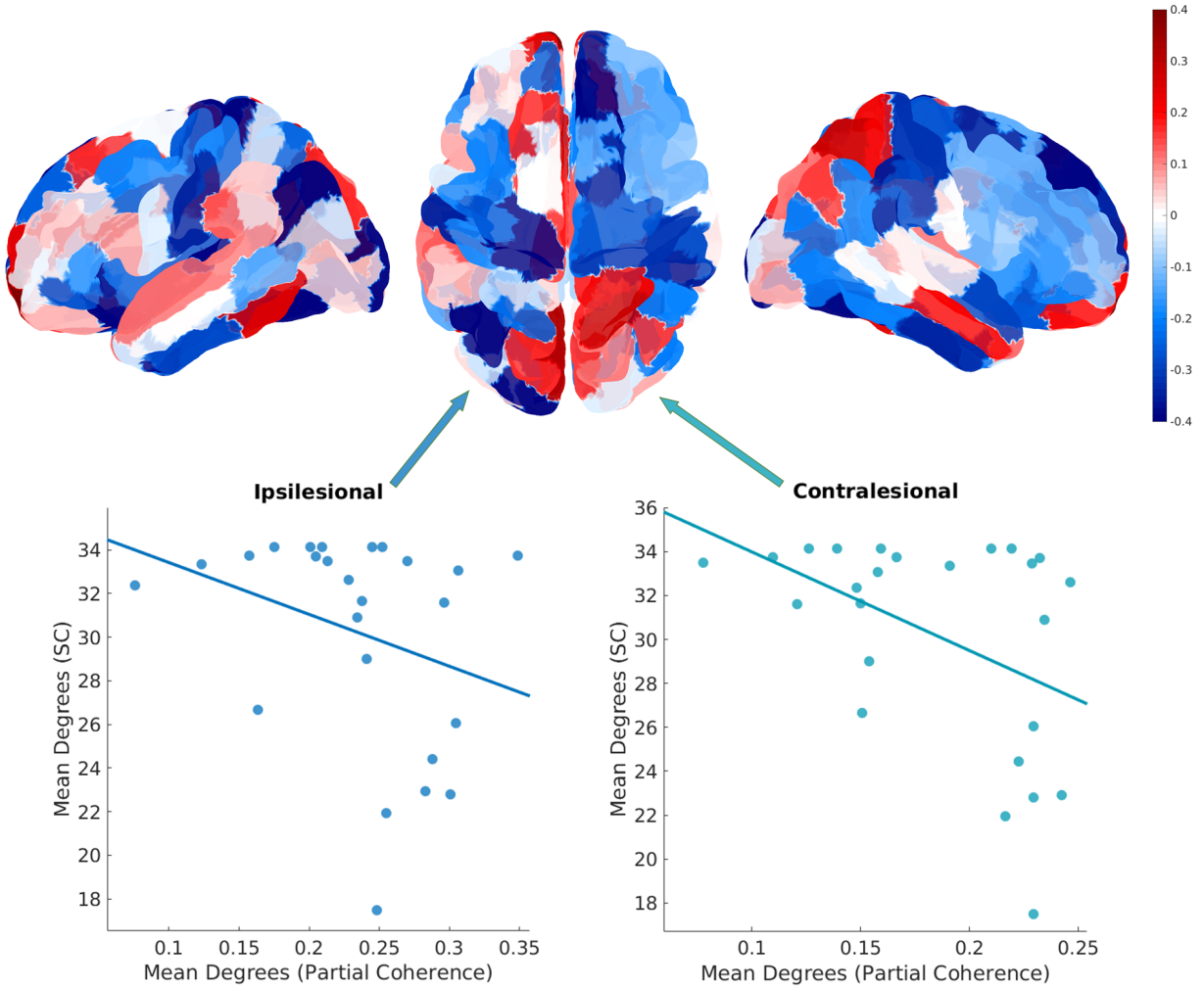

Figure 4.2: Mean Degrees in SC and Delta Band for Subacute group: In the top row we show the correlation between the degrees for each area and the mean degrees of damage across the subacute group of patients. In the bottom row we show a scatter of mean degrees over each hemisphere (ipsilesional/contralesional) and the mean degrees of damage in SC (across all areas).

the signal to noise ratio, we checked whether the correlation between the mean degrees of SC and EC was significant when partialling out the mean power in the band being examined. We found the relationship between SC and PC (in theta, alpha and lower beta for chronic and in delta for subacute) remained robust ($p < 0.01$) even when accounting for the power.

Additionally, we checked whether the contralesional or ipsilesional hemispheres were more influential in driving the negative correlation when using partial coherence. For the subacute group, we found that in the delta band. Correlations were more negative in the contralesional hemisphere relative to the ipsilesional hemisphere - $r = -0.45$ for contralesional hemisphere and $r = -0.31$ in the ipsilesional hemisphere (the difference was not significant). We show these results in detail in Figure 4.2. We found that for the chronic group in the theta band, the mean degrees of the ipsilesional hemisphere showed a significantly stronger ($p < 0.1$) negative correlation to mean SC degrees, i.e. the trend we see in the subacute group of patients is reversed. Correlations were -0.29 for contralesional hemisphere and -0.55 in the ipsilesional hemisphere. We saw a similar trend in the alpha and lower beta band - $r = -0.39$ and $r = -0.34$ for contralesional hemisphere and $r = -0.49$ and $r = -0.37$ in the ipsilesional hemisphere, however neither difference was significant.

Finally, in the theta band partial coherence for chronic patients we examined which areas particularly contributed to the relationship between mean degrees in partial coherence and the mean degrees of the structural connectome. We estimated the correlation between the degree of each area (in the theta band) and the mean degrees of the SC. We found a negative correlation over a majority of areas and this was particularly pronounced ($r < -0.4$) in the rostral middle frontal, pars orbitalis, postcentral and superior temporal areas of the ipsilesional hemisphere. In the contralesional hemisphere, paracentral, lingual and precuneus showed strong negative correlations ($r < -0.4$). Visually examining the correlations in Figure 4.3 we see that the negative correlation is heavily driven by areas in the ipsilesional parietal lobe.

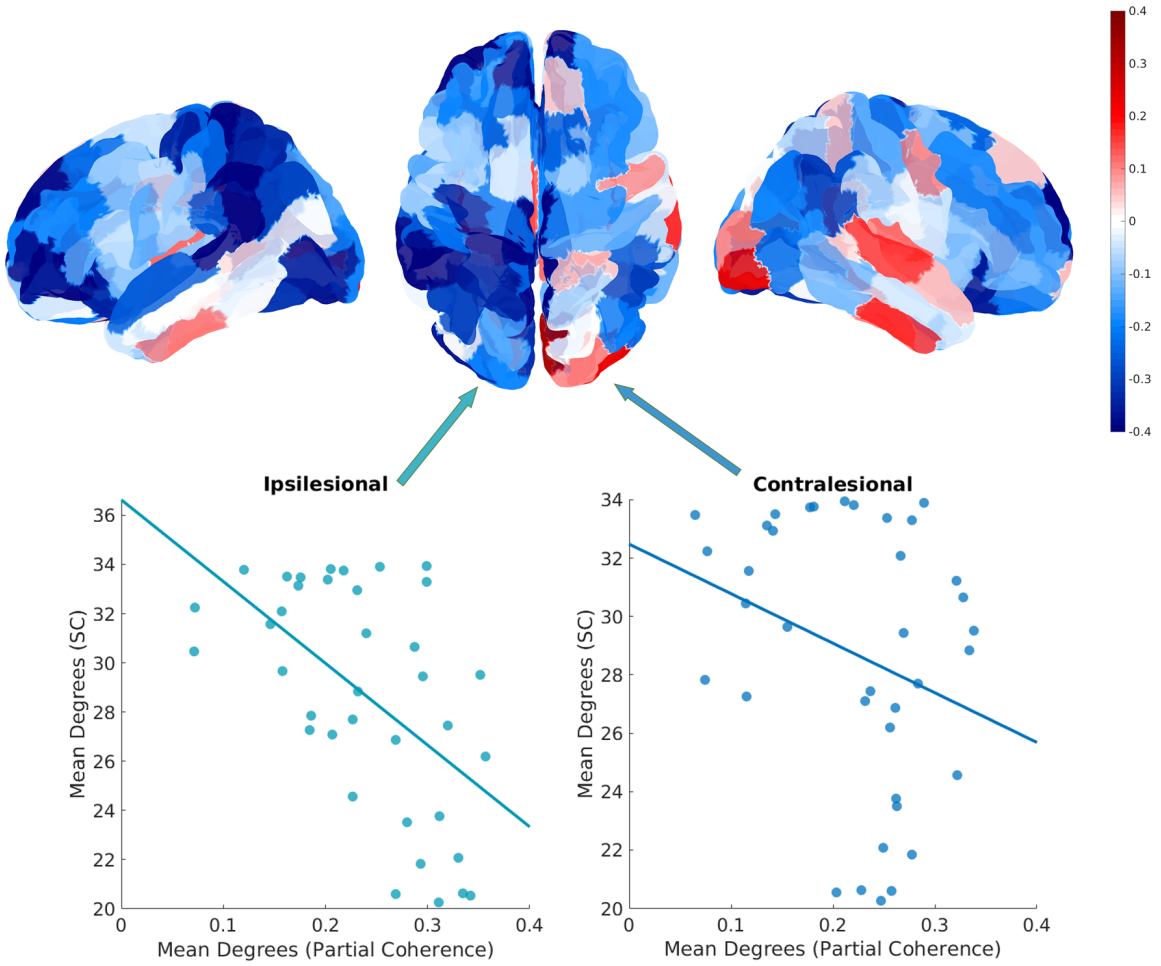

Figure 4.3: Mean Degrees in SC and Theta Band for Chronic group: In the top row we show the correlation between the degrees for each area and the mean degrees of damage across the chronic group of patients. In the bottom row we show a scatter of mean degrees over each hemisphere (ipsilesional/contralesional) and the mean degrees of damage in SC (across all areas).

4.4 Discussion

Using virtual tractography to define individual specific structural connectome (SC) damage, and EEG effective connectivity, we examined the influence of SC damage on effective connectivity in subacute and chronic stroke patients. In both patient groups, we showed that only a limited number of edges show the influence of damage on EEG-EC.

When examining the whole-brain level relationship between the connectome and EEG-EC, in the subacute group of patients we found mean degrees in delta band increased with increasing damage. This potentially compensatory mechanism was driven by the contralesional hemisphere. In the chronic group of patients, we found that partial coherence mean degrees increases with increasing damage in theta and alpha bands across chronic patients. There was again lateralization of the relationship to damage, with the ipsilesional hemisphere mean degrees being more tightly linked to the presence of damage.

Past work on discerning how the anatomical connectivity facilitates EEG connectivity [54, 55] has shown that there is a weak but significant relationship at an individual level functional and structural connectivity, explaining between 1 to 16% of the variance in EEG coherence. This relationship is stronger when using group averaged matrices for the functional connectivity [54], with structural connectivity explaining 23.4% of the variance in the EEG coherence. Further both of these studies looked at structural connectivity and coherence within individuals, rather than looking at the relationship between variability in structural connectivity and coherence across individuals. In our work, we used the case of patients of stroke where there is large heterogeneity in structural connectivity to examine this relationship. However, as might be expected from past studies where the structural connectivity to coherence relationship was weak, we did not find that damage influenced the EEG effective connectivity strongly. In Chapter 2 we found that when using MEG, the effective connectivity at frequencies above 8 Hz was tightly linked to SC for over 50% of the struc-

tural connectivity edges. A potential reason that, in EEG, estimating the SC to effective connectivity relationship is limited by the poorer knowledge of the forward model for EEG in comparison to MEG.

After the initial lesion from disruption in blood flow leading to stroke, there are broad changes in electrical activity in the brain [111, 115–117]. EEG activity as measured by spectral power in different frequency bands differs in characteristic ways during the acute, subacute and chronic stages of stroke [118–120]. In particular, in a rat model of stroke [121], during the subacute period, EEG showed higher delta power, while in the chronic stage there was higher theta and alpha power. These results have been replicated in longitudinal studies in human stroke patients [119, 120]. Further, connectivity in specific frequency bands during the acute (0-12 days) stage of stroke is important for predicting patient prognosis [122]. Characteristics of networks at the connectome level (estimated through graph theory) is altered in stroke patients [111, 112, 117]. In our connectome level analysis we found that mean degrees in the partial coherence increased with increasing damage in both subacute and chronic stage patients. While for chronic patients we saw this to be true in theta, alpha and lower beta bands, for subacute patients we only saw a negative correlation between mean degrees in EC and SC in the delta band. This higher sensitivity of the delta band in subacute patients fits with past work showing that during the early period after stroke delta power is specifically increased while other bands are not [119–121]. Further, our theta, alpha, lower beta results, is in line with past work that suggests that activity in these bands is altered in later stages of stroke. Our results add to this line of work by showing that, specifically in relation to increased white matter damage there is a compensatory increase in connectivity strengths. The increasing partial coherence with damage visible on the connectome scale suggests that there are compensatory mechanisms that are operating in both subacute and chronic patients.

We observed that the relationship of the overall connectivity in partial coherence and the SC

damage was lateralized, with the contralesional hemisphere driving the relationship for subacute stage patients while the ipsilesional hemisphere was relevant for chronic stage patients. In other words, the hemisphere where there is no damage seems to be more connected in subacute patients, while the hemisphere where there is damage is more connected in chronic patients. Past work on the changes in EEG and fMRI post stroke have shown that improvement in behavioral deficits is linked to the ipsilesional hemisphere showing greater activation over time, and regaining some of its functionality [114]. Our work demonstrates that this same trend is visible in the connectivity, with the chronic patients showing greater compensatory mechanisms in the ipsilesional hemisphere in the presence of greater damage. However, for the subacute patients, this renormalization is yet to occur and the contralesional hemisphere is undertaking the burden of damage.

On a technical note, our work shows the potential of using virtual tractography [105, 106] with effective connectivity estimates from EEG source imaging to identify the influence of SC damage on EEG EC. Virtual tractography's success is attributable to the low levels of across individual variability in structural connectivity[101]. In addition estimating EEG effective connectivity using the SC-QUIC method allows us to reduce the problems of leakage effects and common inputs. Using EEG-EC with virtual tractography is a framework that could be used in future studies to expand our understanding of the relationship between structure and function.

4.4.1 Limitations

Source localization in EEG is a heavily debated field, with many algorithms having been suggested to optimally reconstruct EEG activity in source space. The primary influence on source localization is the accuracy of the head model used. Studies have shown that neglecting the gray-white boundary and building a head model with a common boundary

for both leads to considerable error in the forward model [123]. Additionally, the conductivity for different tissues is only known approximately and assumed to be isotropic which may very well not be the case. These issues potentially lead to the weak results we see when examining the relationship between structural connections and effective connectivity.

When estimating effective connectivity, we assumed the simplest model possible, however, several papers have shown that more complex, phenomenologically accurate models of neural mass activity can be fitted with EEG data [124–127]. These models are potentially better at identifying the genuine effective connectivity between areas, but this is yet to be explored. Also, and more importantly, we ignore for our purposes subcortical source activity and connectivity. We do this partly because we expect that source localizing data at subcortical sources without explicit prior expectations is difficult given the measurement capabilities of EEG [92]. However, this may lead to large variation in the estimated results. An important note is that the influence of subcortical-cortical connectivity could bias graphical model based connectivity approaches as it acts as an unseen common influence. Similarly, unaccounted for neuromodulatory influences that only affect a small set of regions will also appear as unseen common influences on the connectivity structure and thus, bias the results.

In conclusion, while we found EEG effective connectivity to be a poor reflection of structural connectivity damage when examining individual edges, we saw that at a connectome scale there is a clear influence of white matter damage. This result indicates that the EEG EC is mediated by the structural connectome but unaccounted for influences (source localization, nonlinear connectivity, nonstationarity) make it difficult to identify the SC influence in a more resolved manner.

Chapter 5

Conclusion

Across three different neuroimaging modalities - fMRI, MEG and EEG - and using methods of estimating statistical dependencies between brain areas that emphasize different timescales of activity, we examined how structure constrains function in the brain. Using MEG (Chapter 2) we found that both slow and fast timescale effective connectivity estimates were sensitive to the structural connectome, but in different frequency bands. Also, using graph theory tools led to more accurate reconstructions of structural connectome characteristics. When using fMRI data in patients of subacute stroke (Chapter 3), with diverse damage to the white matter, we found that using an effective connectivity model showed the impact of damage across more edges than using functional connectivity (correlation). Averaging fMRI activity over the groups of voxels that demarcate a region of interest seems to unnecessarily spatially smooth diverse neural data. Instead, using streamlines to guide functional connectivity estimation at the voxel level showed the influence of structural connectivity damage across a larger set of connections. Finally, we found, using graph theory in EEG (Chapter 4) from subacute and chronic patients of stroke, that damage to the structural connectome influences EEG effective connectivity differently after damage is instantiated in the brain, possibly due to plasticity and potential compensatory effects.

5.1 Structural Connectivity and Graphical Models for Effective Connectivity

Simple models of functional connectivity - graphical models - were a core method we applied in examining how structure influenced function. Graphical models estimate conditional dependencies between areas thereby removing the influence of polysynaptic pathways and common input on the connection strength between brain areas. We built a framework (adaptive graphical lasso) that allowed us to bias graphical model estimation towards the structural connectome, and unlike past efforts [43], we did not directly use the SC weights, instead expecting connection strengths to vary between subjects and across frequency bands. Using this approach was clearly beneficial, as we saw when using MEG and fMRI data. Penalizations applied in the adaptive graphical lasso (as decided by cross validation) showed that there was high sensitivity in the data for the structural connectome, i.e, conditional dependencies between areas were mediated through the SC. In fMRI and EEG, use of graphical models allowed us to see modulation of connectivity from structural connectivity damage. Additionally, we saw when examining streamline functional connectivity that edges where damage induced modulation in FC were those that were traversed more rapidly under a diffusion process. This indicates that polysynaptic pathways are relevant for the generation of functional connectivity and potentially suggests that we should use graphical models at the voxel level. It is worth noting that while using graphical models appears to be well motivated by our analyses, there are caveats to appreciate. First, by not including subcortical areas, it is possible that common input effects appear as connections outside the connectome. Indeed we observed in Chapter 2, that in real MEG data, 30% of the edges recovered in cGGM and aGGM models were outside the original SC. Future efforts need to examine the level of impact this has on effective connectivity, and the ability to detect the presence of SC damage. Our work suggests that while we are able to detect the presence of damage reasonably well, we weren't able to see its influence in over 60% of connections in fMRI. One

of the reasons for this may be subcortical common drive effects. Second, gaussian graphical model estimation yields undirected connectivity. The expectation of undirected connectivity will estimate incorrect connectivity when there is directionality to connections between areas. For example, common input effects become more complex, with a connection motif such as $A \longrightarrow B \longleftarrow C$ leading to connectivity between A and C in both functional and effective undirected connectivity. The potential presence of such motifs and their relevance to functional connections will need to be explored in more detail in future work.

5.2 Structural Connectivity and Function across Different Timescales

Past work on showing the link between electrophysiological (M/EEG) networks and structural connectivity have been few but have shown significant relationships between structure and function[54–57]. No study to our knowledge, thus far, has examined the relationship of the SC to both estimates of connectivity based on amplitude and phase, and estimates of connectivity based on only amplitude, in humans. We found that in the MEG, gamma band (31 - 80 Hz) cGGM (using amplitude and phase) reflects the SC more closely than any other network estimate. This result indicates that the phase has information about the connectome, but primarily in higher frequencies ($>$ 30 Hz). The slower timescale amplitude envelope modulation (aGGM) reflects information about the SC primarily in lower frequencies (1-30 Hz), reaching a peak in the beta band. These results provide potentially useful constraints on theories of how the MEG connectivity is instantiated over the structural connectome. One possible theory is that phase information in lower frequencies occupies a range around 0 and is corrupted by leakage effects. However, at higher frequencies, we are able to recover phase consistency based networks with greater fidelity. At lower frequencies, amplitude alone provides a higher signal to noise ratio than amplitude and phase. However

at higher frequencies, using amplitude and phase together is better than using amplitude alone, which may be biased from genuine phase relationships [84].

5.3 Link between Structure and Function is Limited

Our work with MEG/ fMRI data to understand the influence of the structural connectome indicated an important item of note. We could see the influence of damage across only 40% of edges when using the fMRI streamline functional connectivity. The low number of edges being influenced by damage is likely related to some degree to the compensatory mechanisms occurring after stroke. Other potential influences could be subcortical and neuromodulatory in nature. When examining the sensitivity of MEG amplitude graphical models (known to have similar organization as fMRI resting state networks) to structural connectivity, we found that for the bands that best reflected the SC, sensitivity lay between 40 to 60% (40 to 60 % of SC edges were detected). Once more we see that 100% of SC edges do not influence the slow timescale connectivity structure. These results motivate explorations of whether the structural connectivity to functional connectivity relationship changes across different disease states and across different cognitive states[128–130]. This line of work may be particularly useful at identifying sources of influence on the functional connectivity other than the structural connectivity and exposing in greater detail the relationship of the structural connectome to functional connectivity.

5.4 Summary

In summary, our work showed how structure constrains function to a limited extent, influenced by the timescale and spatial resolution of effective connectivity estimates. Our results provide useful constraints on models of the link between structure and function in macroscale

resting state neural activity. Finally, our work motivates efforts to examine this relationship in more detail, incorporating information about other potential influences such as subcortical sources and neuromodulatory activity.

Bibliography

[1] Buzsaki G. Rhythms of the Brain. Oxford University Press; 2006.

[2] Fries P. Rhythms for cognition: communication through coherence. Neuron. 2015;88(1):220–235.

[3] Engel AK, Gerloff C, Hilgetag CC, Nolte G. Intrinsic coupling modes: multiscale interactions in ongoing brain activity. Neuron. 2013;80(4):867–886.

[4] Mill RD, Ito T, Cole MW. From connectome to cognition: The search for mechanism in human functional brain networks. NeuroImage. 2017;160:124–139.

[5] Medaglia JD, Lynall ME, Bassett DS. Cognitive network neuroscience. Journal of cognitive neuroscience. 2015;27(8):1471–1491.

[6] Sporns O, Tononi G, Kötter R. The human connectome: a structural description of the human brain. PLoS computational biology. 2005;1(4):e42.

[7] Taylor JR, Williams N, Cusack R, Auer T, Shafto MA, Dixon M, et al. The Cambridge Centre for Ageing and Neuroscience (Cam-CAN) data repository: structural and functional MRI, MEG, and cognitive data from a cross-sectional adult lifespan sample. Neuroimage. 2017;144:262–269.

[8] Van Essen DC, Smith SM, Barch DM, Behrens TE, Yacoub E, Ugurbil K, et al. The WU-Minn human connectome project: an overview. Neuroimage. 2013;80:62–79.

[9] Krishnan GP, González OC, Bazhenov M. Origin of slow spontaneous resting-state neuronal fluctuations in brain networks. Proceedings of the National Academy of Sciences. 2018;115(26):6858–6863.

[10] Marder E. Neuromodulation of neuronal circuits: back to the future. Neuron. 2012;76(1):1–11.

[11] Bargmann CI, Marder E. From the connectome to brain function. Nature methods. 2013;10(6):483.

[12] Nunez PL, Srinivasan R. Electric fields of the brain: the neurophysics of EEG. Oxford University Press, USA; 2006.

[13] Baillet S. Magnetoencephalography for brain electrophysiology and imaging. Nature neuroscience. 2017;20(3):327.

[14] Logothetis NK. What we can do and what we cannot do with fMRI. Nature. 2008;453(7197):869.

[15] Friston KJ. Functional and effective connectivity: a review. Brain connectivity. 2011;1(1):13–36.

[16] Eickhoff SB, Yeo BT, Genon S. Imaging-based parcellations of the human brain. Nature Reviews Neuroscience. 2018;p. 1.

[17] Greicius MD, Krasnow B, Reiss AL, Menon V. Functional connectivity in the resting brain: a network analysis of the default mode hypothesis. Proceedings of the National Academy of Sciences. 2003;100(1):253–258.

[18] Raichle ME. The brain's default mode network. Annual review of neuroscience. 2015;38:433–447.

[19] Hipp JF, Hawellek DJ, Corbetta M, Siegel M, Engel AK. Large-scale cortical correlation structure of spontaneous oscillatory activity. Nature neuroscience. 2012;15(6):884.

[20] Mantini D, Perrucci MG, Del Gratta C, Romani GL, Corbetta M. Electrophysiological signatures of resting state networks in the human brain. Proceedings of the National Academy of Sciences. 2007;104(32):13170–13175.

[21] Bendat JS, Piersol AG. Random data: analysis and measurement procedures. vol. 729. John Wiley & Sons; 2011.

[22] OfNeill GC, Barratt EL, Hunt BA, Tewarie PK, Brookes MJ. Measuring electrophysiological connectivity by power envelope correlation: a technical review on MEG methods. Physics in Medicine & Biology. 2015;60(21):R271.

[23] Brookes MJ, Woolrich M, Luckhoo H, Price D, Hale JR, Stephenson MC, et al. Investigating the electrophysiological basis of resting state networks using magnetoencephalography. Proceedings of the National Academy of Sciences. 2011;108(40):16783–16788.

[24] Brookes MJ, Hale JR, Zumer JM, Stevenson CM, Francis ST, Barnes GR, et al. Measuring functional connectivity using MEG: methodology and comparison with fcMRI. Neuroimage. 2011;56(3):1082–1104.

[25] Hipp JF, Siegel M. BOLD fMRI correlation reflects frequency-specific neuronal correlation. Current Biology. 2015;25(10):1368–1374.

[26] Srinivasan R, Nunez PL, Silberstein RB. Spatial filtering and neocortical dynamics: estimates of EEG coherence. IEEE Transactions on Biomedical Engineering. 1998;45(7):814–826.

[27] Srinivasan R, Winter WR, Ding J, Nunez PL. EEG and MEG coherence: measures of functional connectivity at distinct spatial scales of neocortical dynamics. Journal of neuroscience methods. 2007;166(1):41–52.

[28] Hauk O. Keep it simple: a case for using classical minimum norm estimation in the analysis of EEG and MEG data. Neuroimage. 2004;21(4):1612–1621.

[29] Dale A. Sereno Mi Improved localization of cortical activity by combining EEG and MEG with MRI cortical surface reconstruction: A linear approach. J Cogn Neurosci. 1993;5:162–170.

[30] Schoffelen JM, Gross J. Source connectivity analysis with MEG and EEG. Human brain mapping. 2009;30(6):1857–1865.

[31] Whittaker J. Graphical models in applied multivariate statistics. Wiley Publishing; 2009.

[32] Friedman J, Hastie T, Tibshirani R. Sparse inverse covariance estimation with the graphical lasso. Biostatistics. 2008;9(3):432–441.

[33] Meinshausen N, Bühlmann P, et al. High-dimensional graphs and variable selection with the lasso. The annals of statistics. 2006;34(3):1436–1462.

[34] Marrelec G, Krainik A, Duffau H, Pélégrini-Issac M, Lehéricy S, Doyon J, et al. Partial correlation for functional brain interactivity investigation in functional MRI. Neuroimage. 2006;32(1):228–237.

[35] Smith SM, Vidaurre D, Beckmann CF, Glasser MF, Jenkinson M, Miller KL, et al. Functional connectomics from resting-state fMRI. Trends in cognitive sciences. 2013;17(12):666–682.

[36] Smith SM, Miller KL, Salimi-Khorshidi G, Webster M, Beckmann CF, Nichols TE, et al. Network modelling methods for FMRI. Neuroimage. 2011;54(2):875–891.

[37] Ryali S, Chen T, Supekar K, Menon V. Estimation of functional connectivity in fMRI data using stability selection-based sparse partial correlation with elastic net penalty. NeuroImage. 2012;59(4):3852–3861.

[38] Fransson P, Marrelec G. The precuneus/posterior cingulate cortex plays a pivotal role in the default mode network: Evidence from a partial correlation network analysis. Neuroimage. 2008;42(3):1178–1184.

[39] He H, Sui J, Yu Q, Turner JA, Ho BC, Sponheim SR, et al. Altered small-world brain networks in schizophrenia patients during working memory performance. PloS one. 2012;7(6):e38195.

[40] de Vos F, Koini M, Schouten TM, Seiler S, van der Grond J, Lechner A, et al. A comprehensive analysis of resting state fMRI measures to classify individual patients with Alzheimer's disease. Neuroimage. 2018;167:62–72.

[41] Horn A, Ostwald D, Reisert M, Blankenburg F. The structural–functional connectome and the default mode network of the human brain. Neuroimage. 2014;102:142–151.

[42] Huebner NS, Mechling AE, Lee HL, Reisert M, Bienert T, Hennig J, et al. The connectomics of brain demyelination: functional and structural patterns in the cuprizone mouse model. Neuroimage. 2017;146:1–18.

[43] Pineda-Pardo JA, Bruña R, Woolrich M, Marcos A, Nobre AC, Maestú F, et al. Guiding functional connectivity estimation by structural connectivity in MEG: an application to discrimination of conditions of mild cognitive impairment. Neuroimage. 2014;101:765–777.

[44] Paz-Linares D, Gonzalez-Moreira E, Martinez-Montes E, Valdes-Sosa PA. Note on the Estimation of Embedded Hermitian Gaussian Graphical Models for MEEG Source Activity and Connectivity Analysis in the Frequency Domain. Part I: Single Frequency Component and Subject. arXiv preprint arXiv:181001174. 2018;.

[45] Gao X, Shen W, Ting CM, Cramer SC, Srinivasan R, Ombao H. Modeling Brain Connectivity with Graphical Models on Frequency Domain. arXiv preprint arXiv:181003279. 2018;.

[46] Wodeyar A, Srinivasan R. Network Structure During Encoding Predicts Working Memory Performance. bioRxiv. 2018;p. 409615.

[47] Fornito A, Zalesky A, Bullmore E. Fundamentals of brain network analysis. Academic Press; 2016.

[48] Honey CJ, Kötter R, Breakspear M, Sporns O. Network structure of cerebral cortex shapes functional connectivity on multiple time scales. Proceedings of the National Academy of Sciences. 2007;104(24):10240–10245.

[49] Goñi J, van den Heuvel MP, Avena-Koenigsberger A, de Mendizabal NV, Betzel RF, Griffa A, et al. Resting-brain functional connectivity predicted by analytic measures of network communication. Proceedings of the National Academy of Sciences. 2014;111(2):833–838.

[50] OfReilly JX, Croxson PL, Jbabdi S, Sallet J, Noonan MP, Mars RB, et al. Causal effect of disconnection lesions on interhemispheric functional connectivity in rhesus monkeys. Proceedings of the National Academy of Sciences. 2013;110(34):13982–13987.

[51] Messé A, Rudrauf D, Giron A, Marrelec G. Predicting functional connectivity from structural connectivity via computational models using MRI: an extensive comparison study. NeuroImage. 2015;111:65–75.

[52] Grayson DS, Bliss-Moreau E, Machado CJ, Bennett J, Shen K, Grant KA, et al. The rhesus monkey connectome predicts disrupted functional networks resulting from pharmacogenetic inactivation of the amygdala. Neuron. 2016;91(2):453–466.

[53] Straathof M, Sinke MR, Dijkhuizen RM, Otte WM. A systematic review on the quantitative relationship between structural and functional network connectivity strength in mammalian brains. Journal of Cerebral Blood Flow & Metabolism. 2018;p. 0271678X18809547.

[54] Finger H, Bönstrup M, Cheng B, Messé A, Hilgetag C, Thomalla G, et al. Modeling of large-scale functional brain networks based on structural connectivity from DTI: comparison with EEG derived phase coupling networks and evaluation of alternative methods along the modeling path. PLoS computational biology. 2016;12(8):e1005025.

[55] Chu CJ, Tanaka N, Diaz J, Edlow BL, Wu O, Hämäläinen M, et al. EEG functional connectivity is partially predicted by underlying white matter connectivity. Neuroimage. 2015;108:23–33.

[56] Tewarie P, Hillebrand A, van Dellen E, Schoonheim MM, Barkhof F, Polman C, et al. Structural degree predicts functional network connectivity: a multimodal resting-state fMRI and MEG study. Neuroimage. 2014;97:296–307.

[57] Garcés P, Pereda E, Hernández-Tamames JA, Del-Pozo F, Maestú F, Ángel Pineda-Pardo J. Multimodal description of whole brain connectivity: A comparison of resting state MEG, fMRI, and DWI. Human brain mapping. 2016;37(1):20–34.

[58] Mišić B, Betzel RF, Nematzadeh A, Goñi J, Griffa A, Hagmann P, et al. Cooperative and competitive spreading dynamics on the human connectome. Neuron. 2015;86(6):1518–1529.

[59] Roux F, Uhlhaas PJ. Working memory and neural oscillations: alpha–gamma versus theta–gamma codes for distinct WM information? Trends in cognitive sciences. 2014;18(1):16–25.

[60] Stam CJ. Modern network science of neurological disorders. Nature Reviews Neuroscience. 2014;15(10):683.

[61] Rouhinen S, Panula J, Palva JM, Palva S. Load dependence of β and γ oscillations predicts individual capacity of visual attention. Journal of Neuroscience. 2013;33(48):19023–19033.

[62] Siebenhühner F, Wang SH, Palva JM, Palva S. Cross-frequency synchronization connects networks of fast and slow oscillations during visual working memory maintenance. Elife. 2016;5:e13451.

[63] De Pasquale F, Della Penna S, Snyder AZ, Lewis C, Mantini D, Marzetti L, et al. Temporal dynamics of spontaneous MEG activity in brain networks. Proceedings of the National Academy of Sciences. 2010;107(13):6040–6045.

[64] Colclough GL, Woolrich MW, Tewarie P, Brookes MJ, Quinn AJ, Smith SM. How reliable are MEG resting-state connectivity metrics? Neuroimage. 2016;138:284–293.

[65] Bullmore E, Sporns O. The economy of brain network organization. Nature Reviews Neuroscience. 2012;13(5):336.

[66] Cammoun L, Gigandet X, Meskaldji D, Thiran JP, Sporns O, Do KQ, et al. Mapping the human connectome at multiple scales with diffusion spectrum MRI. Journal of neuroscience methods. 2012;203(2):386–397.

[67] Cabral J, Luckhoo H, Woolrich M, Joensson M, Mohseni H, Baker A, et al. Exploring mechanisms of spontaneous functional connectivity in MEG: how delayed network interactions lead to structured amplitude envelopes of band-pass filtered oscillations. Neuroimage. 2014;90:423–435.

[68] Yeh FC, Panesar S, Fernandes D, Meola A, Yoshino M, Fernandez-Miranda JC, et al. Population-averaged atlas of the macroscale human structural connectome and its network topology. NeuroImage. 2018;178:57–68.

[69] Colby JB, Soderberg L, Lebel C, Dinov ID, Thompson PM, Sowell ER. Along-tract statistics allow for enhanced tractography analysis. Neuroimage. 2012;59(4):3227–3242.

[70] Hagmann P, Cammoun L, Gigandet X, Meuli R, Honey CJ, Wedeen VJ, et al. Mapping the structural core of human cerebral cortex. PLoS biology. 2008;6(7):e159.

[71] Schreier PJ, Scharf LL. Statistical signal processing of complex-valued data: the theory of improper and noncircular signals. Cambridge University Press; 2010.

[72] Malmivuo P, Malmivuo J, Plonsey R. Bioelectromagnetism: principles and applications of bioelectric and biomagnetic fields. Oxford University Press, USA; 1995.

[73] Fischl B. FreeSurfer. Neuroimage. 2012;62(2):774–781.

[74] Gramfort A, Papadopoulo T, Olivi E, Clerc M. OpenMEEG: opensource software for quasistatic bioelectromagnetics. Biomedical engineering online. 2010;9(1):45.

[75] Menéndez P, Kourmpetis YA, ter Braak CJ, van Eeuwijk FA. Gene regulatory networks from multifactorial perturbations using Graphical Lasso: application to the DREAM4 challenge. PloS one. 2010;5(12):e14147.

[76] Varoquaux G, Gramfort A, Poline JB, Thirion B. Brain covariance selection: better individual functional connectivity models using population prior. In: Advances in neural information processing systems; 2010. p. 2334–2342.

[77] Zerenner T, Friederichs P, Lehnertz K, Hense A. A Gaussian graphical model approach to climate networks. Chaos: An Interdisciplinary Journal of Nonlinear Science. 2014;24(2):023103.

[78] Hsieh CJ, Dhillon IS, Ravikumar PK, Sustik MA. Sparse inverse covariance matrix estimation using quadratic approximation. In: Advances in neural information processing systems; 2011. p. 2330–2338.

[79] Zou H. The adaptive lasso and its oracle properties. Journal of the American statistical association. 2006;101(476):1418–1429.

[80] Murphy K, Dunham M. PMTK: Probabilistic modeling toolkit. In: Neural Information Processing Systems (NIPS) Workshop on Probabilistic Programming; 2008. .

[81] Dahlhaus R. Graphical interaction models for multivariate time series. Metrika. 2000;51(2):157–172.

[82] Rubinov M, Sporns O. Complex network measures of brain connectivity: uses and interpretations. Neuroimage. 2010;52(3):1059–1069.

[83] Chu CJ, Kramer MA, Pathmanathan J, Bianchi MT, Westover MB, Wizon L, et al. Emergence of stable functional networks in long-term human electroencephalography. Journal of Neuroscience. 2012;32(8):2703–2713.

[84] Palva JM, Wang SH, Palva S, Zhigalov A, Monto S, Brookes MJ, et al. Ghost interactions in MEG/EEG source space: A note of caution on inter-areal coupling measures. Neuroimage. 2018;173:632–643.

[85] Nelli S, Itthipuripat S, Srinivasan R, Serences JT. Fluctuations in instantaneous frequency predict alpha amplitude during visual perception. Nature communications. 2017;8(1):2071.

[86] Lai M, Demuru M, Hillebrand A, Fraschini M. A comparison between scalp-and source-reconstructed EEG networks. Scientific reports. 2018;8(1):12269.

[87] Antiqueira L, Rodrigues FA, van Wijk BC, Costa LdF, Daffertshofer A. Estimating complex cortical networks via surface recordings?a critical note. Neuroimage. 2010;53(2):439–449.

[88] Zalesky A, Fornito A, Bullmore E. On the use of correlation as a measure of network connectivity. Neuroimage. 2012;60(4):2096–2106.

[89] Nolte G, Bai O, Wheaton L, Mari Z, Vorbach S, Hallett M. Identifying true brain interaction from EEG data using the imaginary part of coherency. Clinical neurophysiology. 2004;115(10):2292–2307.

[90] Siems M, Siegel M. Dissociated cortical phase-and amplitude-coupling patterns in the human brain. bioRxiv. 2018;p. 485599.

[91] Wipf D, Nagarajan S. A unified Bayesian framework for MEG/EEG source imaging. NeuroImage. 2009;44(3):947–966.

[92] Krishnaswamy P, Obregon-Henao G, Ahveninen J, Khan S, Babadi B, Iglesias JE, et al. Sparsity enables estimation of both subcortical and cortical activity from MEG and EEG. Proceedings of the National Academy of Sciences. 2017;114(48):E10465–E10474.

[93] Xiong J, Parsons LM, Gao JH, Fox PT. Interregional connectivity to primary motor cortex revealed using MRI resting state images. Human brain mapping. 1999;8(2-3):151–156.

[94] Raichle ME, MacLeod AM, Snyder AZ, Powers WJ, Gusnard DA, Shulman GL. A default mode of brain function. Proceedings of the National Academy of Sciences. 2001;98(2):676–682.

[95] Fox MD, Snyder AZ, Vincent JL, Corbetta M, Van Essen DC, Raichle ME. The human brain is intrinsically organized into dynamic, anticorrelated functional networks. Proceedings of the National Academy of Sciences. 2005;102(27):9673–9678.

[96] Koch MA, Norris DG, Hund-Georgiadis M. An investigation of functional and anatomical connectivity using magnetic resonance imaging. Neuroimage. 2002;16(1):241–250.

[97] Van Den Heuvel MP, Mandl RC, Kahn RS, Hulshoff Pol HE. Functionally linked resting-state networks reflect the underlying structural connectivity architecture of the human brain. Human brain mapping. 2009;30(10):3127–3141.

[98] Maier-Hein KH, Neher PF, Houde JC, Côté MA, Garyfallidis E, Zhong J, et al. The challenge of mapping the human connectome based on diffusion tractography. Nature communications. 2017;8(1):1349.

[99] de Reus MA, Van den Heuvel MP. The parcellation-based connectome: limitations and extensions. Neuroimage. 2013;80:397–404.

[100] Stulz SB, Insabato A, Deco G, Gilson M, Senden M. Comparing Task-Relevant Information Across Different Methods of Extracting Functional Connectivity. bioRxiv. 2018;p. 509059.

[101] Chamberland M, Girard G, Bernier M, Fortin D, Descoteaux M, Whittingstall K. On the origin of individual functional connectivity variability: The role of white matter architecture. Brain connectivity. 2017;7(8):491–503.

[102] Zimmermann J, Griffiths J, Schirner M, Ritter P, McIntosh AR. Subject specificity of the correlation between large-scale structural and functional connectivity. Network Neuroscience. 2018;3(1):90–106.

[103] Abdelnour F, Voss HU, Raj A. Network diffusion accurately models the relationship between structural and functional brain connectivity networks. Neuroimage. 2014;90:335–347.

[104] Avena-Koenigsberger A, Misic B, Sporns O. Communication dynamics in complex brain networks. Nature Reviews Neuroscience. 2018;19(1):17.

[105] Kuceyeski A, Maruta J, Relkin N, Raj A. The Network Modification (NeMo) Tool: elucidating the effect of white matter integrity changes on cortical and subcortical structural connectivity. Brain connectivity. 2013;3(5):451–463.

[106] Pustina D, Coslett HB, Ungar L, Faseyitan OK, Medaglia JD, Avants B, et al. Enhanced estimations of post-stroke aphasia severity using stacked multimodal predictions. Human brain mapping. 2017;38(11):5603–5615.

[107] Whitfield-Gabrieli S, Nieto-Castanon A. Conn: a functional connectivity toolbox for correlated and anticorrelated brain networks. Brain connectivity. 2012;2(3):125–141.

[108] Park B, Eo J, Park HJ. Structural Brain Connectivity Constrains within-a-Day Variability of Direct Functional Connectivity. Frontiers in human neuroscience. 2017;11:408.

[109] Skudlarski P, Jagannathan K, Calhoun VD, Hampson M, Skudlarska BA, Pearlson G. Measuring brain connectivity: diffusion tensor imaging validates resting state temporal correlations. Neuroimage. 2008;43(3):554–561.

[110] Karnath HO, Sperber C, Rorden C. Mapping human brain lesions and their functional consequences. Neuroimage. 2018;165:180–189.

[111] Fallani FDV, Pichiorri F, Morone G, Molinari M, Babiloni F, Cincotti F, et al. Multiscale topological properties of functional brain networks during motor imagery after stroke. Neuroimage. 2013;83:438–449.

[112] Caliandro P, Vecchio F, Miraglia F, Reale G, Della Marca G, La Torre G, et al. Small-world characteristics of cortical connectivity changes in acute stroke. Neurorehabilitation and neural repair. 2017;31(1):81–94.

[113] Philips GR, Daly JJ, Príncipe JC. Topographical measures of functional connectivity as biomarkers for post-stroke motor recovery. Journal of neuroengineering and rehabilitation. 2017;14(1):67.

[114] Rehme AK, Eickhoff SB, Wang LE, Fink GR, Grefkes C. Dynamic causal modeling of cortical activity from the acute to the chronic stage after stroke. Neuroimage. 2011;55(3):1147–1158.

[115] Westlake KP, Hinkley LB, Bucci M, Guggisberg AG, Findlay AM, Henry RG, et al. Resting state alpha-band functional connectivity and recovery after stroke. Experimental neurology. 2012;237(1):160–169.

[116] Gottselig J, Bassetti C, Achermann P. Power and coherence of sleep spindle frequency activity following hemispheric stroke. Brain. 2002;125(2):373–383.

[117] Fallani FDV, Clausi S, Leggio M, Chavez M, Valencia M, Maglione AG, et al. Interhemispheric connectivity characterizes cortical reorganization in motor-related networks after cerebellar lesions. The Cerebellum. 2017;16(2):358–375.

[118] Kam JW, Solbakk AK, Endestad T, Meling TR, Knight RT. Lateral prefrontal cortex lesion impairs regulation of internally and externally directed attention. NeuroImage. 2018;175:91–99.

[119] Zappasodi F, Tecchio F, Marzetti L, Pizzella V, Di Lazzaro V, Assenza G, et al. Longitudinal quantitative electroencephalographic study in mono-hemispheric stroke patients. Neural regeneration research. 2019;14(7):1237.

[120] Giaquinto S, Cobianchi A, Macera F, Nolfe G. EEG recordings in the course of recovery from stroke. Stroke. 1994;25(11):2204–2209.

[121] Zhang Sj, Ke Z, Li L, Yip Sp, Tong Ky. EEG patterns from acute to chronic stroke phases in focal cerebral ischemic rats: correlations with functional recovery. Physiological measurement. 2013;34(4):423.

[122] Wu J, Quinlan EB, Dodakian L, McKenzie A, Kathuria N, Zhou RJ, et al. Connectivity measures are robust biomarkers of cortical function and plasticity after stroke. Brain. 2015;138(8):2359–2369.

[123] Cho JH, Vorwerk J, Wolters CH, Knösche TR. Influence of the head model on EEG and MEG source connectivity analyses. Neuroimage. 2015;110:60–77.

[124] Saggar M, Zanesco AP, King BG, Bridwell DA, MacLean KA, Aichele SR, et al. Mean-field thalamocortical modeling of longitudinal EEG acquired during intensive meditation training. NeuroImage. 2015;114:88–104.

[125] Kiebel SJ, David O, Friston KJ. Dynamic causal modelling of evoked responses in EEG/MEG with lead field parameterization. NeuroImage. 2006;30(4):1273–1284.

[126] David O, Kiebel SJ, Harrison LM, Mattout J, Kilner JM, Friston KJ. Dynamic causal modeling of evoked responses in EEG and MEG. NeuroImage. 2006;30(4):1255–1272.

[127] Larsen LH, Zibrandtsen IC, Wienecke T, Kjaer TW, Langberg H, Nielsen JB, et al. Modulation of task-related cortical connectivity in the acute and subacute phase after stroke. European Journal of Neuroscience. 2018;47(8):1024–1032.

[128] Zimmermann J, Griffiths JD, McIntosh AR. Unique mapping of structural and functional connectivity on cognition. Journal of Neuroscience. 2018;38(45):9658–9667.

[129] Zhang J, Zhang Y, Wang L, Sang L, Yang J, Yan R, et al. Disrupted structural and functional connectivity networks in ischemic stroke patients. Neuroscience. 2017;364:212–225.

[130] Shah P, Ashourvan A, Mikhail F, Pines A, Kini L, Oechsel K, et al. Characterizing the role of the structural connectome in seizure dynamics. Brain. 2019;.

Appendix A

Locations of Areas

A.1 MNI coordinates of Lausanne Parcellation

Areas	X	Y	Z
R-lateralorbitofrontal_1	26.97	42.28	-35.02
R-lateralorbitofrontal_2	23.78	63.03	-33.88
R-parsorbitalis_1	45.48	59.01	-29.34
R-frontalpole_1	10.13	84.69	-28.81
R-medialorbitofrontal_1	7.07	71.81	-28.42
R-medialorbitofrontal_2	6.78	46.77	-37.22
R-parstriangularis_1	50.07	51	-13.32
R-parsopercularis_1	49.98	34.56	-4.01
R-rostralmiddlefrontal_1	38.85	57.15	10.37
R-rostralmiddlefrontal_2	30.71	76.7	-15.22
R-superiorfrontal_1	10.58	75.15	-1.21
R-superiorfrontal_2	14.21	58.85	24.29
R-superiorfrontal_3	11.02	32.88	36.71

Areas	X	Y	Z
R-superiorfrontal_4	22.63	25.48	42.16
R-caudalmiddlefrontal_1	38.39	29.7	29.68
R-precentral_1	54.72	23.92	-1.53
R-precentral_2	50.67	15.57	24.56
R-precentral_3	27.28	2	45.74
R-paracentral_1	9.31	-6.28	37.95
R-rostralanteriorcingulate_1	7.84	56.45	-14.87
R-caudalanteriorcingulate_1	7.27	42.04	8.19
R-posteriorcingulate_1	7.54	4.39	19.98
R-isthmuscingulate_1	9.71	-26.34	1.43
R-postcentral_1	57.67	10.33	-0.26
R-postcentral_2	42.02	-5.4	37.26
R-supramarginal_1	58.26	-15.51	23.26
R-supramarginal_2	56.58	-5.84	9.73
R-superiorparietal_1	30.18	-23.56	40.04
R-superiorparietal_2	26.51	-40.13	42.99
R-superiorparietal_3	24.63	-59.21	20.82
R-inferiorparietal_1	50.95	-30.78	22.56
R-inferiorparietal_2	42.98	-46.78	23.12
R-inferiorparietal_3	50.28	-45.64	5.32
R-precuneus_1	14.59	-42.18	7.51
R-precuneus_2	9.24	-34.67	31.75
R-cuneus_1	9.85	-59.25	5.28
R-pericalcarine_1	13.21	-59.32	-10.25
R-lateraloccipital_1	28.32	-73.83	-5.41
R-lateraloccipital_2	37.09	-66.83	-24.79

Areas	X	Y	Z
R-lateraloccipital_3	48.76	-49.32	-13.38
R-lingual_1	11.81	-55.19	-22.38
R-lingual_2	20.9	-36.4	-20.23
R-fusiform_1	40.19	-41.26	-31.93
R-fusiform_2	36.06	-3.6	-47.53
R-parahippocampal_1	26.76	-11.24	-35.67
R-entorhinal_1	26.5	14.78	-51.04
R-temporalpole_1	31.32	33.8	-52.97
R-inferiortemporal_1	50.35	8.32	-51.78
R-inferiortemporal_2	57.45	-30.29	-30.29
R-middletemporal_1	62.67	-22.56	-18.07
R-middletemporal_2	57.86	13.58	-41.33
R-bankssts_1	55.87	-20.54	-8.03
R-superiortemporal_1	60.13	-0.45	-13.5
R-superiortemporal_2	49.16	26.79	-33.95
R-transversetemporal_1	46.46	-0.6	-8.94
R-insula_1	39.32	10.13	-10.77
R-insula_2	37.47	30.36	-24.25
L-lateralorbitofrontal_1	-26.17	40.79	-34.04
L-lateralorbitofrontal_2	-17.86	62.99	-34.75
L-parsorbitalis_1	-41.71	56.61	-30.39
L-frontalpole_1	-5.77	85.45	-25.71
L-medialorbitofrontal_1	-4.04	58.13	-33.47
L-parstriangularis_1	-44.94	51.42	-15.19
L-parsopercularis_1	-45.78	35.54	-3.14
L-rostralmiddlefrontal_1	-32.7	51.98	14.48

Areas	X	Y	Z
L-rostralmiddlefrontal_2	-30.86	68.07	1.5
L-rostralmiddlefrontal_3	-26.99	76.58	-19.85
L-superiorfrontal_1	-7.11	74.07	-3.76
L-superiorfrontal_2	-5.91	62.3	17.89
L-superiorfrontal_3	-14.02	44.37	32.89
L-superiorfrontal_4	-8.2	25.33	40.62
L-caudalmiddlefrontal_1	-33.57	30.13	28.77
L-precentral_1	-16.86	0.58	48.21
L-precentral_2	-34.61	2.8	41.26
L-precentral_3	-45.2	13	23.67
L-precentral_4	-50.68	21.66	1.57
L-paracentral_1	-4.99	-8.44	38.66
L-rostralanteriorcingulate_1	-3.93	55.55	-18.13
L-caudalanteriorcingulate_1	-3.77	40.06	8.16
L-posteriorcingulate_1	-3.93	0.84	19.69
L-isthmuscingulate_1	-5.38	-27.4	1.68
L-postcentral_1	-19.93	-16.06	49.99
L-postcentral_2	-41.23	-9.55	36.43
L-postcentral_3	-54.34	5.16	7.28
L-supramarginal_1	-52.77	-8.2	7.14
L-supramarginal_2	-52.39	-23.28	20.95
L-superiorparietal_1	-22.81	-30.44	43.02
L-superiorparietal_2	-24.03	-40.14	34.29
L-superiorparietal_3	-15.42	-60.88	21.38
L-inferiorparietal_1	-40.16	-56.58	9.05
L-inferiorparietal_2	-39.37	-44.71	23.99

Areas	X	Y	Z
L-precuneus_1	-5.79	-31.47	33.21
L-precuneus_2	-7.33	-45.79	12.62
L-cuneus_1	-4.32	-60.35	3.62
L-pericalcarine_1	-7.89	-62.18	-12.14
L-lateraloccipital_1	-14.69	-78.59	-11.92
L-lateraloccipital_2	-38.62	-62.7	-14.32
L-lingual_1	-8.94	-55.72	-24.34
L-lingual_2	-16.29	-39.21	-19.68
L-fusiform_1	-36.54	-44.32	-33
L-fusiform_2	-31.18	-5.46	-46.05
L-parahippocampal_1	-23.44	-11.87	-36.46
L-entorhinal_1	-23.72	12.63	-51.1
L-temporalpole_1	-27.73	31.81	-53.41
L-inferiortemporal_1	-49.26	2.2	-49.31
L-inferiortemporal_2	-50.32	-34.64	-29.43
L-middletemporal_1	-59.05	-29.05	-16.77
L-middletemporal_2	-54.41	10.17	-39.03
L-bankssts_1	-51.46	-26.3	-9.84
L-superiortemporal_1	-55.15	-17.25	-3.97
L-superiortemporal_2	-49.22	16.88	-28.11
L-transversetemporal_1	-41.83	-4.28	-9.04
L-insula_1	-35.62	7.3	-12.91
L-insula_2	-32.68	30.21	-21.23

Table A.1: Lausanne Parcellation of 114 areas: For each area we define the center of the area in X,Y, and Z coordinates defined for the MNI template.